

LICENTIATE THESIS

Prospects for performing tests of quantum  
electrodynamics with high-intensity lasers

CHRISTOFFER OLOFSSON

---

Department of Physics  
University of Gothenburg  
Gothenburg, Sweden 2023

*Prospects for performing tests of quantum electrodynamics with high-intensity lasers*  
Christoffer Olofsson

This thesis is electronically published, available at  
<https://hdl.handle.net/2077/75421>

Department of Physics  
University of Gothenburg  
SE-412 96 Gothenburg  
Sweden

Telephone: +46 (0)31-786 00 00

Printed by Stema Specialtryck AB  
Borås, Sweden 2023



## ABSTRACT

Charged particles emit radiation in the presence of strong electromagnetic fields. Emission implies a recoil on the charge, altering its dynamics and is referred to as radiation reaction (RR). Current experiments are on the verge of probing the quantum regime of RR by usage of intense laser pulses colliding with high-energy electron beams. The framework for quantum RR is described by quantum electrodynamics (QED) and becomes nonperturbative in the strong-field limit (SFQED). Theoretical knowledge beyond it is limited but could potentially be detectable with upcoming laser facilities. Here, the presence of electron-positron cascades and low-energy emissions masks any signal emergent in such experiments. Hence, the appeal for strategies to extract signals of SFQED and/or the adoption of advanced statistical techniques. In this thesis, strategies are developed to retrieve information in laser-electron experiments. Firstly, a selection rule is established based on the kinematic properties of electrons and their emissions to form a descriptive reading at the detector. Secondly, the role of tight focusing of lasers is explored to attain extreme regimes of interest. The optimal solution for this is derived and is denoted a bidipole wave. Finally, an experimental framework capable of inferring parameters of models designated to capture SFQED effects using Bayesian techniques is proposed.

Keywords: laser, plasma, accelerator, experiment, radiation reaction, QED, Bayesian inference



## LIST OF PAPERS

This thesis consists of an introductory text outlined in part I and the following two appended papers as well as their summaries, found in Part II:

### **Paper A**

C. OLOFSSON AND A. GONOSKOV. "Attaining a strong-field QED signal at laser-electron colliders with optimized focusing". *Physical Review A* **106.6** (2022), p.063512.

### **Paper B**

C. OLOFSSON, A. GONOSKOV. "Prospects for statistical tests of strong-field quantum electrodynamics with high-intensity lasers".  
*arXiv preprint: arXiv:2303.00568*.

## MY CONTRIBUTIONS

My contributions to the appended papers are:

### **Paper A**

I performed and illustrated the simulations corresponding to Fig. 5. I worked with the theoretical derivations that aim to describe the bidipole structure and engaged in the overall writing of the paper.

### **Paper B**

I am responsible for all simulations and figures appearing in this paper. The writing of the manuscript was shared equally between the authors.

## ACKNOWLEDGEMENTS

First and foremost I need to express my sincerest gratitude to my supervisor Arkady Gonoskov. Not only has he provided me the opportunity to pursue a PhD in laser-plasma physics but he also holds the traits of a great supervisor; modest, encouraging, knowledgeable and very supportive of my work and in my transition into fatherhood. Further, I would like to convey individual appreciation to the rest of my research group:

Tom Blackburn for providing a brilliant collaboration on the course in quantum mechanics as well as our chats and discussions. He also comes with a great sense of humour, seemingly endless expertise in our area of physics and gives captivating talks at seminars and conferences.

Mattias Marklund for being the pillarstone of our group and such an inspiring and likeable guy. Humorously, some consider his physical appearance rare but people often forget his great responsibility at the Swedish Research Council and the time dedicated for traveling.

Mathias Samuelsson for constituting a new asset to our group. We might not know each other well yet but I look forward in doing so.

Shikha Bhadoria for being so kind and supportive whenever I give a talk or I have questions on something. We share a similar mindset on many things, especially within research and the general philosophy of life. She is a great researcher and is very knowledgeable and humble in her field of study.

Joel Magnusson for always brightening the mood whenever I arrive at the office. He might believe I am annoyed by all the things he shows me or talks about but in fact it is these things I appreciate greatly. The only exception would be in sharing the conundrum of the square-triangle. He is very clever and in my view, holds a lot of sensible opinions on life.

Lastly, I thank my loving fiancée Mikaela. Being pregnant with our daughter and taking care of our amazing son Harry she is the reason I could finish this thesis. Their support means everything to me. I thank my parents and my brother because they truly know my affection for working in Physics.

# CONTENTS

<b>Introduction</b>	<b>1</b>
<b>I Theoretical principles and methods</b>	<b>9</b>
<b>1 The nexus of charged particles and electromagnetic fields</b>	<b>9</b>
1.1 Radiation from charged particles in electromagnetic fields . . . . .	10
1.2 Transition to relativistic formulation . . . . .	13
1.3 Classical radiation reaction . . . . .	15
1.4 Landau & Lifshitz approach to radiation reaction . . . . .	20
1.5 Quantum regime of radiation reaction . . . . .	22
1.6 Photon emission and pair-generation . . . . .	23
<b>II Analysis and results</b>	<b>27</b>
<b>2 Extraction of SFQED signals and optimal focusing</b>	<b>27</b>
2.1 Signal extraction and cascade development . . . . .	28
2.2 Optimal focusing . . . . .	32
2.3 Optimal focusing : field strength . . . . .	33
2.4 Additive property of multipoles . . . . .	36
2.5 Optimal focusing : maximization of $\chi$ . . . . .	38
2.6 Structure of the bidipole wave . . . . .	40
<b>3 Bayesian approach to radiation reaction</b>	<b>44</b>
3.1 Bayesian inference . . . . .	44
3.2 Likelihood mitigation . . . . .	46
3.3 Approximate Bayesian computation . . . . .	48
3.4 Effective mass model . . . . .	51
3.5 Latent variable elimination . . . . .	54
<b>4 Current and upcoming research</b>	<b>57</b>
4.1 Summary of paper A . . . . .	57
4.2 Summary of paper B . . . . .	61
4.3 Conclusions . . . . .	63
<b>References</b>	<b>65</b>
<b>5 Research papers</b>	<b>73</b>





# Introduction

From the first notion on stimulated emission by Albert Einstein [1] and the advent of the maser oscillator [2] the idea of generating coherent radiation at sub-millimeter and infrared wavelengths paved the way for the first laser observed in ruby crystals [3–5]. The basic principle of a laser require a gain medium, a pump source and a set of mirrors (optical resonator). The gain medium can be a gas, liquid or a solid compound whose electrons are excited to a higher energy state by e.g. an electrical current or light of a different wavelength. By bouncing between the set of mirrors the emitted photons traverse the media multiple times, each time stimulating emission and amplifies into a coherent beam of radiation. Over the decades the laser found several applications such as cornea reshaping, destruction of tumors and gallstones [6] but also uses in photography and interferometry [7]. A number of laser media can operate in a continuous-wave mode meaning that the output power of the light is constant in time. In contrast, the medium can be intentionally made to only yield intense bursts of light with a certain duration and rate of repetition. These are referred to as pulsed lasers and the effort to make them as short and intense as possible is central in controlling the electron motion in solids [8], tunneling of electrons in nanodevices [9] and areas of attosecond physics [10–13].

As intensity is the energy transferred per unit time and per unit area it becomes clear that intense lasers are attained by 1) increasing the total input energy, 2) focus said radiation to a small spot and 3) decreasing the pulse duration. Combining all of these can result in extreme intensities, raising the question what level can be reached with present-day laser facilities? This is best answered with the aid of Fig. 1 where the timeline of record peak intensities obtained with high-intensity lasers are shown. Shortly after the first laser came the technique of Q-switching where an attenuating element is introduced to the traditional laser setup [15]. The component prevents lasing and results in a large buildup of energy in the gain medium, producing a short and intense laser pulse once the attenuator is deactivated. In close succession came mode-locking, a method where the longitudinal modes of the laser is made to interfere constructively, resulting in bursts of light [16]. Then, in the mid 1980s a drastic increase in peak intensity emerged

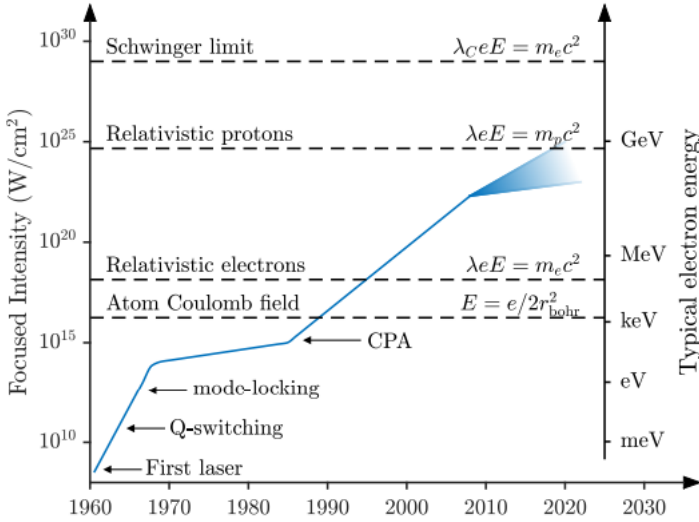


**Figure 1:** History of record peak intensities attained with high-intensity lasers. Typical electron energies obtained at these intensities with a laser wavelength of  $\lambda = 1 \mu\text{m}$  are displayed on the right axis. The shaded area correspond to the range of intensities that upcoming 10 PW facilities might produce. Figure adapted from [14].

with the technique of chirped pulse amplification (CPA) by Strickland and Mourou [17], awarding them the 2018 Nobel Prize in Physics. CPA is used to further amplify ultra-short laser pulses by elongating them in time, ensuring a safe amplification of the long pulse which in the end is compressed, having drastically increased in peak power. In the 1990s, a useful variation of this technique known as optical parametric CPA (OPCPA) was discovered [18] and was employed by several facilities [19, 20].

In terms of peak laser power, contemporary facilities can now reach the order of 1 PW [21, 22] and have recently topped the 10 PW level [23]. More facilities are in development to reach this level [24–27] and even the 100 PW barrier [28]. A comprehensive overview of laser facilities can be seen in Fig. 2 in which they are placed on a map in terms of their pulse energy and duration.

With the ample number of ultra-intense laser facilities one might ask the question what the practicality of these pulses are? In the field of laser-plasma physics, examples range from electron/ion acceleration, high-harmonic generation (HHG) and inertial confinement fusion (ICF) [29]. However, at these extreme intensities there is an opportunity to conduct studies of the fundamental theory of light-matter interactions which is dictated by quantum electrodynamics (QED). Its framework, originally developed during the 1930s by Dirac, Heisenberg and Weisskopf and later finalized by Feynman, Schwinger, Dyson, Tomonaga and others encompass any process where one or several photons interact with electrons or positrons and so forth [30]. Common processes predictable with QED include the Breit-Wheeler process [31] and nonlinear inverse Compton scattering [32]. QED also predicts that in the presence of an exceptionally intense field, electron-positron pairs can spontaneously emerge from the vacuum which is known as the Sauter-Schwinger mechanism [33]. Unfortunately, no facility in the near future can reach the critical field required for this to happen;  $E_{\text{cr}} = m_e^2 c^3 / q_e \hbar \simeq 10^{18} \text{ V m}^{-1}$  where  $\hbar$  is the reduced Planck constant,  $c$  is the speed of light,  $m_e$  and  $q_e$  are the electron mass and charge respectively. For optical wavelengths this translates to intensities  $\approx 10^{29} \text{ W cm}^{-2}$  which is six orders of magnitude greater than the current intensity record ( $\approx 10^{23} \text{ W cm}^{-2}$ ) [34]. Probing such strong-field QED (SFQED) processes in an all-optical environment using e.g. laser-laser collisions is thus demanding.

Question is, are there other schemes to study SFQED processes experimentally? If one consider the collision of a high-intensity laser and a beam of high-energy electrons the situation becomes different. In the rest frame of the electron, the particle will experience a Lorentz boosted electromagnetic field. Depending on the energy of the electrons they can experience field strengths on the order of the critical field and hence entail strong-field processes. As a quantitative measure one can form the quantum nonlinearity parameter  $\chi$  as the ratio of the electron acceleration in said rest frame to the acceleration caused solely by  $E_{\text{cr}}$ . Additionally, electrons (all charged particles in fact) emit radiation when they are accelerated by electromagnetic fields and their response to it is commonly known as radiation reaction. In the classical limit  $\chi \ll 1$  and particles emit radiation continuously of which synchrotron radiation is an example of this [35]. When the combination of strong fields and high-energy electrons reach magnitudes of  $\chi \gtrsim 1$  the emissions become of

discrete nature where individual photons are radiated away probabilistically and various quantum effects emerge such as pair creation [36]. A map of interactions relevant to laser-electron dynamics is found in Fig. 3 as a function of  $\chi$  and  $a_0$ . Here,  $a_0$  is the normalized electric field amplitude of the laser where  $a_0 \approx 1$  designates the field amplitude necessary to accelerate electrons to relativistic energies within a single oscillation of the electromagnetic wave.

On the subject of limits, scientists have always pushed the boundaries of theories to their extremities and the theory of QED is no exception. It is conjectured that the theory becomes non-perturbative when  $\alpha_f \chi^{2/3} \gtrsim 1$  [38, 39] where  $\alpha_f \approx 1/137$  is the fine-structure constant. In other words, the perturbation approach fails to work in this limit and the theory beyond it is limited. Consulting Fig. 3 once more it becomes evident that both contemporary and past experimental efforts (numbered green circles) have made prospects around the quantum regime  $\chi \sim 1$  [40–43] and is far away from the conjectured breakdown. In this thesis, several concepts to probe this domain from an experimental point of view is demonstrated.

The thesis is divided into two parts. Part I entail theoretical principles of radiation from accelerated charges and radiation reaction, forming six sections. The opening sections derive the classical result of J. J. Larmor which concerns the radiated power from an accelerated charge (Sec. 1.1) and extend this result to include relativistic motion and analyze the radiation pattern (Sec. 1.2). Since the emitting charge responds to its own radiation, classical RR is discussed by analyzing the resulting force on the charge  $\mathbf{F}_{\text{rad}}$  (Sec. 1.3). One shall find that the shape of  $\mathbf{F}_{\text{rad}}$  is deficient and leads to nonphysical solutions which are remedied by finding the relativistic generalization by consulting the work of L. Landau and E.M. Lifshitz (Sec. 1.4). In covering the classical and relativistic approach to RR, the question on how to express RR in the quantum picture is posed. The answer will be that the formulation need to encompass the discreteness of individual photons and the possibility to create electron-positron pairs which is described by QED (Sec. 1.5). Part I is concluded by discussing the quantum processes of interest (Sec. 1.6) obtained using QED; photon emission (nonlinear Compton scattering) and electron-positron pair creation (Breit-Wheeler process).

Part II is devoted to provide solutions to some of the difficulties faced in

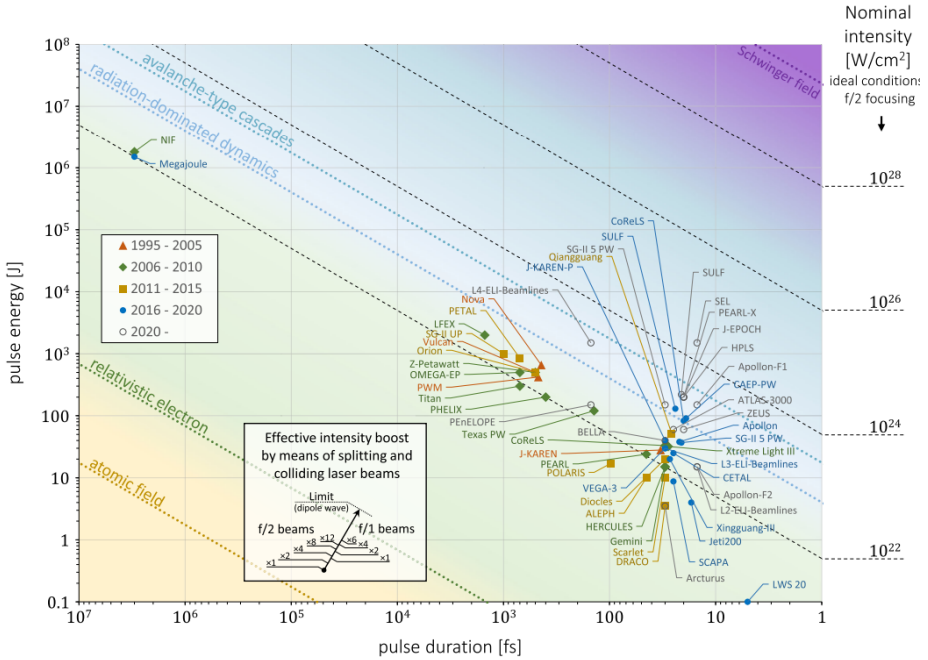


**Figure 2:** Laser facilities in the space of pulse duration and energy assuming a linearly polarized laser with spatiotemporal Gaussian profile, wavelength  $\lambda = 1 \mu\text{m}$  and ideal  $f/2$  focusing. Colored regions show regions of attainable physics; (yellow) intensity corresponding to one atomic unit of field strength ( $\approx 3.5 \cdot 10^{16} \text{ W cm}^{-2}$ ), (green) relativistic electrons ( $a_0 \approx 1 \implies \approx 1.37 \cdot 10^{18} \text{ W cm}^{-2}$ ), (blue) radiation losses of an electron become comparable to the energy gain from the acceleration in the electromagnetic field during each laser cycle. ( $\approx 8 \cdot 10^{22} \text{ W cm}^{-2}$ ), (teal) cascading of electron-positron pairs commence ( $\approx 3.5 \cdot 10^{23} \text{ W cm}^{-2}$ ) and (violet) intensity equivalent to the critical field  $E_{\text{Cr}}$  ( $\approx 4.65 \cdot 10^{29} \text{ W cm}^{-2}$ ). The inset displays the effective intensity boost by splitting the laser power between the given number of beams and adding the electric field coherently. This is shown as a relative shift on the map between the cases of  $f/2$  (left) and  $f/1$  (right) focusing in which the dotted line displays the optimal limit: a dipole wave. Adapted from [37].

laser-electron experiments that aim to probe the extreme regimes of QED. Experimentalists are now equipped with lasers and accelerators whose combined capabilities are enough to observe quantum effects ( $\chi \gtrsim 1$ ) but there is an active appeal to yield larger values of  $\chi$  to study the breakdown regime

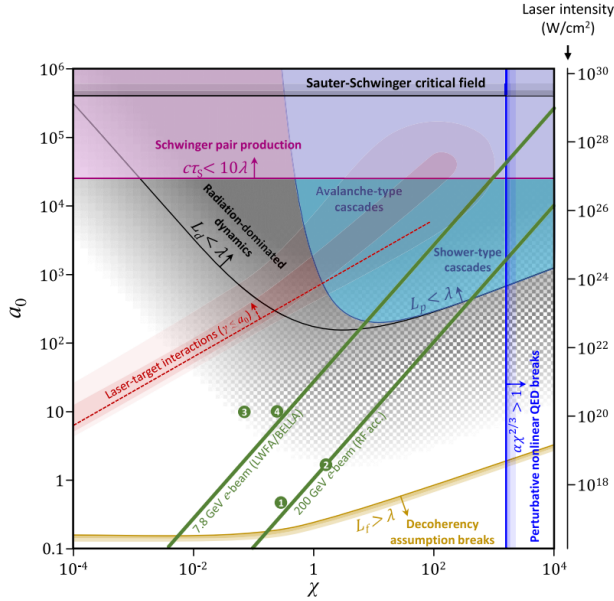


**Figure 3:** Interaction map in the space of the quantum nonlinearity parameter  $\chi$  and dimensionless laser (assumed wavelength  $\lambda = 1 \mu\text{m}$ ) amplitude  $a_0$ : (black solid line) delimits dynamics in which electrons radiate away the majority of their energy where  $L_d$  denote the distance over which the electron has lost all of its energy due to emissions, (checkered area) demarcates whether radiation can be described as continuous (white) or individual photons (checkered), (shaded blue region) domain where the process of electron-positron pair creation becomes significant where  $L_p$  denote the average distance before generating a pair, (shaded violet region) the onset of vacuum pair-production, (yellow line) boundary for which the electromagnetic field can be considered constant where  $L_f$  is the distance required for an electron to emit a photon, (solid blue line) nonperturbative limit of QED, (dashed red line/shaded red area) prospects for experiments using stationary plasma targets and (solid green line) experiments involving an ultrarelativistic electron beam where the numbered points highlight past and contemporary experiments (1)-[41], (2)-[40], (3)-[42] and (4)-[43]. Adapted from [37].

of QED ( $\chi \gtrsim 1600$ ). One approach to detect it is to consider the resulting energy spectrum of electrons and their emitted photons to identify a deviation from what has previously been measured and/or predicted with QED. Nonetheless, the difficulty lies in distinguishing such a deviation possibly

minuscule as  $\chi \ll 1600$ , from the vast majority of background *noise* inherent in such experiments operating at these extremities (Sec. 2.1). In this thesis, concepts that circumvent these difficulties are provided which comprise of three milestones outlined in chapters 2 and 3. Firstly, a strategy to extract information from these experiments based on the kinematic traits of photons emitted from electrons is developed, which provides a feasible way of separating the background noise. Secondly, the optimization problem that results in the maximum achievable  $\chi$  in laser-electron collisions is defined. This is then solved which yields a solution whose structure is shown to be feasible in terms of implementation in experiments. Lastly, prospects of experiments incorporating Bayesian inference by comparing results from repeated simulations and experiments are demonstrated. The summaries of papers A and B can be found in Secs. 4.1 and 4.2.





# PART I

## THEORETICAL PRINCIPLES AND METHODS

### 1 The nexus of charged particles and electromagnetic fields

This chapter covers the basic ideas behind radiation from accelerated charges in electromagnetic fields and the concept of radiation reaction which span six sections. In Sec. 1.1 the total instantaneous power emitted from a non-relativistic charge being accelerated is derived. Obtaining the result is done by calculating the electromagnetic potentials from the current density arising from the moving charge. These can later be used in evaluating the *Poynting vector* which describes the instantaneous energy flux. In Sec. 1.2 the relativistic formulation in which the charge may have arbitrary velocity is attained. This is done by invoking Lorentz covariance onto the previous result which must reduce to the classical expression for velocities much smaller than  $c$ . Sec. 1.3 considers the impact on the radiating charge responding to its own emission which can be encapsulated by a force  $\mathbf{F}_{\text{rad}}$ . In finding its expression, Newton's second law in conjunction with the conservation of momentum within a spherically symmetric and *robust* charge is employed. Sec. 1.4 points out that  $\mathbf{F}_{\text{rad}}$  admits nonphysical solutions which is resolved by again appealing to Lorentz covariance. Lastly, in Secs. 1.5 and 1.6 the quantum formulation of radiation reaction is introduced which no longer treats the coaction between the emitting charge and its radiation as a continuous process. Instead, the emission and absorption of individual photons becomes the dominant feature and the generation of electron-positron pairs becomes possible. Such a description is provided with QED for which the specific focus is on processes connected to photon emission and electron-positron pair production. The following derivations are based on Refs. [44–48].

## 1.1 Radiation from charged particles in electromagnetic fields

All charged particles radiate when accelerated, hence they must lose energy due to conservation of energy. The radiation itself may be dependent on the trajectory, velocity and/or other traits of the particle in question. In this section, the spectral properties of an accelerated, non-relativistic charge is derived. This will serve as a stepping stone in describing radiation reaction and its relativistic variations.

To begin with, the electromagnetic field vectors are denoted as  $\mathbf{E}$  and  $\mathbf{B}$ . These are required to calculate the emitted power which is directly related to the Poynting vector, representing the energy flux of an electromagnetic field

$$\mathbf{S} = \frac{c}{4\pi} \mathbf{E} \times \mathbf{B}. \quad (1.1)$$

All electromagnetic fields obey the Maxwell equations and can be further expressed using potentials:

$$\mathbf{E} = -\nabla\phi - \frac{\partial \mathbf{A}}{\partial t}, \quad (1.2)$$

$$\mathbf{B} = \nabla \times \mathbf{A} \quad (1.3)$$

where  $\phi$  has been introduced as the scalar potential and  $\mathbf{A}$  as the vector potential. A relativistic description of  $\phi$  and  $\mathbf{A}$  is achieved by introducing the four-vector  $A_\mu = (\mathbf{A}, \phi)$ . Here, the metric tensor is chosen to have signature  $\eta_\mu = (-, +, +, +)$ . In the case of a localized charge the potential  $A_\mu$  at any time  $t$  can be written [44]

$$A_\mu(\mathbf{r}, t) = \frac{1}{c} \int \int \frac{J_\mu(\mathbf{r}', t')}{|\mathbf{r} - \mathbf{r}'|} \delta\left(t' + \frac{|\mathbf{r} - \mathbf{r}'|}{c} - t\right) dV' dt' \quad (1.4)$$

where  $J_\mu = (\mathbf{J}, c\rho)$  is the four-current density with spatial components equivalent to the current density  $\mathbf{J}$  and temporal component  $\rho$  being the charge density and  $\mathbf{r} = (x, y, z)$  is the coordinate vector. Here,  $\delta(\cdot)$  denotes the Dirac delta function. Considering a single particle with charge  $q$  and four-velocity

$v_\mu = (\gamma \mathbf{v}, \gamma c)$  where  $\mathbf{v}$  is the particle velocity and  $\gamma = \frac{1}{\sqrt{1 - \frac{v^2}{c^2}}}$  is its corresponding Lorentz factor ( $v = |\mathbf{v}|$ ) it is straightforward to express the four-current density as

$$J_\mu(\mathbf{r}, t) = q v_\mu \delta(\mathbf{r} - \mathbf{r}_p(t)) \quad (1.5)$$

where  $\mathbf{r}_p(t)$  is the location of the particle in space and at time  $t$ . With  $J_\mu$  given by Eq. (1.5) the spatial integration in (1.4) can be carried out effortlessly due to the spatial delta function

$$\begin{aligned} A_\mu(\mathbf{r}, t) &= \frac{q}{c} \int \int \frac{v_\mu(\mathbf{r}', t')}{|\mathbf{r} - \mathbf{r}'|} \delta(\mathbf{r}' - \mathbf{r}_p(t')) \delta\left(t' + \frac{|\mathbf{r} - \mathbf{r}'|}{c} - t\right) dV' dt' \quad (1.6) \\ &= \frac{q}{c} \int \frac{v_\mu(\mathbf{r}_p(t'), t')}{|\mathbf{r} - \mathbf{r}_p(t')|} \delta\left(t' + \frac{|\mathbf{r} - \mathbf{r}_p(t')|}{c} - t\right) dt' \end{aligned}$$

where the following property of delta functions has been used

$$\int f(x') \delta(x - x') dx' = f(x). \quad (1.7)$$

Determining the fields can be done directly with Eq. (1.6) by introducing  $\mathbf{R} = \mathbf{r} - \mathbf{r}_p(t')$  noting that the gradient operator reduces to

$$\nabla \rightarrow \nabla \mathbf{R} \frac{\partial}{\partial R} = \mathbf{n} \frac{\partial}{\partial R} \quad (1.8)$$

where  $\mathbf{n}$  is the unit vector directed from the charge location to the point of observation. This is possible since the only dependence on spatial coordinates  $\mathbf{r}$  is through  $R = |\mathbf{R}|$ . Employing Eq. (1.2) one finds that

$$\begin{aligned} \mathbf{E}(\mathbf{r}, t) &= q \int \frac{\mathbf{n}}{R^2} \delta\left(t' + \frac{R}{c} - t\right) + \frac{1}{cR} (\mathbf{v}/c - \mathbf{n}) \frac{\partial \delta}{\partial R} \left(t' + \frac{R}{c} - t\right) dt' \quad (1.9) \\ &= q \int \frac{\mathbf{n}}{\kappa R^2} \delta(t_{\text{ret}} - t) + \frac{1}{\kappa c R} (\mathbf{v}/c - \mathbf{n}) \frac{\partial \delta}{\partial R} (t_{\text{ret}} - t) dt_{\text{ret}} \end{aligned}$$

where in the last line the substitution  $t_{\text{ret}} = t' + \frac{R(t')}{c}$  and abbreviation  $\kappa = 1 - \frac{v}{c}$  has been made. From Eq. (1.9) the derivative on the delta function can be integrated by parts, giving

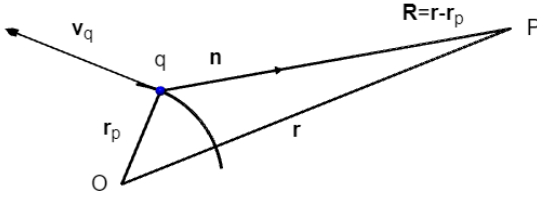


**Figure 1.1:** Geometrical illustration of a charged particle trajectory showing relevant quantities that appear in the derivation of its emitted radiation. Here, O and P denote the origin and point of observation respectively.

$$\mathbf{E}(\mathbf{r}, t) = q \left[ \frac{\mathbf{n}}{\kappa R^2} + \frac{1}{c\kappa} \frac{d}{dt'} \left( \frac{\mathbf{n} - \mathbf{v}/c}{\kappa R} \right) \right]_{t'=t_{\text{ret}}} . \quad (1.10)$$

Although not shown here, the calculation of  $\mathbf{B}$  reveals that it is related to the electric field in the following way

$$\mathbf{B} = \mathbf{n} \times \mathbf{E}. \quad (1.11)$$

The final thing to do is to evaluate the derivative on the second term in Eq. (1.10). For this, the following identities are consulted

$$\frac{d\mathbf{n}}{dt'} = \frac{\mathbf{n} \times (\mathbf{n} \times \mathbf{v})}{R} \quad (1.12)$$

$$\frac{dv}{dt'} = \dot{v} \quad (1.13)$$

$$\frac{d}{dt'}(\kappa R) = \frac{v^2}{c} - \mathbf{v} \cdot \mathbf{n} - \frac{R}{c} \mathbf{n} \cdot \dot{\mathbf{v}}. \quad (1.14)$$

To convince oneself of Eq. (1.12), a brief look at Fig. 1.1 indicates that the time rate of change of  $\mathbf{n}$  will be the negative ratio of the perpendicular components

of  $\mathbf{v}$  to that of  $R$ . Thus, using Eqs. (1.12)-(1.14) in Eq. (1.10) the electric field will be given by

$$\mathbf{E}(\mathbf{r}, t) = \frac{q}{\gamma^2 \kappa^3 R^2} [\mathbf{n} - \mathbf{v}/c]_{t'=t_{\text{ret}}} + \frac{q}{c \kappa^3 R} [\mathbf{n} \times ((\mathbf{n} - \mathbf{v}/c) \times \dot{\mathbf{v}}/c)]_{t'=t_{\text{ret}}}. \quad (1.15)$$

Note that  $\mathbf{E}$  comprise of two parts. The first depends linearly on the particle velocity, diminishing as  $R^{-2}$  whereas the second contribution depend on the particle acceleration, falling off as  $R^{-1}$ . In the non-relativistic case, a reference frame where the particle velocity  $v \ll c$  but its acceleration is non-negligible can be considered so that Eq. (1.15) simplifies to

$$\mathbf{E}(\mathbf{r}, t) = \frac{q}{c^2} \left[ \frac{\mathbf{n} \times (\mathbf{n} \times \dot{\mathbf{v}})}{R} \right]_{t'=t_{\text{ret}}}. \quad (1.16)$$

Recall that the power can be obtained through the Poynting vector (Eq. (1.1))

$$\mathbf{S} = \frac{c}{4\pi} \mathbf{E} \times \underbrace{(\mathbf{n} \times \mathbf{E})}_{=\mathbf{B}} = \frac{c}{4\pi} |\mathbf{E}|^2 \mathbf{n} \quad (1.17)$$

and because  $|\mathbf{S}| = \frac{dP}{dA} = \frac{dP}{R^2 d\Omega}$ , the power radiated per unit solid angle is

$$\frac{dP}{d\Omega} = \frac{c}{4\pi} |\mathbf{E}|^2 R^2 = \frac{q^2}{4\pi c^2} |\mathbf{n} \times (\mathbf{n} \times \dot{\mathbf{v}})|^2. \quad (1.18)$$

Further, introducing the angle  $\Theta$  so that  $\dot{\mathbf{v}} \cdot \mathbf{n} = \dot{v} \cos(\Theta)$  enables one to compute the total instantaneous radiated power

$$P = \int \underbrace{\frac{q^2}{4\pi c^3} \dot{v}^2 \sin^2(\Theta)}_{\frac{dP}{d\Omega}} d\Omega = \frac{q^2}{4\pi c^3} \cdot 2\pi \underbrace{\int_0^\pi \sin^3(\Theta) d\Theta}_{=4/3} = \frac{2}{3} \frac{q^2 \dot{v}^2}{c^3} \quad (1.19)$$

which is the famous result of J. J. Larmor for a non-relativistic charge being accelerated [49].

## 1.2 Transition to relativistic formulation

One can argue that there should exist a Lorentz transformation to a frame of reference for arbitrary particle velocity. Additionally, the power  $P$  is a Lorentz

invariant [50]. Thus, if one can find a suitable Lorentz invariant for the right-hand side of Eq. (1.19) which reduce to the non-relativistic expression in the limit  $v \ll c$  then one has the desired result. Realizing that the electric field emitted from the particle according to Eq. (1.16) depend on  $\mathbf{v}$  and  $\dot{\mathbf{v}}$  implies that the relativistic form also need to depend only on these. To highlight the correct choice of the Lorentz invariant, the Larmor formula (1.19) can be expressed using the particle momentum  $\mathbf{p}$

$$P = \frac{2}{3} \frac{q^2}{m^2 c^3} \left( \frac{d\mathbf{p}}{dt} \frac{d\mathbf{p}}{dt} \right) \quad (1.20)$$

where  $m$  is the mass of the particle. Now the choice is obvious,  $\frac{d\mathbf{p}}{dt} \rightarrow \frac{dp_\mu}{d\tau}$  where  $d\tau = dt/\gamma$  is the proper infinitesimal time,  $p_\mu = (\mathbf{p}, E/c)$  is the four-momentum of the particle and  $E$  its energy. Then the relativistic generalization must be

$$P = \frac{2}{3} \frac{q^2}{m^2 c^3} \left( \frac{dp_\mu}{d\tau} \frac{dp^\mu}{d\tau} \right) \quad (1.21)$$

with an implicit sum over the indices. Evaluating the above four-product yields

$$\frac{dp_\mu}{d\tau} \frac{dp^\mu}{d\tau} = \left( \frac{d\mathbf{p}}{d\tau} \right)^2 - \frac{v^2}{c^2} \left( \frac{dp}{d\tau} \right) \quad (1.22)$$

where  $p = |\mathbf{p}|$  which indeed reduce to Eq. (1.19) when  $v \ll c$ . It is possible to put Eq. (1.21) in a non-covariant form by expressing  $E = mc^2\gamma$  and  $\mathbf{p} = m\mathbf{v}\gamma$ . Then, Eq. (1.21) takes the form

$$P = \frac{2}{3} \frac{q^2}{c^3} \left( \left( \frac{\dot{\mathbf{v}}}{c} \right)^2 - \left( \frac{\mathbf{v}}{c} \times \frac{\dot{\mathbf{v}}}{c} \right)^2 \right) \quad (1.23)$$

which was originally found by Liénard [51]. Evidently, the radiated power now depend on both the particle velocity and its acceleration, making the angular distribution more complex than that of Eq. (1.18). However, consider the example of linear motion and when the charge is accelerated for a short period of time. Then, if the emission is observed from far away one finds [44]

$$\frac{dP}{d\Omega} = \frac{q^2 \dot{v}^2}{4\pi c^3} \frac{\sin^2 \Theta}{\left(1 - \frac{v}{c} \cos \Theta\right)^5} \quad (1.24)$$

where  $\Theta$  is the angle of observation measured from the joint direction of  $\mathbf{v}$  and  $\dot{\mathbf{v}}$ . This also approach Eq. (1.18) when  $v \ll c$ . The radiation pattern now emerge as two lobes tilted toward the direction of propagation as opposed to the non-relativistic result where the lobes are perpendicular to the propagation axis.

### 1.3 Classical radiation reaction

Perhaps one of the most well-known forces related to the motion of charges in an electromagnetic field is that of the Lorentz force [52, 53]

$$\mathbf{F}_l = q \left( \mathbf{E} + \frac{\mathbf{v}}{c} \times \mathbf{B} \right) \quad (1.25)$$

with the velocity of the charge being constant. Note that  $\mathbf{E}, \mathbf{B}$  now denote external electromagnetic field vectors. Coincidentally, by Newtons second law the charge in question must experience an acceleration  $\dot{\mathbf{v}} = \frac{\mathbf{F}_l}{m}$  which must give rise to emission of radiation according to Sec. 1.1. Emitting particles must lose energy and deposit its momentum as well as angular momentum to the radiation. This alters the equations of motion for the charge and Eq. (1.25) is not enough to describe trajectories for situations where the energy loss is non-negligible. This suggests that there should exist an additional force term  $\mathbf{F}_{\text{rad}}$  which capture the correct dynamics. The description of a charged particle, including the self-force from its emitted radiation dates back to the attempts of Abraham and Lorentz [45–47]. In what follows, the discussion of [44] is adopted in order to unravel the form of  $\mathbf{F}_{\text{rad}}$  and one shall find that this form is incorrect and admits nonphysical solutions.

Similar to Sec. 1.1, one can consider a particle with charge  $q$  and strongly localized charge density  $\rho(\mathbf{r})$  present in electromagnetic fields  $\mathbf{E}$  and  $\mathbf{B}$ . To commence the analysis, acknowledge the fact that the rate of change of total momentum is conserved within the volume of the charge

$$\frac{d}{dt} (\mathbf{P}_{\text{mech}} + \mathbf{P}_{\text{EM}}) = 0 \quad (1.26)$$

where  $\mathbf{P}_{\text{mech}}$  and  $\mathbf{P}_{\text{EM}}$  are the mechanical momentum and electromagnetic momentum respectively. Under the assumption that the mechanical mo-

momentum is of electromagnetic origin (as Abraham and Lorentz argued) then Eq. (1.26) can be expressed in terms of the Lorentz force

$$\int \mathbf{F}_l dV = \int \left( \rho \mathbf{E}_{\text{tot}} + \frac{1}{c} \mathbf{J} \times \mathbf{B}_{\text{tot}} \right) dV = 0 \quad (1.27)$$

where the integral runs over the volume of the particle and  $\mathbf{E}_{\text{tot}}, \mathbf{B}_{\text{tot}}$  are the total fields

$$\begin{aligned} \mathbf{E}_{\text{tot}} &= \mathbf{E} + \mathbf{E}_{\text{rad}}, \\ \mathbf{B}_{\text{tot}} &= \mathbf{B} + \mathbf{B}_{\text{rad}} \end{aligned}$$

being composed of the external ones and the fields related to the emitted radiation  $\mathbf{E}_{\text{rad}}, \mathbf{B}_{\text{rad}}$ . In turn, the integral (1.27) decompose to

$$\mathbf{F} = \int \left( \rho \mathbf{E} + \frac{1}{c} \mathbf{J} \times \mathbf{B} \right) dV, \quad (1.28)$$

$$\mathbf{F}_{\text{rad}} = \int \left( \rho \mathbf{E}_{\text{rad}} + \frac{1}{c} \mathbf{J} \times \mathbf{B}_{\text{rad}} \right) dV \quad (1.29)$$

and implies that  $-\frac{d\mathbf{p}}{dt} = \mathbf{F}_{\text{rad}}$  where  $\mathbf{p} = \mathbf{P}_{\text{mech}}$  is the particle momentum. To evaluate Eq. (1.29) two assumptions must be made to simplify the calculation. First, assume that the charge is instantaneously at rest and secondly, that the charge distribution is spherically symmetric and robust. The latter implies  $\mathbf{J}(\mathbf{r}, t) = \rho(\mathbf{r}, t) \cdot \mathbf{v}(t)$ , that is, every part of the charge travels with the same velocity. From these assumptions one has  $\mathbf{v} = 0 \rightarrow \mathbf{J} = 0$  and Eq. (1.29) collapse to

$$\frac{d\mathbf{p}}{dt} = - \int \rho(\mathbf{r}, t) \mathbf{E}_{\text{rad}}(\mathbf{r}, t) dV. \quad (1.30)$$

Recall from Eq. (1.2) that the electric field can be expressed in terms of the potentials  $\phi$  and  $\mathbf{A}$  so that

$$\frac{d\mathbf{p}}{dt} = \int \rho(\mathbf{r}, t) \left( \nabla \phi(\mathbf{r}, t) + \frac{1}{c} \frac{\partial \mathbf{A}(\mathbf{r}, t)}{\partial t} \right) dV \quad (1.31)$$



where it is understood that  $\phi = \phi_{\text{rad}}$  and  $\mathbf{A} = \mathbf{A}_{\text{rad}}$ . In turn, the potentials are given by Eq. (1.4), hence

$$A_\mu(\mathbf{r}, t) = \frac{1}{c} \int \frac{J_\mu(\mathbf{r}', t' = t_{\text{ret}})}{R} dV' \quad (1.32)$$

where again  $R = |\mathbf{r} - \mathbf{r}'|$ . Here,  $J_\mu$  must be evaluated at the retarded time  $t' = t - \frac{R}{c}$ . However, since the integration spans the extent of the particle the term  $\frac{R}{c} \sim \frac{r_q}{c}$  with  $r_q$  being the spatial dimension of the charge. By the second assumption,  $r_q$  must be exceptionally small due to the highly localized charge distribution. Therefore, one can attempt to Taylor expand Eq. (1.32) around  $t' = t$  in powers of  $-\frac{R}{c}$

$$J_\mu(t') = \sum_{n=0}^{\infty} \frac{(-1)^n}{n!} \left(\frac{R}{c}\right)^n \frac{\partial^n J_\mu(t)}{\partial t^n}. \quad (1.33)$$

Putting Eq. (1.33) into Eq. (1.31) one finds

$$\frac{d\mathbf{p}}{dt} = \sum_{n=0}^{\infty} \frac{(-1)^n}{c^n n!} \int \int \rho(\mathbf{r}, t) \frac{\partial^n}{\partial t^n} \left( \rho(\mathbf{r}', t) \nabla R^{n-1} + \frac{R^{n-1}}{c^2} \frac{\partial \mathbf{J}(\mathbf{r}', t)}{\partial t} \right) dV' dV. \quad (1.34)$$

To facilitate the analysis, consider only the contribution from the scalar potential  $\phi$ . Its first term ( $n = 0$ ) in the expansion is proportional to

$$\begin{aligned} &\propto \int \int \rho(\mathbf{r}, t) \rho(\mathbf{r}', t) \nabla \left( \frac{1}{R} \right) dV' dV \\ &\propto \int \int \rho(\mathbf{r}, t) \rho(\mathbf{r}', t) \frac{\mathbf{r} - \mathbf{r}'}{|\mathbf{r} - \mathbf{r}'|^3} dV' dV = 0 \end{aligned} \quad (1.35)$$

which is true for spherically symmetric charge distributions (reversal of  $\mathbf{r} \rightarrow \mathbf{r}'$  inverts the sign). Here, the identity  $\nabla R^n = nR^{n-2}\mathbf{R}$  is employed. Next, the term  $n = 1$  also has zero contribution due to the term  $\nabla R^{n-1} = \nabla R^0 = 0$ . As a consequence, all non-zero scalar contributions come from  $n \geq 2$  and its sum can be re-expressed by shifting the index  $n$  by +2. Note that the vector potential contribution is non-zero for  $n = 0, 1$  and its indices remain unchanged. Then, Eq. (1.34) can be cast in the following form

$$\frac{d\mathbf{p}}{dt} = \sum_{n=0}^{\infty} \frac{(-1)^n}{n!c^{n+2}} \int \int \rho(\mathbf{r}, t) R^{n-1} \frac{\partial^{n+1}}{\partial t^{n+1}} \left[ \frac{\frac{\partial \rho(\mathbf{r}', t)}{\partial t} \frac{\nabla R^{n+1}}{R^{n-1}}}{(n+2)(n+1)} + \mathbf{J}(\mathbf{r}', t) \right] dV' dV. \quad (1.36)$$

Apart from the momentum conservation in Eq. (1.26), charge must also be conserved. This is formulated using the continuity equation [54]

$$\frac{\partial \rho}{\partial t} + \nabla \cdot \mathbf{J} = 0 \quad (1.37)$$

and states that any charge transported out of a volume must decrease the amount of charge inside that volume. Applying Eq. (1.37) to the current density term in Eq. (1.36) yields

$$\frac{d\mathbf{p}}{dt} = \dots \int \int \rho(\mathbf{r}, t) R^{n-1} \frac{\partial^{n+1}}{\partial t^{n+1}} \left[ \mathbf{J}(\mathbf{r}', t) - \nabla' \cdot \mathbf{J}(\mathbf{r}', t) \frac{\mathbf{R}}{(n+2)} \right] dV' dV \quad (1.38)$$

where  $\nabla'$  denotes differentiation with respect to  $\mathbf{r}'$  and the sum has been omitted for readability. Additionally, the second term in the square brackets can be integrated by parts to yield

$$\frac{d\mathbf{p}}{dt} = \dots \int \int \rho(\mathbf{r}, t) R^{n-1} \frac{\partial^{n+1}}{\partial t^{n+1}} \left[ \frac{(n+1)}{(n+2)} \mathbf{J}(\mathbf{r}', t) - \frac{(n-1)}{(n+2)} \frac{(\mathbf{J} \cdot \mathbf{R}) \mathbf{R}}{R^2} \right] dV' dV. \quad (1.39)$$

According to the second assumption, the spherically symmetric charge distribution suggest that the only relevant direction of the problem is along its velocity  $\mathbf{v}$ . As a result, only the components inside the square brackets of Eq. (1.39) oriented along  $\mathbf{v}$  will survive the integration. Utilizing the robustness of the charge and projecting the components along  $\mathbf{v}$  one can write

$$\frac{d\mathbf{p}}{dt} = \dots \int \int \rho(\mathbf{r}, t) R^{n-1} \frac{\partial^{n+1}}{\partial t^{n+1}} \left[ \rho(\mathbf{r}', t) \mathbf{v} \left( \frac{(n+1)}{(n+2)} - \frac{(n-1)}{(n+2)} \cdot \frac{(\mathbf{R} \cdot \mathbf{v})^2}{R^2 v^2} \right) \right] dV' dV. \quad (1.40)$$

The only angular dependence comes from  $\frac{(\mathbf{R} \cdot \mathbf{v})^2}{R^2 v^2}$  and it can be shown that integrating over the angles for this term gives  $\frac{(\mathbf{R} \cdot \mathbf{v})^2}{R^2 v^2} \rightarrow \frac{1}{3}$ , leading to the simpler expression

$$\frac{d\mathbf{p}}{dt} = \frac{2}{3} \sum_{n=0}^{\infty} \frac{(-1)^n}{n!c^{n+2}} \frac{\partial^{n+1}\mathbf{v}}{\partial t^{n+1}} \int \int \rho(\mathbf{r}')R^{n-1}\rho(\mathbf{r})dV'dV. \quad (1.41)$$

Now, defining the characteristic extent of the charge as

$$r_p^{n-1} \simeq \frac{1}{q^2} \int \int \rho(\mathbf{r}')R^{n-1}\rho(\mathbf{r})dV'dV \quad (1.42)$$

it is possible to see that the  $n$  :th term in the expansion is proportional to

$$\left[ \frac{d\mathbf{p}}{dt} \right]_n \propto r_p^{n-1}. \quad (1.43)$$

Taking the limit of point-like charges ( $r_p \rightarrow 0$ ), only the terms  $n = 0, 1$  contribute to the self-force expression. These contributions read

$$\left[ \frac{d\mathbf{p}}{dt} \right]_{n=0} = \frac{2\dot{\mathbf{v}}}{c^3} \int \int \frac{\rho(\mathbf{r}')\rho(\mathbf{r})}{R} dV'dV = \frac{4}{3} m_q \dot{\mathbf{v}}, \quad (1.44)$$

$$\left[ \frac{d\mathbf{p}}{dt} \right]_{n=1} = \frac{-2\ddot{\mathbf{v}}}{3c^3} \int \int \rho(\mathbf{r}')\rho(\mathbf{r})dV'dV = \frac{-2q^2}{3c^3} \ddot{\mathbf{v}} \quad (1.45)$$

where the electrostatic self-energy has been identified as

$$U = \frac{1}{2} \int \int \frac{\rho(\mathbf{r}')\rho(\mathbf{r})}{R} dV'dV \quad (1.46)$$

and the electromagnetic mass  $m_q = \frac{U}{c^2}$  connecting the self-energy contribution to the mass of the particle. Finally, the expression for the self-force becomes

$$\mathbf{F}_{\text{rad}} = \frac{4}{3} m_q \dot{\mathbf{v}} - \frac{2q^2}{3c^3} \ddot{\mathbf{v}} \quad (1.47)$$

which is the classical result describing the response of a charge to its own electromagnetic radiation. Being a classical result, there is a deficiency of it not being relativistic and possessing incorrect Lorentz covariance (the factor  $\frac{4}{3}$  in Eq. (1.47) is in fact wrong). Additionally, neglecting higher-order terms is not sustainable as the assumption  $r_p \rightarrow 0$  implies  $m_q \rightarrow \infty$ . To resolve this issue, one can at least take the observable mass of the charge for a finite

spatial extent. In the case of electrons one can take  $r_p \sim 10^{-13}$  cm which is the classical electron radius. Despite the smallness of  $r_p$ , it is still possible for the motion to be rapid enough to make contributions beyond  $n \geq 2$  in the expansion important. Thus, the radiation force in Eq. (1.47) can at best be taken as an approximated theory.

## 1.4 Landau & Lifshitz approach to radiation reaction

Considering the difficulties of the self-force derived in Sec. 1.3 one can briefly observe another derivation made by L. Landau and E.M. Lifshitz [48] on classical radiation reaction. In their book they make the remark that the self-force stated by Eq. (1.47) lead to nonphysical solutions. To exemplify, take a charged particle not present in any external field and only affected by  $\mathbf{F}_{\text{rad}} = -\frac{2q^2}{3c^3}\dot{\mathbf{v}}$ . Writing the equation of motion for the particle as

$$m\dot{\mathbf{v}} = \frac{2q^2}{3c^3}\dot{\mathbf{v}} \quad (1.48)$$

the non-constant solution for  $\dot{\mathbf{v}}$  is proportional to  $e^{\frac{3mc^3 t}{2q^2}}$  which increase indefinitely in time. In other words, if a charge were to experience electromagnetic fields for a finite period, it would begin to self-accelerate exponentially in time upon leaving the fields. Before deriving the relativistic case for the self-force, recall that the classical version is only valid as an approximation in the limit  $\frac{|\mathbf{F}_{\text{rad}}|}{|\mathbf{F}_l|} \ll 1$ .

To obtain the relativistic generalization one can use the same arguments as motivated in Sec. 1.2. Now, a four-force  $f_{\mu}^{\text{rad}} = (\frac{\gamma}{c}\mathbf{f} \cdot \mathbf{v}, \gamma\mathbf{f})$  is sought after that reduce to the right-hand side of Eq. (1.48) in the limit  $v \ll c$ . Here,  $\mathbf{f}$  is the three-dimensional vector describing the self-force. Starting off, one can write the equation of motion for the charge in relativistic form

$$m \frac{dv_{\mu}}{d\tau} = q F^{\mu\nu} v_{\nu} + f_{\mu}^{\text{rad}} \quad (1.49)$$

where  $F_{\mu\nu}$  is the electromagnetic tensor given by

$$F_{\mu\nu} = \begin{bmatrix} 0 & E_x/c & E_y/c & E_z/c \\ -E_x/c & 0 & -B_z & B_y \\ -E_y/c & B_z & 0 & -B_x \\ -E_z/c & -B_y & B_x & 0 \end{bmatrix}. \quad (1.50)$$

The shape of  $f_{\mu}^{\text{rad}}$  is built by

$$f_{\mu}^{\text{rad}} = \frac{2q^2}{3c} \frac{d^2 v_{\mu}}{d\tau^2} \quad (1.51)$$

since this retrieves the classical result in the limit  $v \ll c$ . All four-forces must follow the orthogonal property  $f^{\mu} v_{\mu} = 0$  which is not fulfilled by Eq. (1.51). To enforce this requirement one needs to add an auxiliary four-vector to Eq. (1.51) which in turn must have its spatial components go to zero when  $\mathbf{v} \rightarrow 0$ . It turns out that the four-vector  $v_{\mu}$  is sufficient and the inclusion of this auxiliary contribution is written as

$$f_{\mu}^{\text{rad}} = \frac{2q^2}{3c} \frac{d^2 v_{\mu}}{d\tau^2} + \zeta v_{\mu} \quad (1.52)$$

where  $\zeta$  is a constant determined by the condition  $f_{\mu}^{\text{rad}} v^{\mu} = 0$ . Evaluating it leads to

$$\zeta = -\frac{2q^2}{3c^3} \frac{d^2 v_{\mu}}{d\tau^2} v^{\mu} \quad (1.53)$$

giving

$$f_{\mu}^{\text{rad}} = \frac{2q^2}{3c} \left( \frac{d^2 v_{\mu}}{d\tau^2} - \frac{1}{c} \frac{d^2 v^{\nu}}{d\tau^2} v_{\nu} v_{\mu} \right). \quad (1.54)$$

It is possible to write the four-acceleration in terms of the external field using

$$\frac{d v^{\mu}}{d\tau} = \frac{q}{m} F^{\mu\nu} v_{\nu} \rightarrow \quad (1.55)$$

$$\rightarrow \frac{d^2 v^{\mu}}{d\tau^2} = \frac{q}{m} \frac{\partial F^{\mu\nu}}{\partial x_{\gamma}} v_{\nu} v^{\gamma} + \frac{q^2}{m^2} F^{\mu\nu} F_{\nu\gamma} v^{\gamma}.$$

As the final step, substitute Eq. (1.55) into Eq. (1.54) recalling that the inner product between the antisymmetric tensor  $\frac{\partial F^{\mu\nu}}{\partial x^\gamma}$  and the symmetric tensor  $v_\mu v_\nu$  is zero and find

$$f_\mu^{\text{rad}} = \frac{2q^3}{3mc} \left( \frac{\partial F_{\mu\nu}}{\partial x^\gamma} v^\nu v_\gamma - \frac{q}{m} F_{\mu\gamma} F^{\nu\gamma} v_\nu + \frac{q}{m} F_{\nu\gamma} v^\gamma F^{\nu\delta} v_\delta \right) \quad (1.56)$$

which is the result originally obtained by L. Landau and E.M. Lifshitz [48]. It is worth mentioning that there exist other options than  $v_\mu$  in making the expression Lorentz covariant resulting in alternative theories besides Eq. (1.56). Reviewing them is outside the scope of this thesis but a comprehensive overview can be found in Ref. [55].

To untangle the expression (1.56) one can consider the example in which a charge approaches the speed of light. Then its components containing the third derivatives of the velocity contribute the most so that one can show

$$\mathbf{f}_{\text{rad}} = \frac{2q^4}{3m^2c} (F_{\nu\gamma} u^\gamma F^{\nu\delta} u_\delta) \mathbf{v} \quad (1.57)$$

which is in fact opposite in the direction of  $\mathbf{v}$ . Taking the axis of propagation along  $x$ , Eq. (1.57) can be cast to

$$f_x = -\frac{2q^4}{3m^2c\gamma^2} [(E_y - H_z)^2 + (E_z + H_y)^2] \quad (1.58)$$

which is proportional to the square of its emitted energy.

## 1.5 Quantum regime of radiation reaction

Having treated radiation reaction in the classical and relativistic limits it is appropriate to ask the question on how radiation reaction emerge in a quantum picture? In contrast to previous sections, consider now the charge to be an electron. To quantify the significance of quantum effects, another Lorentz invariant quantity is introduced

$$\chi = \frac{q_e \hbar}{m_e^3 c^4} \sqrt{p^\mu F_{\mu\nu} F^{\mu\nu} p_\nu} = \frac{\gamma_e}{E_{\text{cr}}} \sqrt{\left( \mathbf{E} + \frac{\mathbf{v}}{c} \times \mathbf{B} \right)^2 - \left( \mathbf{E} \cdot \frac{\mathbf{v}}{c} \right)^2} \quad (1.59)$$

where  $p_\mu$ ,  $\mathbf{v}$  and  $\gamma_e$  are the momentum, velocity and Lorentz factor for an electron respectively. This quantity can be seen as the dimensionless acceleration of the electron in its rest frame. This parameter delimits the theory of radiation reaction where  $\chi \gtrsim 1$  signify the presence of quantum effects and  $\chi \ll 1$  implies its classical domain.

In treating the quantum aspect it no longer makes sense to treat the interaction between charges and field as a continuous process since the emission and/or absorption of single photons becomes the dominant feature [56]. Additionally, the probability to generate electron-positron pairs from this scenario becomes non-negligible [37]. A correct description would be to account for every possible interaction channel between the charges, emitted/external photons and pair-generated particles. As noted in the introduction, this is described using QED. Although there are infinite ways to form interaction processes, only those that are non-negligible and relevant for papers A and B are covered. In other words, the significant processes that govern the photon emission and pair-production in laser-electron collisions.

## 1.6 Photon emission and pair-generation

One can envision that when an electron enters a strong laser field, it can absorb some amount of its photons (or any other external photon) and quickly thereafter emit one or many new photons. Classically, this can be seen as the elastic scattering between electrons and photons, also known as Compton scattering [57]. In the framework of QED, interactions like these are depicted using Feynman diagrams and the cross-section of them are computed with their concomitant Feynman rules. In general, the absorption and emission of photons by scattering with an electron is given by the following Feynman diagram in figure 1.3a. Here, time flows to the right in the diagram and one electron absorbs a laser photon  $\gamma_L$  which later on emits a separate photon  $\gamma'$ . Note that the diagram could be extended to include the absorption and emission of multiple photons (non-linear Compton scattering). Additionally, the rate of high-energy photon emissions from non-linear Compton scattering computed from QED is governed by [58, 59]

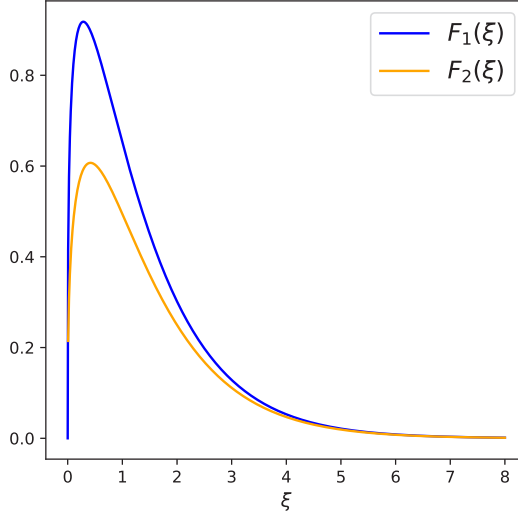


**Figure 1.2:** Illustration of the first (blue solid line) and second (orange solid line) Synchrotron functions.

$$\frac{\partial I}{\partial \omega} = \frac{\sqrt{3}}{2\pi} \frac{q_e^3 E_{cr} \chi}{m_e c^2 \gamma_e} (1 - \delta) \left( F_1(z_c) + \frac{3}{2} \delta \chi z_c F_2(z_c) \right) \quad (1.60)$$

where  $\delta = \frac{\hbar\omega}{m_e c^2 \gamma_e}$  is the energy of the emitted photon with frequency  $\omega$  normalized to the emitting electron energy and  $z_c = \frac{2}{3} \frac{\delta}{(1-\delta)\chi}$ . The functions  $F_1$  and  $F_2$  are known as Synchrotron functions, expressed using modified Bessel functions of the second kind  $K_\nu(\xi)$ :

$$F_1(\xi) = \xi \int_{\xi'}^{\infty} K_{5/3}(\xi') d\xi', \quad F_2(\xi) = \xi K_{2/3}(\xi). \quad (1.61)$$

A graph over the Synchrotron functions given by Eq. (1.61) can be found in Fig. 1.2. Another process that can occur is the collision between two photons which then generate an electron-positron pair. In figure 1.3b the interaction diagram is displayed and could likewise be extended to include many interacting photons (non-linear or multiphoton Breit-Wheeler). While the diagrams are similar in structure, the Breit-Wheeler channel is restricted



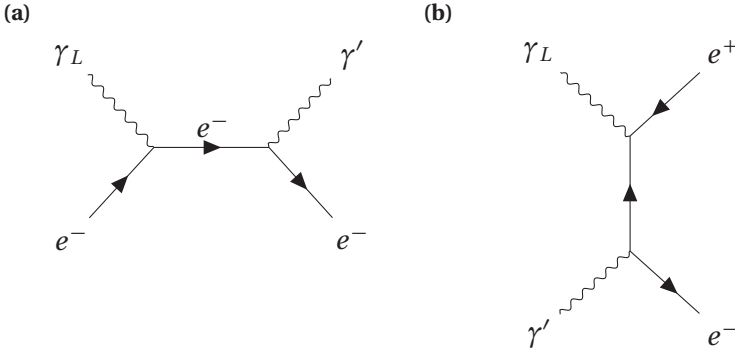


**Figure 1.3:** Tree-level Feynman diagrams for (a) Compton scattering and (b) the Breit-Wheeler process. Solid and curvy lines depict fermions (electrons with  $e^-$  and positrons with  $e^+$ ) and photons ( $\gamma_L$  being laser photons and  $\gamma'$  emitted or external photons) respectively.

in terms of the colliding photon energy. Considering the impact of two photons with four-momenta  $k_\mu = (\mathbf{k}, |\mathbf{k}|)$  and  $k'_\mu = (\mathbf{k}', |\mathbf{k}'|)$ , the pair-production would need to satisfy  $|\mathbf{k}||\mathbf{k}'| > (2m_e c^2)^2$ . In other words, there must be at least enough energy supplied by the photons to overcome the rest energy of the pair. Inclusion of many photons and considering different laser pulse configurations alters this condition in various ways [32, 60].

Just as for Compton scattering, the rate of produced pairs from the Breit-Wheeler process per unit time  $t$  can be shown to be [58]

$$\frac{\partial P}{\partial t} = \frac{\sqrt{3}}{2\pi} \frac{\chi_\gamma q_e^3 E_{\text{cr}}}{\hbar^2 \omega} (\delta_e - 1) \delta_e \left( F_1(z_b) - \frac{3}{2} \chi_\gamma z_b F_2(z_b) \right) \quad (1.62)$$

where now  $z_b = \frac{2}{3} \frac{1}{\chi_\gamma (1 - \delta_e) \delta_e}$ ,  $\delta_e = \frac{m_e c^2 \gamma}{\hbar \omega}$  and

$$\chi_\gamma = \frac{\delta \gamma}{E_{\text{cr}}} \sqrt{\left( \mathbf{E} + \frac{c \mathbf{k}}{\omega} \times \mathbf{B} \right)^2 - \left( \mathbf{E} \cdot \frac{\mathbf{k}}{|\mathbf{k}|} \right)^2} \quad (1.63)$$

is a generalization of  $\chi$  but for photons with momentum  $\mathbf{k}$  and frequency  $\omega$ .

As a final remark, there are at least two more processes on the tree-level apart from those displayed in figure 1.3. One of them is the annihilation of an

electron-positron pair into a single photon and the other is absorption of a single photon by an electron (no emission thereafter). Additionally, there are higher-order processes including multiple interaction vertices which describe related processes. In the scope of QED simulations, the latter can be included in the simulation routine using the diagrams for non-linear Compton scattering and pair-production [37]. As for the two additional tree-level processes, they can be rightfully neglected [32].

## PART II

# ANALYSIS AND RESULTS

## 2 Extraction of SFQED signals and optimal focusing

This chapter is devoted to introduce the theoretical results that constitute paper A. Before outlining its sections, recall from the introduction the advantage in exploiting the collision between high-powered lasers and high-energy electrons. This setting provides a Lorentz boosted field on the order of  $E_{\text{cr}}$  perceived by the electrons and is quantified by the quantum nonlinearity parameter  $\chi$  given by Eq. (1.59). Contemporary laser-beam experiments analyze the post-collision energy spectrum of the electrons and emitted photons, comparing them to that of theoretical predictions made with QED and/or RR models to draw conclusions [42, 43]. Such experiments now operate at values of  $\chi \lesssim 1$  but there are also efforts to probe effects occurring at large values of  $\chi \sim 10^2 - 10^3$  (SFQED) [61–66] of which the conjectured breakdown of QED is of particular interest  $\chi \gtrsim 1600$  [67–72]. Apart from gaining large values of  $\chi$ , the onset of *QED cascades* at these magnitudes pose another difficulty [73] in extracting information from the experiment. Briefly, a QED cascade is the process of generating electron-positron pairs and photons at an exponential rate which is described in Sec. 2.1. This sheer amount of pairs and photons (possessing low  $\chi$ ) can overshadow the sought after deviation in the energy spectrum coming from the limited portion of descriptive electrons/photons (having large  $\chi$ ). To circumvent this, a strategy is developed to retrieve information in such experiments based on the kinematic properties of the electrons and emitted photons found in Sec. 2.1. In addition to this, it is shown how experimentalists can focus their laser optimally for the purpose of achieving the maximal value of  $\chi$ . In Secs. 2.3-2.5 this optimization problem is formulated as follows: "For which focusing geometry can one yield the maximal value of  $\chi$  in the interaction region for a given power  $P$ ?" and solve it. The solution, which is referred to

as a bidipole wave is detailed in Sec. 2.6 in terms of its radiation pattern and how to implement one in practice.

## 2.1 Signal extraction and cascade development

In this section, the specific difficulties mentioned in the premise to this chapter concerning laser-electron collision experiments is presented. To begin with, general experimental obstacles not related to the interaction physics is discussed and then follow the definitions of the properties that are relevant in reading *signals* from such experiments. Additionally, the process of QED cascades and its impact on reading signals is described. In what follows, the term *signal* is defined as measurable quantities in said experiment capable of signaling a deviation compared to past experiments or theoretical models. For instance, the signal can be formed by observing the energy spectrum of electrons and/or photons but could also include the polarization and spin of emitted photons or other theoretical parameters. An example of the latter is the notion of an effective electron and positron mass, introduced later in Ch. 3.

One could argue that future laser-matter facilities will reach very large values of  $\chi$  and thus make a direct detection of SFQED signals. While this statement holds some truth, recall that in the quantum description photons are emitted probabilistically at the rate given by Eq. (1.60). Thus, there is no knowledge at what field strength  $|\mathbf{E}|, |\mathbf{B}|$  (hence  $\chi$ ) and neither at what electron gamma factor  $\gamma_e$  emissions occur. Consequentially, it is not possible to make a direct detection of any signal mapping to values of  $\chi$ . This calls for a statistical approach in which one compares the result of many simulations to that of experiments. For this to be successful, the experiment must be repeatable and robust. Repeatability ensures that one can gather enough data over a reasonable period of time necessary to carry out the statistical analysis and make conclusions. Robustness implies that for each shot, the alignment of the experiment does not vary too much in order to have informative data. To exemplify, if the collision between the laser and the electron beam is not head-on, a substantial fraction of electrons does not experience the strong-field region.

SFQED signals can be carried by electrons having emitted a single *hard* photon around the maximum achievable  $\chi$  of the laser-beam system. Hard photons are defined as those having more than a half of the initial kinetic energy of an electron in the beam ( $> 0.5m_e c^2\gamma_e$ ). A large value of  $\chi$  indicates that the electron has emitted in the vicinity of strong fields and that it has retained its initial kinetic energy (negligible radiative losses prior to entering the strong-field region). The emission of a single hard photon at large  $\chi$  thus becomes a characteristic that separate multiple emissions of lower energy. However, the emitting electrons falling under this category are difficult to distinguish at a detector due to the vast majority of the *background*. Hereinafter, the background is defined as the electrons or photons that do not provide information on SFQED physics i.e. those with low energy or low  $\chi$ . These can stem from (c.f. Fig. 2.1):

- Electrons bypassing the strong-field region which "miss out" on the interaction provides no information at the detector nor does it radiate away photons with substantial energy.
- Electrons emitting a single high-energy photon are indistinguishable from those emitting multiple low-energy photons.
- Electrons that radiate significantly before entering the strong-field zone have lower energy and hence lower values of  $\chi$ . Additionally, this restricts electrons to emit high-energy photons.

Stimulated by this complication, the chain of logic that results in the strategy to obtain a feasible signal at the detector is provided. First, note that electrons conserve their transverse momentum in the interaction with the electromagnetic field of the laser [74]

$$\frac{d}{dt} \left( \mathbf{p}_\perp - \frac{1}{c} \mathbf{A}_\perp \right) = 0 \quad (2.1)$$

where  $\mathbf{p}_\perp$  and  $\mathbf{A}_\perp$  denote the transverse components of the electron momentum and the vector potential of the electromagnetic field respectively. A result of Eq. (2.1) is that at any instance of time, the electron forms an angle  $\alpha$  as measured from its initial axis of propagation:

$$\alpha = \arctan \left( \frac{|\mathbf{p}_\perp|}{|\mathbf{p}_\parallel|} \right) \quad (2.2)$$

where  $\mathbf{p}_{\parallel}$  denote the longitudinal component of the electron momentum. Thus, in the region of strongest field the electron will experience the maximal deviation  $\alpha$  and could potentially be separated from the majority of background cases in which  $\alpha \rightarrow 0$ . Nonetheless, Eq. (2.1) implies that the net gain of transverse momentum is zero meaning that the deviation angle is small when electrons reach the detector. In the end, the signal and background electrons share small values of  $\alpha$  making them difficult to separate regardless. If instead the emitted photons from these electrons are considered there are multiple advantages at hand. First, photons emitted in the strong-field region also have large values of  $\alpha$  but they retain this value since they do not obey Eq. (2.1). Second, in the limit of high  $\chi$  the average distance before re-combining into a pair is  $\ell_{pp} \approx 3\ell_{rad}$  where  $\ell_{rad}$  is the mean-free path between photon emissions [75]

$$\ell_{rad} \approx 15\lambda_C \gamma_e^{1/3} (a_0/a_{cr})^{-2/3} \quad (2.3)$$

where  $\lambda_C = \frac{h}{m_e c}$  is the Compton wavelength,  $a_0 = \frac{e|\mathbf{E}|}{m_e \omega c}$  is the dimensionless amplitude of the laser electric field  $|\mathbf{E}|$  and  $a_{cr}$  is the critical field  $E_{cr}$  in the same dimensionless units. In other words, these photons have a greater chance to escape the strong-field region and contribute to the signal whereas electrons would be more likely to emit multiple times, contributing to the background. Note that electrons emitting hard photons are less likely to have emitted before this. Conclusively, it is anticipated that a large portion of these photons, having large  $\alpha$  and high energy  $\hbar\omega$  to constitute a feasible signal.

When the laser is linearly polarized there is a chance that photons can be emitted with high energy and high  $\chi$  when  $\alpha = 0$  (see Fig. 2.1) which is due to the phase dependence within the laser field. If the polarization is circular the unfavorable phase dependence is eliminated, making  $\alpha$  and  $\chi$  correlated [72]. The benefit is then that large values of  $\alpha$  implies large values of  $\chi$ .

Large values of  $\chi$  increase the risk of generating a vast blend of electron-positron pairs and photons, commonly referred to as a QED cascade. This avalanche of particles and photons can mask the few electrons or photons that carries information about the interaction in the strong-field regime. In what follows, the difficulties that arise with QED cascades are described.

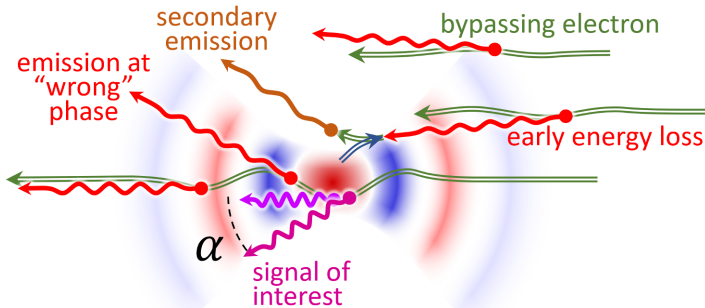


**Figure 2.1:** Concept illustrating various paths and emissions electrons can undergo in the collision with a tightly focused laser pulse. Adapted from [72].

From section 1.6 the processes of photon emission and pair-production were discussed. One may have realized that under appropriate conditions, a single electron could trigger an avalanche of electron-positron pairs. To see this, consider a single electron emitting a high-energy photon in the presence of a high-intensity laser field. This photon can combine with other laser photons through the Breit-Wheeler process (see Fig. 1.3b), generating a pair. Both the electron and the positron have the opportunity to emit high-energy photons which in turn can combine with the laser photons, forming more pairs. This results in an avalanche of particles conceptualized in Fig. 2.2. The formation of the cascade is exponential in time [73, 76] and the formation length can be quantified by Eq. (2.3). For an electron with energy 2 GeV [77] and  $\chi \sim 1$  the average distance between photon emissions according to Eq. (2.3) is on the order of a few nm. Comparing this to a typical laser pulse with a duration of 15fs (spatial extent on the order of tens of  $\mu\text{m}$ ) the electron is very likely to trigger a cascade. Returning to the discussion on signal extraction in experiments it is clear that QED cascades constitute an extensive background of low energy and low  $\chi$  photons and pairs that conceal the signal.

To conclude, the proposal is to make statistical inferences by measuring distributions of (1) emitted photons (as opposed to initial electrons) which, (2) are restricted to have sufficiently large deviation angles and (3) energies, in contrast to previous experimental endeavours.

Based on the analysis of this section, it is expected that such data is formed by a larger fraction of photons originating from the strong-field QED processes

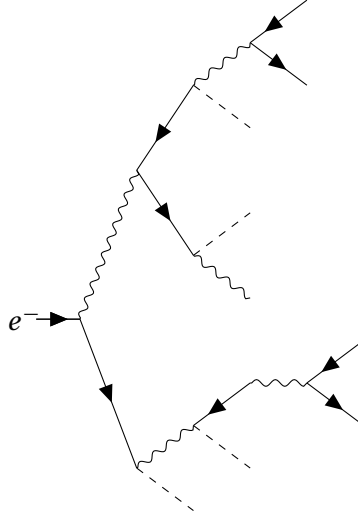


**Figure 2.2:** Depiction of a seed electron emitting a photon(s) which eventually results in a cascade of electron-positron pairs and photons. Dashed lines indicate the continued trajectory of the emitting fermion. Here it is understood that photons collide with background photons to form pairs.

at high  $\chi$ . As such, this provides a more prominent signal to reach any given confidence level whether it be hypothesis testing or parameter estimation.

## 2.2 Optimal focusing

So far, a strategy to extract signals of SFQED by selecting photons at high values of  $\chi$  from laser-electron collisions has been developed. The next intent is to assess how one can reach the maximum value of  $\chi$  in such experiments for a given laser power  $P$ . To elucidate this matter, consider a single focused laser beam of peak power  $P$  with peak electric field  $E^{(1)}$ . If the power is split into two separate beams which are summed coherently at focus in e.g. a counter-propagating scheme, the resulting peak electric field becomes

$$E^{(2)} = \frac{E^{(1)}}{\sqrt{2}} + \frac{E^{(1)}}{\sqrt{2}} = \sqrt{2}E^{(1)} \quad (2.4)$$

which increase the original peak electric field by a factor of  $\sqrt{2}$ . This result can be generalized by splitting the original beam into  $N$  separate ones in



one plane such that

$$E^{(N)} = \sqrt{N} E^{(1)} \quad (2.5)$$

where  $E^{(N)}$  denote the peak electric field achieved by coherently adding  $N$  beams at focus. Logically, it is possible to add even more beams at an angle to this plane given that the  $N$  beams must not overlap on their way to the focus. This concept is known as multiple colliding laser pulses (MCLP) and was formulated in Ref. [78]. The theoretical limit for the peak electric field for a power  $P$  is given by the dipole wave solution [79, 80] which will be covered shortly.

The concept above concerns reaching the strongest electric field at focus for a power  $P$  which is appealing in reaching the critical field  $E_{cr}$ . However, the aim is to maximize the value of  $\chi$  since the scheme involve electron beams. Certainly, maximizing the electric field strength is beneficial for high  $\chi$  but Eq. (1.59) also suggest that the magnetic field can contribute. Therefore, one considers the problem of finding the focusing geometry that maximize the value of  $\chi$  for a given electron under the assumption of straightforward propagation, which is practically warranted by its high energy.

In what follows, the dipole wave solution is elaborated on in Secs. 2.3-2.4 firstly, using the approach of I.M. Bassett whom in 1986 demonstrated that the dipole component provides the highest possible electromagnetic energy density for a given  $P$ . Then, in Sec. 2.5 the optimization problem for maximizing of  $\chi$  is defined and solved. Lastly, the structure of the solution and its practical implementation is detailed in Sec. 2.6.

## 2.3 Optimal focusing : field strength

In this section, the following optimization problem: "What focusing geometry yields the largest electromagnetic energy density at focus, hence the strongest peak field for a given power  $P$ ?" is solved. The derivation of I. M. Basset is adapted [79] where the author express the Maxwell equations using the multipole representation. Then, by stating that this optimum is achieved at the origin in this representation the analysis is simplified to a few electromagnetic field components and the solution can be obtained. This result

will act as a stepping stone in attaining the optimal focusing geometry for reaching the highest value for  $\chi$ .

The Maxwell equations in the absence of external charges and current densities in Cartesian coordinates  $x, y$  and  $z$  read [81]

$$\nabla \cdot \mathbf{E} = 0, \quad (2.6)$$

$$\nabla \times \mathbf{E} = -\frac{1}{c} \frac{\partial \mathbf{B}}{\partial t}, \quad (2.7)$$

$$\nabla \cdot \mathbf{B} = 0, \quad (2.8)$$

$$\nabla \times \mathbf{B} = \frac{1}{c} \frac{\partial \mathbf{E}}{\partial t}. \quad (2.9)$$

The multipole representation is found by switching to spherical coordinates  $x, y, z \rightarrow r, \theta, \phi$ . Any real solution of Eqs. (2.6)-(2.9) can be expressed as the real part of some complex electric and magnetic multipole fields multiplied by  $e^{-i\omega t}$  where  $\omega$  is its the central frequency. These multipole components can be written [82]

$$E_r^E = \ell(\ell + 1) \frac{j_\ell(kr)}{r} Y_\ell^m(\theta, \phi), \quad (2.10)$$

$$E_\theta^E = \frac{1}{r} \frac{\partial}{\partial r} (r j_\ell(kr)) \frac{\partial}{\partial \theta} Y_\ell^m(\theta, \phi), \quad (2.11)$$

$$E_\phi^E = \frac{im}{r \sin \theta} \frac{\partial}{\partial r} (r j_\ell(kr)) Y_\ell^m(\theta, \phi), \quad (2.12)$$

$$B_r^E = 0, \quad (2.13)$$

$$B_\theta^E = \frac{km}{\sin \theta} j_\ell(kr) Y_\ell^m(\theta, \phi), \quad (2.14)$$

$$B_\phi^E = ik j_\ell(kr) \frac{\partial}{\partial \theta} Y_\ell^m(\theta, \phi) \quad (2.15)$$

where  $\ell = 1, 2, 3, \dots$ ,  $m = -\ell, -\ell + 1, \dots, \ell$ ,  $k = \omega/c$  and  $j_\ell, Y_\ell^m(\theta, \phi)$  are spherical Bessel functions and spherical harmonics respectively. Subscripts indicate the vector components of the fields in the spherical coordinates

$$\hat{\mathbf{r}} = \hat{\mathbf{x}} \sin \theta \cos \phi + \hat{\mathbf{y}} \sin \theta \sin \phi + \hat{\mathbf{z}} \cos \theta, \quad (2.16)$$

$$\hat{\theta} = \hat{\mathbf{x}} \cos \theta \cos \phi + \hat{\mathbf{y}} \cos \theta \sin \phi - \hat{\mathbf{z}} \sin \theta, \quad (2.17)$$

$$\hat{\phi} = -\hat{\mathbf{x}} \sin \phi + \hat{\mathbf{y}} \cos \phi \quad (2.18)$$

where  $\hat{\mathbf{x}}, \hat{\mathbf{y}}$  and  $\hat{\mathbf{z}}$  denote the Cartesian unit vectors. The relation between electric multipole and magnetic multipole fields satisfy the following rule:

$$\mathbf{E}^B = -\mathbf{B}^E, \quad (2.19)$$

$$\mathbf{B}^B = \mathbf{E}^E \quad (2.20)$$

where superscripts  $E, B$  denote electric and magnetic multipole fields. To be clear, the magnetic components of an electric multipole field will vanish at the origin and vice versa for the magnetic multipole field. Nevertheless, with the components given by Eqs. (2.10)-(2.15) one is in a position to answer the following: "Which multipole component will provide the maximal energy density  $U$  and hence the peak electric or magnetic field?". If the optimum is taken to be attained at the origin, i.e.  $r \rightarrow 0$ , an expansion of the spherical Bessel functions for small arguments  $x$  can be employed

$$j_\ell(x) \approx \frac{x^\ell}{(2\ell + 1)!!} \left( 1 - \frac{x^2}{2(2\ell + 3)} + \dots \right) \quad (2.21)$$

where the double factorial is defined as  $n!! = n \cdot (n-2) \cdot (n-4) \cdot \dots \cdot 5 \cdot 3 \cdot 1$ . Taking the limit of Eqs. (2.10)-(2.15) and making use of (2.21) only the multipole modes with  $\ell = 1$  i.e. the dipole terms contribute. Without loss of generality one can consider an electric dipole of which six components remain:

$$\mathbf{E}_{1,-1}^E = \mathbf{B}_{1,-1}^B = k(6\pi)^{-1/2} (\hat{\mathbf{x}} - i\hat{\mathbf{y}}), \quad (2.22)$$

$$\mathbf{E}_{1,0}^E = \mathbf{B}_{1,0}^B = k(3\pi)^{-1/2} \hat{\mathbf{z}}, \quad (2.23)$$

$$\mathbf{E}_{1,1}^E = \mathbf{B}_{1,1}^B = -k(6\pi)^{-1/2} (\hat{\mathbf{x}} + i\hat{\mathbf{y}}) \quad (2.24)$$

where subscripts indicate values of  $\ell$  and  $m$ . Evidently, any of the electric field components (2.22)-(2.24) will provide the optimum. One can show that the peak dimensionless amplitude  $a_0^d$  of such a field becomes

$$a_0^d \approx 780(P/(1 \text{ PW}))^{1/2}. \quad (2.25)$$

The same holds for the peak magnetic field of magnetic dipole waves. Applications of dipole waves range from particle trapping [83], photon generation [84–86] and the generation of extreme electron-positron plasma states [87, 88]. Note that all solutions under the multipole analysis have been considered monochromatic i.e. with an infinite temporal extent. This can be generalized to pulsed solutions with arbitrary temporal envelopes (see Ref. [89]).

The mathematical expressions alone are not necessarily enough to identify the structure of such waves. However, dipole waves can be regarded as the time reversed process of an antenna emitting dipole radiation. Fig. 2.3a and 2.3b provide a cross sectional view of two dipole waves with perpendicular symmetry axes as well as a bidipole wave which will be defined shortly.

## 2.4 Additive property of multipoles

An important result following from the previous analysis is that both the electromagnetic energy density and the incoming power are additive. Put differently, the total of either quantity is the sum of the individual quantity from each multipole. That is, any cross terms vanish.

Without loss of generality one can analyze the superposition of two multipole fields where one of them is defined by a set of  $\ell, m$  and the other by  $\ell', m'$ . The energy density for a specific mode is given by

$$u_{\ell,m} = \frac{1}{4\pi} (|\mathbf{E}_{\ell,m}|^2 + c^2|\mathbf{B}_{\ell,m}|^2) \quad (2.26)$$

where the superscripts  $E, B$  have been dropped and it is explicitly stated which type of multipole field is concerned from now on. Then, the resulting energy density from the sum of two multipoles is

$$\frac{1}{4\pi} (|\mathbf{E}_{\ell,m} + \mathbf{E}_{\ell',m'}|^2 + c^2|\mathbf{B}_{\ell,m} + \mathbf{B}_{\ell',m'}|^2) \quad (2.27)$$

which is equivalent to

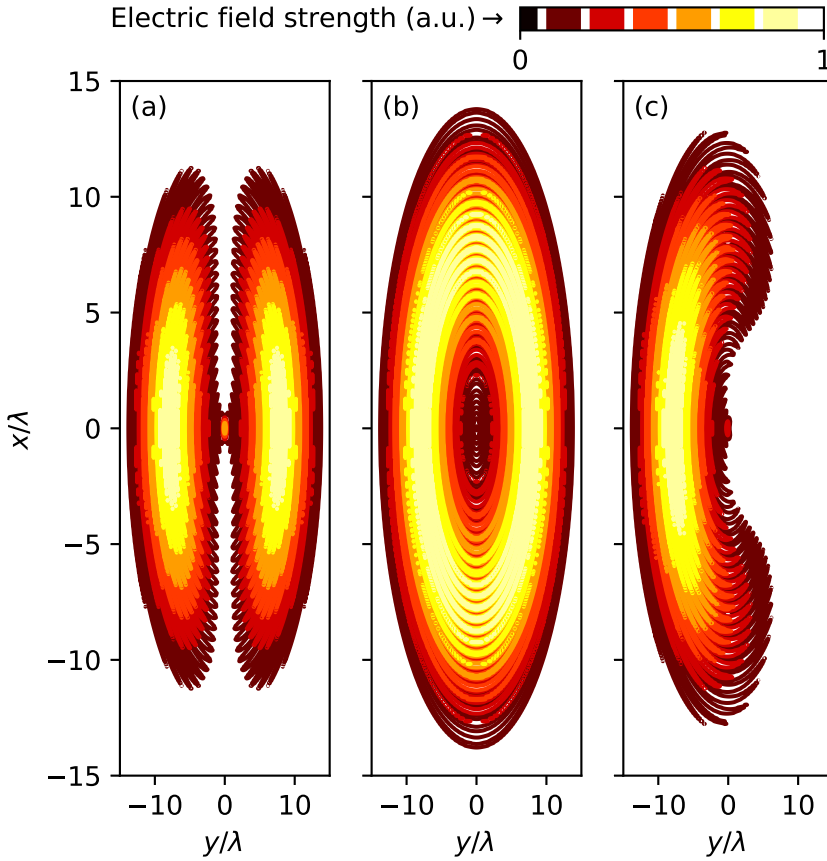


**Figure 2.3:** Cross section of the electric field strength in the plane  $xy$ -plane where  $z = 0$  for (a) an electric dipole pulse, (b) a magnetic dipole pulse and (c) a bidipole pulse. In all cases the wavelength was  $\lambda = 0.8 \mu\text{m}$  and the duration  $\tau = 5\lambda/c$ . The pulses are displayed at a time  $t = 9\lambda/c$  before reaching focus.

$$u_{\ell,m} + u_{\ell',m'} + \frac{1}{2\pi} (\mathbf{E}_{\ell,m} \cdot \mathbf{E}_{\ell',m'} + c^2 \mathbf{B}_{\ell,m} \cdot \mathbf{B}_{\ell',m'}). \quad (2.28)$$

In order to prove the additive property for this quantity it is enough to show that the cross term in Eq. (2.28) vanishes. Recall that at the origin, the electric (magnetic) field will vanish for magnetic (electric) multipole waves. Thus,

the cross term is zero for waves of different type. In the case of identical types but for arbitrary  $\ell, \ell'$  and  $m, m'$  one can be reminded that only the dipole terms contribute at the origin. Hence, the proof is completed by verifying the orthogonality between the expressions given in Eqs. (2.22)-(2.24). An analogous procedure can be done for the magnetic dipole waves.

To sketch the proof of the additive property for power, the Poynting vector for a sum of two multipole waves can be expressed as

$$\begin{aligned} \mathbf{S}_{\text{tot}} &\propto (\mathbf{E}_{\ell,m} + \mathbf{E}_{\ell',m'}) \times (\mathbf{B}_{\ell,m} + \mathbf{B}_{\ell',m'}) \\ &\propto \mathbf{S}_{\ell,m} + \mathbf{S}_{\ell',m'} + (\mathbf{E}_{\ell,m} \times \mathbf{B}_{\ell',m'}) + (\mathbf{E}_{\ell',m'} \times \mathbf{B}_{\ell,m}) \end{aligned} \quad (2.29)$$

where  $\mathbf{S}_{\ell,m}$  and  $\mathbf{S}_{\ell',m'}$  denote the Poynting vector for each multipole. Recall from Sec. 1.1 that

$$|\mathbf{S}_{\text{tot}}| = \frac{dP_{\text{tot}}}{R^2 d\Omega} \quad (2.30)$$

where  $R$  is now the radius of an arbitrary sphere and  $d\Omega$  a solid angle element in this coordinate system respectively. To facilitate the analysis, consider the power crossing the sphere by projecting  $\mathbf{S}_{\text{tot}}$  along  $\hat{r} = \frac{\mathbf{R}}{R}$  so that Eq. (2.30) can be reformulated as

$$P_{\text{tot}}^C \propto P_{\ell,m}^C + P_{\ell',m'}^C + R^2 \int (\mathbf{E}_{\ell,m} \times \mathbf{B}_{\ell',m'}) \cdot \hat{r} + (\mathbf{E}_{\ell',m'} \times \mathbf{B}_{\ell,m}) \cdot \hat{r} d\Omega \quad (2.31)$$

where the superscript denote the power crossing the surface of the sphere and subscripts have the same meaning as previously. Proving that the cross-terms in Eq. (2.31) are zero requires an extensive calculation which is omitted here. The full proof can be found at p.285 of Ref. [79] where the idea is to exploit the orthogonal properties between spherical harmonics when substituting in arbitrary multipole fields given by Eqs. (2.10)-(2.15).

## 2.5 Optimal focusing : maximization of $\chi$

It might be natural to think that the solution given by Eqs. (2.22)-(2.24) could provide the largest value of  $\chi$  because it provides the strongest peak electric

field. However, the expression for  $\chi$  suggests that both  $\mathbf{E}$  and  $\mathbf{B}$  can contribute. So the question arise if there exist a better choice for the focusing geometry than the dipole wave in this context?

To arrive at the solution one can continue the discussion from Sec. 2.3 with the exception that both electric and magnetic field contributions exist at the origin. Again, only dipole modes exist here so the solution must be a combination of them. Whatever the solution, one can take its electric field to point in the  $\hat{\mathbf{z}}$ - direction so that its electric field component comprise of Eq. (2.23):

$$\mathbf{E}_{\text{sol}} = \mathbf{E}_{1,0}^E. \quad (2.32)$$

Choosing its magnetic field to be oriented in the  $xz$ -plane, one observes that this must be a combination of Eqs. (2.22)-(2.24)

$$\mathbf{B}_{\text{sol}} = \underbrace{\mathbf{B}_{1,0}^B}_{\propto \hat{\mathbf{z}}} + \sqrt{2} \underbrace{(\mathbf{B}_{1,-1}^B - \mathbf{B}_{1,1}^B)}_{\propto \hat{\mathbf{x}}} \quad (2.33)$$

where the factor of  $\sqrt{2}$  ensure synchronous peaking. The solution can be divided into three parts due to the additive property outlined in Sec. 2.4. That is, for a given power  $P$  a portion  $aP$  goes into the electric dipole wave in Eq. (2.32) and portions  $bP$  and  $(1-a-b)P$  go to the magnetic dipole waves in Eq. (2.33) respectively. It is understood that  $0 \leq ab \leq 1$  and  $a+b \leq 1$ . From this the solution can be expressed as

$$\mathbf{E}_{\text{sol}} \propto \sqrt{a} \hat{\mathbf{z}}, \quad (2.34)$$

$$\mathbf{B}_{\text{sol}} \propto \sqrt{b} \hat{\mathbf{z}} + \sqrt{1-a-b} \hat{\mathbf{x}}. \quad (2.35)$$

So far the discussion has only involved electromagnetic fields. Accounting for the propagation of electrons, note that the value of  $\chi$  is maximal if electrons travel along  $\hat{\mathbf{y}}$  since then  $\mathbf{v} \cdot \mathbf{E}_{\text{sol}} = 0$ . Putting the expressions (2.34) and (2.35) into (1.59) one obtains

$$\chi \propto \sqrt{\left( (\sqrt{a} + \sqrt{1-a-b})^2 + b \right)}. \quad (2.36)$$

To find the optimum, the derivative of  $\chi^2$  with respect to  $b$  is taken

$$\frac{\partial \chi^2}{\partial b} \propto -\sqrt{\frac{a}{1-a-b}} \leq 0. \quad (2.37)$$

Hence,  $b = 0$  must give the maximum. Next, evaluating  $\frac{\partial \chi^2}{\partial a}$  at  $b = 0$  yields

$$\frac{\partial \chi^2}{\partial a} \propto \frac{1-2a}{\sqrt{a(1-a)}} \quad (2.38)$$

with extremum at  $a = 1/2$ . As a result, the solution according to Eqs. (2.34) and (2.35) comprise out of one electric dipole wave and one magnetic dipole wave with perpendicular orientations (c.f. Figs. 2.3a and 2.3b). This solution achieves the maximal value of  $\chi$  for a given power  $P$  and is referred to as a bidipole wave in paper A [72]

$$\chi_{\max} = \kappa \left( \frac{\varepsilon}{1 \text{ GeV}} \right) \left( \frac{P}{1 \text{ PW}} \right)^{1/2} \left( \frac{\lambda}{1 \mu\text{m}} \right)^{-1} \quad (2.39)$$

where  $\lambda$  is the bidipole wavelength,  $\varepsilon$  is the initial energy of the electron and  $\kappa \approx 5.25$ . Contours of the bidipole electric field strength in the  $x y$ -plane can be seen in Fig. 2.3c. As a matter of fact, the study of mixed dipole waves has been covered in Ref. [90]. Nonetheless, the realization that this specific mixed dipole wave gives the maximum value of  $\chi$  introduces novelty.

## 2.6 Structure of the bidipole wave

This section is allocated to derive the intensity dependence of the bidipole wave to build further insight in addition to Fig. 2.3c. Further, it is demonstrated how the bidipole wave can be constructed by reflecting a *suitable* laser beam off a parabolic mirror. By suitable, the spatial dependency of the polarization and the intensity across the beam before reflection needs to be specified in achieving the bidipole structure which is computed next.

In the far-field region  $r \rightarrow \infty$  the electric field of the bidipole wave, now denoted as  $\mathbf{E}_{\text{bd}}$ , scales as

$$\mathbf{E}_{\text{bd}} \propto \frac{\mathbf{E}_{1,0}^E + \mathbf{E}_{1,0}^B}{r} \quad (2.40)$$

where



$$\mathbf{E}_{1,0}^E \propto (\hat{\mathbf{z}} \times \hat{\mathbf{n}}) \times \hat{\mathbf{n}}, \quad (2.41)$$

$$\mathbf{E}_{1,0}^B \propto (\hat{\mathbf{x}} \times \hat{\mathbf{n}}) \quad (2.42)$$

and  $\hat{\mathbf{n}} = \hat{\mathbf{r}}$ . Directions are chosen so that the electron propagates along  $\hat{\mathbf{y}}$ . Here the unit vector  $\hat{\mathbf{n}}$  is written as  $\hat{\mathbf{n}} = (n_x, n_y, n_z)$  where its components are given by

$$\begin{aligned} n_z &= \cos \theta, \\ n_x &= \sin \theta \cos \varphi, \\ n_y &= \sin \theta \sin \varphi. \end{aligned}$$

Now, let us compute the intensity dependence of such a wave by rewriting Eqs. (2.41) and (2.42)

$$\mathbf{E}_{1,0}^E \propto n_x n_z \hat{\mathbf{x}} - (n_x^2 + n_y^2) \hat{\mathbf{z}} + n_y n_z \hat{\mathbf{y}}, \quad (2.43)$$

$$\mathbf{E}_{1,0}^B \propto n_y \hat{\mathbf{z}} - n_z \hat{\mathbf{y}} \quad (2.44)$$

so that

$$I(r, \theta, \varphi) \propto |\mathbf{E}_{1,0}^E + \mathbf{E}_{1,0}^B|^2 = n_x^2 n_z^2 + (n_x^2 + n_y^2 - n_y)^2 + n_z^2 (n_y - 1)^2. \quad (2.45)$$

In fact, the intensity is independent of  $\varphi$  by noting

$$\frac{\partial n_z}{\partial \varphi} = 0, \quad \frac{\partial n_x}{\partial \varphi} = -n_y, \quad \frac{\partial n_y}{\partial \varphi} = n_x.$$

Using this fact and taking the derivative of Eq. (2.45) with respect to  $\varphi$  yields

$$\frac{\partial I}{\partial \varphi} \propto 2n_x n_y (1 - n_x^2 - n_y^2 - n_z^2) = 0 \quad (2.46)$$

which proves the independence of  $\varphi$ . Arbitrarily,  $\varphi = 0$  can then be chosen so that  $\sin \varphi = 0$  and  $\cos \varphi = 1$  and one can re-express Eq. (2.45) as

$$I \propto (1 - \cos \theta)^2 / r^2. \quad (2.47)$$

Having derived the intensity scaling for the bidipole wave it is possible to state the following. First, the radiation pattern has a  $(1 - \cos \theta)^2$  dependence meaning that radiation arrives predominantly from one side. Secondly, this scaling is rotationally invariant around the  $\hat{\mathbf{y}}$ -axis because of the  $\varphi$  independence. Putting this together one can better understand the cross section of the bidipole wave as seen in Fig. 2.3c.

Next, the generation of a bidipole wave in practice is shown. Despite its mathematical solution being a sum of two dipole waves, the practical implementation only requires a single laser beam being reflected off a parabolic mirror. Additionally, this probe beam need to have 1) linear polarization everywhere and 2) a bell-shaped intensity distribution prior to reflection. To prove the former, consider the electric field of the probe pulse before reflection  $\mathbf{E}_p$  which can be written

$$\mathbf{E}_p = \mathbf{E} - 2(\mathbf{E} \cdot \mathbf{N})\mathbf{N} \quad (2.48)$$

to within a constant factor. Here,  $\mathbf{N} = (\hat{\mathbf{y}} - \hat{\mathbf{n}})/|\hat{\mathbf{y}} - \hat{\mathbf{n}}|$  is the mirror normal. observing that  $\mathbf{E} \cdot \mathbf{N} = n_z(n_y - 1)/|\hat{\mathbf{y}} - \hat{\mathbf{n}}|$  and evaluating the  $x$  component of  $\mathbf{E}_p$  one finds

$$\mathbf{E}_p \cdot \hat{\mathbf{x}} = n_x n_z + 2n_z(n_y - 1)n_x \left( n_x^2 + n_z^2 + (n_y - 1)^2 \right)^{-1} = 0 \quad (2.49)$$

implying that the probe need to have linear polarization along  $\hat{\mathbf{z}}$  everywhere. The intensity of the probe before reflection  $I_p$  can be derived by employing Eq. (2.47) and the expression for  $\mathbf{N}$ . The result is

$$I_p \propto \left( 1 + \left( \frac{R}{2L} \right)^2 \right)^{-4} \quad (2.50)$$

where  $R$  is now the transverse distance to the  $\hat{\mathbf{z}}$ -axis (not to be confused with the radius of the sphere from the previous section.) and  $L$  is the distance to the parabolic mirror. Indeed, the intensity distribution given by Eq. (2.50) is bell-shaped.

Both the discussion of signal extraction in Sec. 2.1 and the bidipole solution constitute the core of paper A. While the discussion has been thorough, any

results or limitations of these topics is postponed to the introductory text of paper A provided in Sec. 4.1.

### 3 Bayesian approach to radiation reaction

It has been clear from the previous chapter that experimentally probing QED in the limit of high  $\chi$  is not straightforward due to the vast portion of low  $\chi$  background stemming from QED cascades and low-energy emissions. The situation is worsened if the goal is to study nonperturbative QED effects by measuring *early* signals from this regime. By early one refers to the capabilities of contemporary and future experiments in measuring minor deviations attributed to the conjectured breakdown of QED at  $\chi \sim 1600$  already at values  $\chi \sim 10 - 100$ . A statistical approach might then be crucial. For instance, one could embed such effects within a parameterized model and compare the results of simulations and experiments to infer the values of the model parameters.

This chapter conveys the versatility of Bayesian techniques in experiments to benchmark models linked to nonperturbative effects which is the essence of paper B. In Sec. 3.1 the concepts of *model*, *experiment* and *data* are defined and embedded in the Bayesian framework. Importantly, circumstances when the *likelihood* becomes intractable is discussed, calling for methods that mitigate this difficulty. The idea to overcome it is presented in Sec. 3.2 by considering the *standard rejection sampling algorithm* and its connection to the Bayesian scheme. Further, it is demonstrated how simulation data through the model can mitigate an uncomputable likelihood but instead poses a deficiency related to the dimensionality of the data. The remedy for this issue is given in Sec. 3.3 by means of dimensionality reduction from *summary statistics* and *kernel functions*, culminating in the formulation of the ABC algorithm. In Sec. 3.4 the difficulties of latent variables are exemplified in applying ABC sampling to a model which represent the idea of a mass shift. In Sec. 3.5 the problem of latent variables is solved by assessing the measured data and choice of summary statistics.

#### 3.1 Bayesian inference

Suppose one has a model  $\mathcal{M}(\vartheta)$  dependent on a parameter  $\vartheta$  (which can be a vector) which one seek to infer by observing data  $\mathcal{D}_{\text{obs}}$ . One approach would be to assign a set of probabilities on the data  $\mathcal{D}_{\text{obs}}$  by performing e.g.

hypothesis testing, forming confidence intervals and so on. If additional data  $\mathcal{D}'_{\text{obs}}$ , complementary to  $\mathcal{D}_{\text{obs}}$  appear it is not obvious how to incorporate this new knowledge to improve the current result. For instance, an experiment  $\mathcal{E}$  might produce many sets of newly observed data. For each, the ambition is to improve the previous result of the inference. This scenario is suitable for a Bayesian approach which incorporates prior knowledge to update results.

In Bayesian statistics, information regarding the model parameters are encapsulated by a posterior probability distribution  $\pi(\vartheta|\mathcal{D}_{\text{obs}})$ . This is formulated via Bayes' theorem [91]

$$\pi(\vartheta|\mathcal{D}_{\text{obs}}) = \frac{\mathcal{L}(\mathcal{D}_{\text{obs}}|\vartheta) \cdot \pi(\vartheta)}{\pi(\mathcal{D}_{\text{obs}})} \quad (3.1)$$

where  $\mathcal{L}(\mathcal{D}_{\text{obs}}|\vartheta)$  is the likelihood, expressing the probability to observe the data  $\mathcal{D}_{\text{obs}}$  given  $\vartheta$ . Further,  $\pi(\vartheta)$  is the prior distribution, reflecting any knowledge on  $\vartheta$  prior to the analysis. Lastly,  $\pi(\mathcal{D}_{\text{obs}})$  is known as the evidence and acts as the normalizing factor. Here, selecting the best set of parameters is not a binary outcome as in hypothesis testing. The inference is done by computing an estimate  $\hat{\vartheta}$  from  $\pi(\vartheta|\mathcal{D}_{\text{obs}})$  e.g. the mode of this density or the location of its mean. To assess the significance of the estimate, credible intervals can be formed using the posterior (not to be confused with confidence intervals). These can be defined in the following way

$$\int_{\vartheta_{\min}}^{\vartheta_{\max}} \pi(\vartheta|\mathcal{D}_{\text{obs}}) d\vartheta = 1 - \beta \quad (3.2)$$

where  $0 \leq \beta \leq 1$  sets the probability to observe  $\vartheta_{\min} < \vartheta < \vartheta_{\max}$  given the data  $\mathcal{D}_{\text{obs}}$ .

Obtaining the posterior can be done in various ways. In rare cases, a closed form can be found using conjugate priors [92]. If the likelihood is in closed form or if one can motivate a suitable one the choice of a prior distribution belonging to the same probability distribution family makes also the posterior analytically tractable. As an example, if  $\mathcal{L}(\mathcal{D}_{\text{obs}}|\vartheta) \sim \mathcal{N}(\mu_{\text{obs}}, \sigma^2)$  where  $\mathcal{N}$  denote the normal distribution with known mean  $\mu_{\text{obs}}$  and unknown variance  $\sigma^2$  the choice of  $\pi(\vartheta) \sim \mathcal{IG}(\alpha_{\text{IG}}, \beta_{\text{IG}})$  ensures a closed form of the

posterior. Here,  $\mathcal{G}(\alpha_{\text{IG}}, \beta_{\text{IG}})$  denote the inverse gamma distribution with hyperparameters  $\alpha_{\text{IG}}$  and  $\beta_{\text{IG}}$ .

Many times, no closed form exist for the posterior. Instead, it can be approximated by collecting a finite amount of samples from it using numerical routines. Common methods include importance sampling, Markov chain Monte Carlo (MCMC) and sequential Monte Carlo (SMC) [93–95]. All Monte Carlo methods require evaluation of the likelihood at some point, which becomes difficult when the likelihood is computationally expensive or simply not possible. An example of the former can arise when  $\mathcal{D}_{\text{obs}}$  is of large dimensionality, making the evaluation of  $\mathcal{L}$  demanding. In the latter case, the likelihood might be defined implicitly as a data generating process such that  $\mathcal{D}_{\text{sim}} \sim \mathcal{M}(\vartheta)$ . This chapter will be focusing on the latter, when the model is defined in a way only accessible through simulations with input parameter  $\vartheta$ . Finally, the data will be considered *discrete* in the following discussion but will later be relaxed to continuous data. By discrete it is implied that the data entries are integers.

## 3.2 Likelihood mitigation

To resolve the issue of likelihood incomputability an alternative approach to sample the posterior becomes central. Such methods exist and this section adopts a similar motivation made in Ref. [96].

Consider the problem of sampling a target distribution  $T(\vartheta)$  provided an auxiliary sampling density  $A(\vartheta)$  with  $A(\vartheta) > 0$  if  $T(\vartheta) > 0$ . Standard rejection sampling can then be used:

---

### **Algorithm 1** : Standard rejection sampling algorithm

---

- 1: Acquire a sample  $\vartheta^*$  from the auxiliary density :  $\vartheta^* \sim A(\vartheta)$ .
  - 2: Admit the sample with probability  $\frac{T(\vartheta^*)}{KA(\vartheta^*)}$  where  $K \geq \text{argmax} \left[ \frac{T(\vartheta)}{A(\vartheta)} \right]$ .
  - 3: Discard  $\vartheta^*$  if it was not admitted : Repeat steps (1)-(2) as many times necessary.
- 

In the end, the result is a collection of samples from  $T(\vartheta)$ . The connection

to Bayesian inference is made by assigning  $T(\vartheta) = \pi(\vartheta|\mathcal{D}_{\text{obs}})$  and  $A(\vartheta) = \pi(\vartheta)$ . By comparing Eq. (3.1) with step 2 of Alg. 1 it is evident that such a choice makes the acceptance probability proportional to the likelihood, which is intractable by the premise. Nonetheless, the opportunity to generate data  $\mathcal{D}_{\text{sim}} \sim \mathcal{M}(\vartheta)$  from the model turns out to be essential in evading direct computation of the likelihood. Because, if the model were to produce data for some  $\vartheta^*$  that coincide with data from that of the experiment  $\mathcal{D}_{\text{obs}} = \mathcal{D}_{\text{sim}}$  then the probability for this is exactly  $\mathcal{L}(\mathcal{D}_{\text{obs}}|\vartheta^*)$ . Thus, the acceptance probability in Alg. 1 could be replaced by the requirement of a perfect match between data. Implementing the aforementioned changes allows one to express *likelihood-free* sampling:

---

**Algorithm 2** : Likelihood-free rejection sampling

---

- 1: Sample a proposal  $\vartheta^* \sim \pi(\vartheta)$ .
  - 2: Generate data  $\mathcal{D}_{\text{sim}} \sim \mathcal{M}(\vartheta^*)$  from the model.
  - 3: If  $\mathcal{D}_{\text{sim}} = \mathcal{D}_{\text{obs}}$  the proposal is admitted, if not it is discarded.
  - 4: Repeat (1)-(3) as many time necessary.
- 

In line with Ref. [96] one should note that "likelihood-free" can be a confusing term as the likelihood is indeed involved within this framework. By likelihood-free it is usually implied that direct evaluation of it is averted. Unfortunately, the acceptance rate in Alg. 2 is vanishingly small for highly dimensional data.

To illustrate this, envision a scenario where data  $\mathcal{D}_{\text{obs}}$  e.g. from a spectrum or counts from a detector is binned in to an array of  $B$  bins. A analogous procedure can be done for such simulated data  $\mathcal{D}_{\text{sim}}$  given a parameter  $\vartheta^*$ . Then

$$\begin{aligned}\mathcal{D}_{\text{obs}} &= [c_1, c_2, c_3, \dots, c_B], \\ \mathcal{D}_{\text{sim}} &= [c'_1, c'_2, c'_3, \dots, c'_B]\end{aligned}$$

where  $c_b, c'_b \in \mathbb{Z}$  denote integer counts in the  $b$ :th bin. Then, let the probability of a match between counts  $c_b = c'_b$  in the  $b$ :th bin read  $p_b$  assuming that this is independent between bins. Then, the probability to match everywhere (hence accept a proposal) is

$$p(\mathcal{D}_{\text{obs}} = \mathcal{D}_{\text{sim}}) = \prod_{b=1}^{b=B} p_b \quad (3.3)$$

and  $p(\mathcal{D}_{\text{obs}} = \mathcal{D}_{\text{sim}}) \rightarrow 0$  as  $B \rightarrow \infty$ . The probability of acceptance becomes even lower or impossible in the limit of continuous data. For instance, if  $c_b, c'_b$  were floating point numbers the probability  $p_b$  might be close to zero. As a result, the appeal for an exact match need to be relieved in order to have a feasible acceptance rate.

### 3.3 Approximate Bayesian computation

Having seen the difficulty arising in the requirement  $\mathcal{D}_{\text{obs}} = \mathcal{D}_{\text{sim}}$  the chain of logic that will yield ABC sampling is now delivered.

Noting that the rate of acceptance in Eq. (3.3) becomes significantly larger if one allows  $\mathcal{D}_{\text{obs}} \approx \mathcal{D}_{\text{sim}}$  it is possible to formulate the condition to accept samples when

$$\|\mathcal{D}_{\text{obs}} - \mathcal{D}_{\text{sim}}\| \leq h \quad (3.4)$$

where  $\|\cdot\|$  is a suitable distance metric and  $h \geq 0$  is a scale parameter sometimes referred to as the kernel size. Consequentially, samples are no longer drawn from the exact posterior distribution (unless  $h = 0$ ) but rather an approximate one  $\pi_{\text{ABC}}(\vartheta|\mathcal{D}_{\text{obs}})$ . Thus, choosing  $h$  becomes a trade-off between the acceptance rate and quality of the approximate posterior. Still, large dimensionality impairs the selection rule given by Eq. (3.4). To clarify this, take the aforementioned example of binned data. Without loss of generality one can take the Euclidean distance metric and express Eq. (3.4) as

$$\left( \sum_{b=1}^{b=B} (c_b - c'_b)^2 \right)^{1/2} \leq h \quad (3.5)$$

for some fixed value of  $h$ . In a favorable scenario when the difference  $c_b - c'_b \sim \Delta \ll 1$  varies negligibly between bins one can naively state Eq. (3.5) as

$$B \leq (h/\Delta)^2. \quad (3.6)$$



As a consequence, the dimension of  $\mathcal{D}_{\text{obs}}, \mathcal{D}_{\text{sim}}$  is bounded by the scale parameter and the average error between entries. Stimulated by this example, the need for dimensionality reduction becomes crucial. Further, it is desirable that this reduction retains information that characterize the data. To achieve this, one can introduce summary statistics

$$S : \mathbb{R}^B \mapsto \mathbb{R}^{\bar{B}} \quad (3.7)$$

being any collection of descriptive quantities derived from the data having dimension  $\bar{B} \ll B$ . As an example one can form the collection  $S(\mathcal{D}) = (\mu, \sigma^2)$  containing the sample mean and variance of data  $\mathcal{D}$ . Hereon,  $\mathcal{D}$  denote either of the data  $\mathcal{D}_{\text{sim/obs}}$  retrieved from a model or experiment and  $S(\mathcal{D})$  denote conversion of data into summary statistics. Logically, there is no restriction in defining the summary statistics other than being data descriptive. However, it should be noted that choosing a suitable set may be strongly dependent on the problem at hand, which will be exemplified later on.

Instead of computing the distance between  $\mathcal{D}_{\text{sim}}$  and  $\mathcal{D}_{\text{obs}}$  one can obtain a set of summary statistics  $S(\mathcal{D}) = [s_1, s_2, \dots, s_{\bar{B}}]$  and evaluate the distance in this subspace

$$\|S(\mathcal{D}_{\text{sim}}) - S(\mathcal{D}_{\text{obs}})\| \leq h. \quad (3.8)$$

While the inequality (3.8) is a viable criterion, it is a binary trial in the sense that the probability of acceptance is either 1 or 0. This does not discriminate between cases when the left-hand side of (3.8) evaluates to zero or boundary cases equating to  $h$ . This suggests a smooth scaling between the cases, attainable by defining

$$K : \mathbb{R}^{\bar{B}} \mapsto \mathbb{R} = K \left( \frac{\|S(\mathcal{D}_{\text{sim}}) - S(\mathcal{D}_{\text{obs}})\|}{h} \right) \quad (3.9)$$

commonly referred to as a kernel function and examples of them can be seen in Fig. 3.1. Here, the scale parameter  $h$  enters the argument of  $K$  which dictates the range of the function.

Lastly, reinforcing Alg. 2 with the improvements via dimensionality reduction, ABC sampling is obtained:

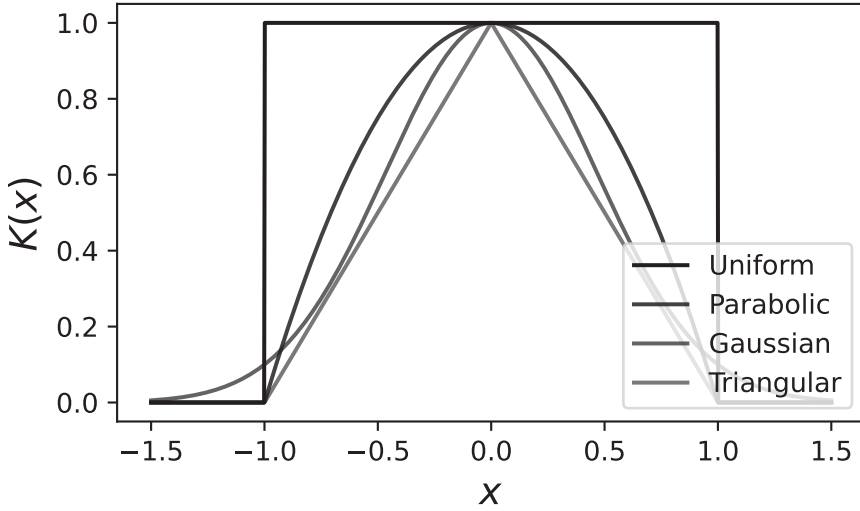


**Figure 3.1:** Examples of four different kernel functions. The uniform kernel amounts to accepting or rejecting based on Eq. (3.8).

---

**Algorithm 3:** ABC sampling algorithm

---

- 1: Sample a proposal  $\vartheta^*$  from the prior distribution :  $\vartheta^* \sim \pi(\vartheta)$ .
  - 2: Generate data from the model given the proposal:  $\mathcal{D}_{\text{sim}} \sim \mathcal{M}(\vartheta^*)$ .
  - 3: Accept the sample with probability  $K\left(\frac{\|S(\mathcal{D}_{\text{sim}}) - S(\mathcal{D}_{\text{obs}})\|}{h}\right)$ .
  - 4: Repeat (1)-(3) as many time necessary.
-

In addition to model parameters  $\vartheta$  there can exist latent parameters  $s$  in a realistic scenario. These are uncontrollable variables that significantly impact the result of experiments, potentially masking the effects attributed to  $\vartheta$ . However, a core strength of ABC lies in the freedom to select summary statistics. If done correctly the effects of  $\vartheta$  and  $s$  can be disentangled so that sampling is possible. This along with the demonstration of ABC will be presented shortly where a model on the effective mass of electrons and positrons due to quantum corrections is outlined.

To summarize, ABC sampling is a method that circumvent the direct calculation of the likelihood by employing repeated comparisons of results from simulations and experiments. While being a powerful tool, it come with a few drawbacks. First, there is no prescribed idea in choosing the scale parameter  $h$ . It can be estimated via trial and error or by investigating the dependence on the acceptance rate for the problem at hand. Second, the choice of summary statistics is problem dependent in the sense that they need to describe the data given a particular  $\vartheta$ . At the same time, they must be able to separate the effects ascribed to latent variables should they exist.

### 3.4 Effective mass model

By recapitulating the premise of this chapter, one is reminded that the combined magnitude of upcoming laser facilities and electron accelerators give the possibility to reach large values of  $\chi$ . The extremities of the physical laws at these values of  $\chi$  is an interesting matter for experimental studies. One prediction is the effective mass of electrons and positrons motivated in Ref. [69]. In making an experimental observation of such effects one can design a model with a parameter  $\vartheta$  so that its value can be inferred by comparing results of experiments to that of simulations with varying  $\vartheta$ . Again, the obstacle lies in measuring a signal which is masked by the predominant noise stemming from rates at low  $\chi$ . The goal is then to devise an experiment. In other words, propose an interaction geometry, assess the data to be measured and the method to process it so that the value of  $\vartheta$  can be inferred.

The model  $\mathcal{M}$ , based on the idea behind the effective mass change is now designed. It was mentioned in the introduction that theoretical knowledge

is limited for the QED rates in the nonperturbative regime, that is when  $\chi \gtrsim 1600$  [38, 39]. The authors of Ref. [69] bring up the notion of an effective mass for electrons and protons  $\tilde{m}_e$  as a result of quantum corrections. More specifically, they estimate it to be

$$\tilde{m}_e^2 = m_e^2 + \delta m_e^2 \approx m_e^2 (1 + 0.84 \alpha_f \chi^{2/3}) \quad (3.10)$$

and argue that the estimate given by Eq. (3.10) can gauge the order of magnitude of nonperturbative corrections in the regime  $\chi \lesssim 1600$ . The authors remark that the effective mass change is not necessarily the only such effect existing in this domain. This estimate is analogous to that of including a recoil correction to the classical rates in estimating the role of quantum effects in the regime  $\chi \lesssim 1$  (see supplementary material of Ref. [97]). From now on, the phenomenological model given by Eq. (3.10) is adopted and the value of  $0.84 \rightarrow \vartheta$  is retained, treating  $\vartheta$  as a parameter of the model  $\mathcal{M}(\vartheta)$ .

The effective mass appearing in Eq. (3.10) implies an effective value of  $\chi$  (mass enters Eq. (1.59) via the critical field):

$$\tilde{\chi}^{2/3} = \frac{\chi^{2/3}}{1 + \vartheta \alpha_f \chi^{2/3}} \quad (3.11)$$

where  $\tilde{\chi}$  denote its effective value. Now, the goal is to devise an experiment capable of inferring the value of  $\vartheta$ . For this, an interaction scheme in which a single electron with longitudinal momentum  $\mathbf{p}_z = -m_e c \gamma_e$  impinge a plane wave pulse with electric field is employed

$$E_x(z, t) = (1 - d) E_0 \sin(k\xi) \cos^2(\xi\pi/L) \cdot \Pi[\xi, -L/2, L/2] \quad (3.12)$$

where  $E_0$  is the peak electric field amplitude,  $\xi = z - ct$  is the moving coordinate,  $k$  and  $L$  are the pulse wavenumber and length respectively and  $\Pi$  is a function which is unity inside  $\xi \in [-L/2, L/2]$  and zero elsewhere. Here, a latent parameter,  $0 \leq d \leq 1$ , has been introduced to model any amplitude discrepancy present in a real experiment. For instance, the timing of the laser-electron collision could vary or the impact could occur off-axis and so forth. As a result, the model is dependent on two parameters  $\mathcal{M} = \mathcal{M}(\vartheta, d)$  of which the latter is uncontrollable. One may argue that a realistic setup ought to include a tightly focused laser pulse and an electron bunch with specified shape. This is true, but as a proof of principle one can consider

this basic layout and the intent is to progressively improve the scheme in upcoming research works. In addition, the formation of electron-positron pairs is neglected which prohibit the onset of QED cascades and consider only the emission of photons from the electron.

Having determined the interaction geometry the data  $\mathcal{D}$  measured from it must be assessed. Hereinafter,  $\mathcal{D}$  labels any data stemming from either a simulation  $\mathcal{D}_{\text{sim}}$  or the experiment  $\mathcal{D}_{\text{obs}}$ . In line with Sec. 2.1 an option is to measure the photon energy spectrum. However, even by neglecting QED cascades this is problematic. To see this, recall that the emitted energy is governed by Eq. (1.60) which depends on the value of  $\chi$  at the instance of emission. Moreover,  $\chi$  is dependent on  $\vartheta$  by virtue of Eq. (3.11) but also on  $d$  as it decreases the electric field amplitude experienced by the electron. Combining these facts it appears that the effects of  $\vartheta$  and/or  $d$  can produce similar values of  $\chi$ . For instance, compare the two cases where  $d = 0, \vartheta \neq 0$  and  $d \neq 0, \vartheta = 0$ . The value of  $\chi$  according to Eq. (3.11) in the former case is on the order of

$$\sim \frac{\chi_0}{\left(1 + \alpha_f \vartheta \chi_0^{2/3}\right)^{3/2}} \quad (3.13)$$

where  $\chi_0 = \gamma_e E_0 / E_{\text{crit}}$  is the peak value of  $\chi$ . In the latter case, the value of  $\chi$  is lowered due to nonzero  $d$  :

$$\sim (1 - d) \cdot \chi_0. \quad (3.14)$$

Evidently, Eqs. (3.13) and (3.14) coincide if

$$d \sim 1 - \left(1 + \theta \alpha_f \chi_0^{2/3}\right)^{-3/2}. \quad (3.15)$$

Consequentially, there exist values of  $\vartheta$  and  $d$  that yield comparable values of  $\chi$  and hence results in similar photon spectra. In turn, any summary statistics derived from it will be near-identical. When this happens, step 3 of Alg. 3 is no longer accurate as it will confuse the effects between  $\vartheta$  and  $d$ . It is concluded that the energy spectrum alone is not indicative enough to infer the value of  $\vartheta$  since the experiment (and hence model) is dependent on the uncontrollable variable  $d$ .

### 3.5 Latent variable elimination

Spurred by the complication posed by the latent parameter  $d$ , the elimination of it by extending the information contained in  $\mathcal{D}$  and choosing suitable summary statistics is demonstrated.

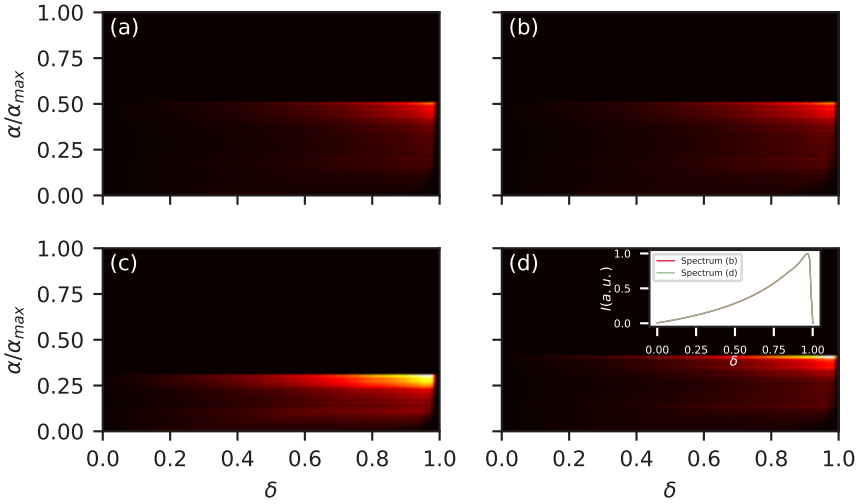


**Figure 3.2:** Heatmap of  $\mathcal{D}$  as a function of  $\delta$  and  $\alpha$  sampled from simulations. Here,  $\mathcal{D}$  is discretized by a grid with  $100 \times 100$  cells where (a)  $\vartheta = d = 0$ , (b)  $\vartheta = 1.0, d = 0$ , (c)  $\vartheta = 0, d = 0.4$  and (d)  $\vartheta = 0.0, d \approx 0.2$  with an inset showing the photon energy spectra of (b) and (d).

In identifying complementary data to that of the photon energy spectrum one can pose the question "Is there a quantity affected by  $d$  but not by  $\vartheta$  or vice versa?". Reminded by the discussion in Sec. 2.1 one can explore the option to include the angular spectrum of emitted photons. Because, the angle  $\alpha$  of a photon inherited from its parent electron is given by Eq. (2.2) of which the electron transverse momentum follows from Eq. (2.1), independent of  $\vartheta$ . In contrast, a non-zero value of  $d$  lowers the electric field strength and hence the transverse momentum of the electron. Therefore, the formed angle is smaller meaning that a property has been found that

might distinguish between the parameters  $\vartheta$  and  $d$ .

From this finding one can redefine  $\mathcal{D} = \mathcal{D}(\delta, \delta + \Delta\delta, \alpha, \alpha + \Delta\alpha)$  as the fractional energy distribution per unit frequency  $\Delta\omega$  and per unit angle  $\Delta\alpha$  as a function of  $\delta = \frac{\hbar\omega}{m_e c^2 \gamma_e}$  and  $\alpha$ . Theoretically,  $\mathcal{D}$  is a continuous function but here it is defined as a two dimensional grid sampled from simulations. Various samplings of  $\mathcal{D}$  from simulations can be observed in Fig. 3.2 where the parameters  $\vartheta$  and  $d$  have been varied. In the simulation corresponding to 3.2d the latent variable was chosen in line with Eq. (3.15) to mimic the energy spectrum of 3.2b where  $\vartheta = 1.0$ . The inset confirms the near-identical features of the spectra whereas the angular components of  $\mathcal{D}$  (along the y-axis) are different in terms of the cutoff. For reference, all simulation parameters can be found in Tab. 3.1.

It is now time to discuss the set of summary statistics to extract from this distribution. Without loss of generality one can evaluate moments of  $\mathcal{D}$

$$M_{i,j} = \int \int \mathcal{D}(\delta, \delta + \Delta\delta, \alpha, \alpha + \Delta\alpha) \delta^i \alpha^j d\delta d\alpha \quad (3.16)$$

where  $M_{i,j}$  denote moments of order  $i$  in  $\delta$  and  $j$  in  $\alpha$  of the distribution  $\mathcal{D}$ .

In choosing summary statistics based on Eq. (3.16) one might speculate about the strategy to find a set  $M_{i,j}$  that separate the effects of  $\vartheta$  and  $d$ . In Sec. 3.3 a remark was made that there is no prescribed way in making the choice of this set. Since summary statistics are problem dependent, it is up to the experimentator to decide a suitable approach. Nonetheless, it is always possible to investigate the dependence of a chosen statistic as a function of the parameters. In this case, one could visualize a number of the moments from Eq. (3.16) as a function of  $\vartheta$  and  $d$  to see if there exist a unique set of moments for every point in this parameter space. Two examples can be viewed in Fig. 3.3 where four distinct moments are compared to each other. Obviously, the set of moments in 3.3a is a good choice as the contours are not parallel anywhere, suggesting a nearly unique pair for every  $\vartheta$  and  $d$ . In contrast, Fig. 3.3b depicts a scenario when the contours become parallel at several points in the parameter space, confusing the effects of  $\vartheta$  and  $d$ . Thus, selecting  $M_{0,0}$  and  $M_{1,2}$  is a feasible input for ABC sampling. It is

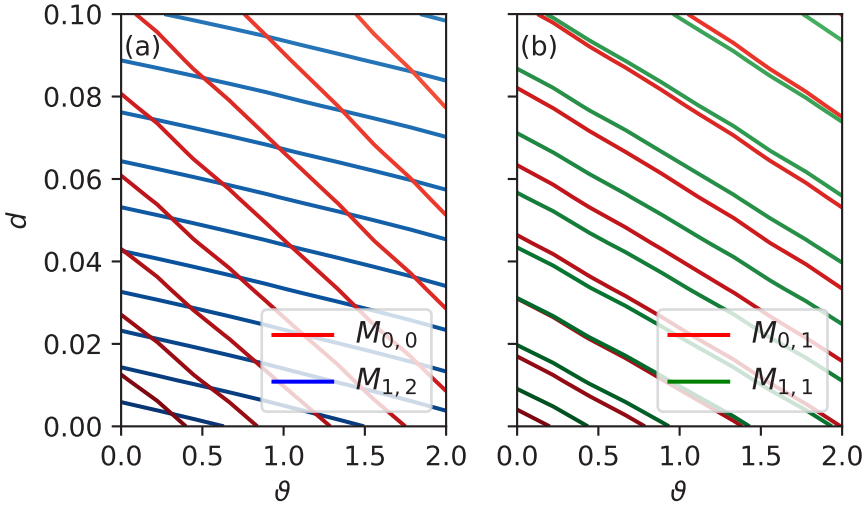


**Figure 3.3:** Contours of  $M_{i,j}$  in the space of  $\vartheta$  and  $d$ , (a) comparison of  $M_{0,0}$  and  $M_{1,2}$  and (b) comparison of  $M_{0,1}$  and  $M_{1,1}$ . The darkness of the contours indicate large values  $M_{i,j}$  but is unimportant for the comparison.

Simulation parameter	$a_0$	$\gamma_e$	$L$	$\chi_0$	$\lambda$
Value	100	$\sim 10^5$	$4.8 \mu\text{m}$	$\sim 100$	$0.8 \mu\text{m}$

**Table 3.1:** A table of simulation parameters for the interaction between the plane wave pulse and the electron.

likely that there exist several moments that satisfy this condition. However, the aim is to perform the ABC analysis not using a too complicated compilation of summary statistics. Thus, the choice  $S(\mathcal{D}) = (M_{0,0}, M_{1,2})$  is sufficient.

Having proposed the interaction geometry, the data to be measured and the choice of summary statistics the demonstration of the ABC algorithm to infer the value of  $\vartheta$  is in order. This final element of the ABC implementation will be given in the introductory text for paper B found in Sec. 4.2.



## 4 Current and upcoming research

In this chapter we place summaries of the appended papers. Sec. 4.1 restates and extends the findings of Ch. 2 which summarizes paper A. Following the achievements of photon-based signal selection and optimal focusing for maximum  $\chi$  value in experiments, we here introduce and compute a *signal ratio* and an *effective cross-section*. These quantities propel the final conclusion of paper A stating that a signal based on electron energy loss would require orders of magnitude more experimental shots to that of photon-based diagnostics in detecting a significant deviation of the rates. The summary of paper B is found in Sec. 4.2 which gives an overview of Ch. 3 but extends the analysis by providing the approximate posterior from sampling the parameter  $\vartheta$  via ABC sampling. The results strongly indicate that our proposed experimental scheme is worth elaborating further on. Primary improvements in this matter range from realistic laser pulse and electron bunch modeling as well as the inclusion of background noise, such as QED cascades. The thesis is concluded with a few words on the future prospects of this research area.

### 4.1 Summary of paper A

Paper A conveys two substantial ideas: How to extract SFQED signals in laser-electron collision experiments and the role of optimal laser focusing to attain large values of  $\chi$ . It is recommended to have covered Ch. 2 to be equipped with the relevant expressions and nomenclature associated with this summary.

The premise to the first idea comes from the obstacles in measuring SFQED rates at large values of  $\chi$  through electron energy-loss:

- The probabilistic nature of the QED rates gives "noisy" data.
- Measured energy loss of an electron due to the emission of a high-energy photon is identical to that of multiple low-energy emissions.
- There is no diagnostic capable in determining the exact electromagnetic fields within the experiment, hence the exact value of  $\chi$ .

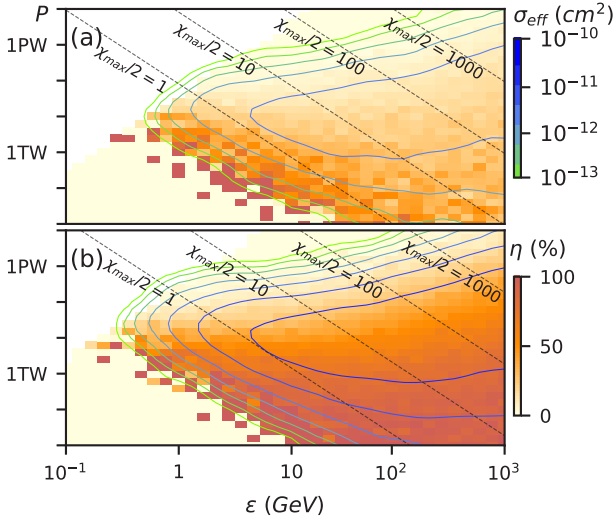


**Figure 4.1:** Parameter scan of the signal ratio  $\eta$  and effective cross section  $\sigma_{\text{eff}}$  for (a) linear polarization and (b) circular polarization. Adapted from [72].

- Shot-to-shot variations such as ill-timed collisions or misalignment impairs the signal.
- Electrons can radiate away the majority of their energy before reaching the strong-field region, restricting their ability to reach high  $\chi$ .
- QED cascades provide an immense background noise of low-energy photons and electron-positron pairs.

Here we reason that if the electron beam is unfocused, the strong-field region is formed within a uniform stream of particles, mitigating any spatiotemporal jitter in the experiment. As for signal extraction, we argue that emitted photons pose a feasible signal as they retain the angle of deviation  $\alpha$  and are more prone to escape the strong-field region of the laser.

Nonetheless, there are phase dependencies within the laser field that inhibit high  $\chi$  emissions at  $\alpha \approx 0$  which is shared with background emissions. A fortunate finding was that switching the polarization from linear to circu-

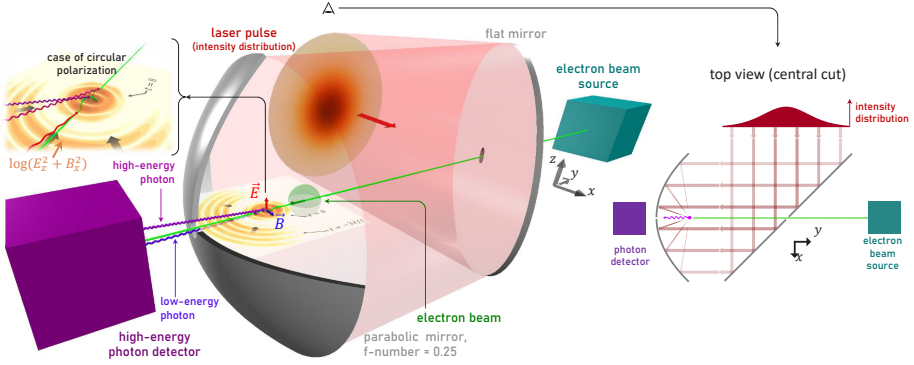


**Figure 4.2:** A possible experimental layout for creating and colliding a bidipole pulse into a beam of electrons (deviation angles are exaggerated). The leftmost inset displays the interaction in the case of circular polarization whereas the rightmost inset illustrates the view of the scheme from above. Adapted from [72].

lar makes  $\chi$  and  $\alpha$  correlated. As a result, photons with large  $\alpha$  were likely emitted at large  $\chi$ . Secondly, if a photon has high energy it is unlikely that its parent electron underwent emission prior to it, separating these from the background. We concluded that of all photons, the ones with large  $\alpha$  and high energy would constitute a viable signal despite the presence of substantial background. Our second achievement was to find the optimal focusing of a laser to maximize the value of  $\chi$  in such experiments. We defined this maximization problem, expressing the solution in terms of the Maxwell equations in a multipole representation. We then appeal to the expression for  $\chi$ , arguing that its maximum is satisfied at the origin. In solving this we found that the solution was a sum of two dipole waves which we refer to as a bidipole wave. The derivation and prospects of them were outlined in Secs. 2.3-2.6.

We performed simulations with a bidipole pulse propagating into a stream of electrons to demonstrate the capability of both achievements in a real experiment. A potential layout for this experiment can be seen in Fig. 4.2. Concisely, the simulations were repeated for a discrete set of points in the parameter space of the input power  $P$  and initial electron beam energy  $\epsilon$ . To quantify the outcome, we defined a signal ratio

$$\eta = \frac{N_{\text{signal}}}{N_{\text{total}}} \quad (4.1)$$

where  $N_{\text{total}}$  represent all photons at the detector having  $\alpha > 0.6\alpha_{\text{max}}$  and energy  $E_\gamma > 0.5m_e c^2 \gamma_e$  of which  $N_{\text{signal}}$  also fulfill  $\chi > 0.5\chi_{\text{max}}$  from parent electrons that hadn't lost more than 1% energy prior to emission. In this case,  $\alpha_{\text{max}} \sim a_0^{\text{max}}/\gamma_e$  where  $a_0^{\text{max}}$  denote the peak dimensionless amplitude and  $\chi_{\text{max}}$  denote the maximal value of  $\chi$  attained at the center of the bidipole wave. In addition to the signal ratio, we introduce an effective cross section of the interaction

$$\sigma_{\text{eff}} = \frac{N_{\text{signal}}}{n_e \tau_l c} \quad (4.2)$$

where  $n_e$  is the electron density and  $\tau_l$  the bidipole pulse duration. A core result from our paper is the parametric scan seen in Fig. 4.1. This motivated us to estimate the number of shots needed to reach a  $3\sigma$  confidence level in detecting a 1% deviation of the emission rates at  $\chi \gtrsim 10$ . We considered a 10 GeV electron beam with total charge 100 pC spread over a spherical volume with radius  $2.5 \mu\text{m}$  ( $n_e \approx 10^{19} \text{ cm}^{-3}$ ) and a bidipole pulse with a 5-cycle duration. As a test statistic we chose  $N_{\text{exp}}$  total shots with cumulative  $N_{\text{total}}$  so that  $3\sigma_{N_{\text{exp}}} \leq 0.01N_{\text{signal}}$  is the desired statistical significance where  $\sigma_{N_{\text{exp}}} \approx \sqrt{N_{\text{total}}}$ . With these parameters and the aid of Fig. 4.1a,  $\chi_{\text{max}}/2 \gtrsim 10$  is reached with  $P \sim 100 \text{ TW}$  so that  $\sigma_{\text{eff}} \sim 10^{-11} \text{ cm}^{-3}$  and  $\eta \sim 0.1$ . This implies  $N_{\text{signal}} \sim 5 \cdot 10^5$  signal photons per shot and the criterion is  $\left(\frac{3}{0.01\eta}\right)^2 \sim 10^7$  photons in total, demanding 200 shots. An analogous derivation implied that in measuring the electron energy loss the number shots required was  $5 \cdot 10^5$  times larger to that of photon-based diagnostics.

We end the paper by stating that photons based on their deviation and energy can provide detectable signals of SFQED rates at  $\chi \sim 10-100$  reachable with PW-10-GeV-class facilities. We further highlight that the use of optimal focusing to increase  $\chi$  values is beneficial, of which the bidipole wave offers the optimal value. However, probing  $\chi \sim 1000$  requires higher intensity and/or electron energy which precipitates further studies of electron injection and pulse steepening.

## 4.2 Summary of paper B

In paper B we propose an experimental layout capable of gauging the extreme limits of interest for QED. That is, we suggest an interaction scheme, the data to be measured from this setup and a statistical framework that enables the inference of such parameters. Again, we advise the reader to consult Ch. 3 to acquire any notation and definitions used in this summary.

We stress in paper B that experiments designed to test QED predictions around its breakdown limit are prone to noisy data stemming primarily from QED cascades. Secondly, misalignment inherent in such experiments adds to this obstacle. To mitigate this we explain the benefit in adopting Bayesian methods to infer parameters of aforementioned predictions embedded in models. Particularly interesting are techniques that sample parameters by comparing results of the experiment to that of simulations specified by a model. This can bypass direct evaluation of the likelihood which is many times problematic due to computational demands or other intractabilities. We demonstrated that this technique is susceptible to data of large dimensionality as the sampling rate is rendered unfeasible. In making the rate practical, we appeal to summary statistics and kernel functions in order to reduce the dimensionality of the data. All of this culminates in what is known as approximate Bayesian computation (ABC).

We then elaborate on our layout by providing a proof of principle by adopting the notion of a mass shift for electrons and positrons mentioned in Ref. [69]. This is argued to be one of many potentially measurable nonperturbative effects of QED. From it we constructed a model with a parameter  $\vartheta$  to signify the strength of the mass shift. Next, we developed the simulation geometry comprised of a plane wave pulse impinging a single counter-propagating electron. Appealing to the realism in an experiment we included a latent parameter  $d$  which mimics any uncontrollable features which reduce the laser amplitude experienced by the electron. We mention examples of such features as off-axis or ill-timed collisions. As our prospects are based on first principles we chose to neglect pair formation to avoid noisy data from QED cascades.

Having defined the setup and model we assessed the role of data measured

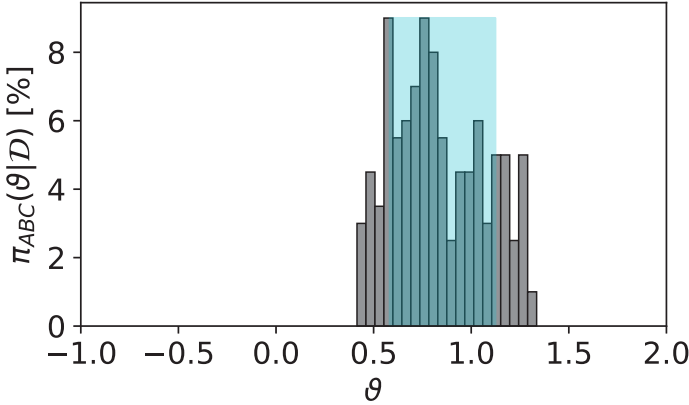


**Figure 4.3:** ABC sampled posterior for  $\vartheta$  with  $N_{\vartheta} = 1600$  accepted samples using  $h = 0.1$ . The shaded region indicate the 68% credible interval  $0.58 < \vartheta < 1.13$ .

in experiments. We gave the example that an experimentator can measure the photon energy spectrum and use this data for the inference. However, we then argued that a nonzero value of  $\vartheta$  will have the same effect on the spectrum to that of  $d \neq 0$ , suggesting the necessity of using complementary data to disentangle the influence ascribed to latent variables. Based on this and results of paper A we also included the angular spectrum of the emitted photons as  $\vartheta$  has no effect on it contrary to  $d$ . Combining the information contained in these properties we proposed to measure a fractional energy distribution per unit frequency and per unit angle as a function of normalized photon energy and angle.

We underlined that selecting informative data is not enough as the disentanglement of parameters ultimately depend on the choice of summary statistics. For our model in consideration we showed that a set of summary statistics in the form of statistical moments could be used to separate the effects of  $\vartheta$  and  $d$  (recall Fig. 3.3 and the discussion therein). In choosing the data and summary statistics we were in a position to sample  $\vartheta$  in simulations by setting the experiment as a *blind test*. That is, we fix the value of  $\vartheta = \vartheta_{\text{true}} = 0.84$  prior to the analysis while  $0 \leq d \leq 1$  is allowed to vary randomly. Our paper culminates in giving the approximate posterior using ABC for a given scale

parameter  $h$  and collected samples  $N_{\theta}$  visible in Fig. 4.3. Although the analysis was based on first principles, it strongly suggests that ABC can possibly be used as a tool to benchmark models of QED in extreme limits of interest. We discuss that a more realistic proof of principle will impact the computational load of the simulation as well as the ABC sampling rate. We explained that these difficulties can be combatted by the use of machine learning methods and high-performance computers.

### 4.3 Conclusions

In this thesis, we have provided the principles of radiation reaction in the scope of laser-electron collision experiments, stimulating the interest to study its extreme limits currently unreachable by contemporary facilities. In addition to this, we have given the theoretical grounds for signal extraction in such experiments using photon-based diagnostics and the opportunity to boost  $\chi$  values with optimized focusing in which the maximum was found to be achieved by the bidipole wave solution. Likewise, we have dedicated a part to the introduction of Bayesian statistics and the discussion on sampling techniques which avoid direct evaluation of the likelihood. Of specific interest were methods utilizing data obtained from repeated simulations and experiments. This motivated the use of ABC sampling and we put emphasis on the role of data selection and summary statistics. The latter also vital in separating effects of model parameters to that of latent variables.

Further, we presented the achievements of paper A by introducing strategies to select SFQED signal photons in such experiments and demonstrated the significance of optimal focusing in unfocused electron beams to provide large values of  $\chi$  where we derived the optimal solution. Then, we argued that emitted photons having a large angle of deviation  $\alpha$  (hence high  $\chi$  value in the case of a circularly polarized wave) and energy  $\hbar\omega$  carry the SFQED signal. We introduced and computed the signal ratio  $\eta$  and effective cross section  $\sigma_{\text{eff}}$  in simulations with a bidipole pulse colliding with a stream of high-energy electrons. With these results we concluded that the number of shots needed in an experiment to detect a 1% deviation of the QED rates on a  $3\sigma$  confidence level is  $\sim 10^5$  larger for electron energy-based diagnostics to that of photon-based.

We also show the implementation of ABC sampling on a model which encapsulates the idea of an effective electron/positron mass stemming from quantum corrections. Here the parameter of the model tunes their effective mass and we include a latent parameter  $d$ , lowering the experienced laser amplitude for electrons due to any mismatch in the collision experiment. Our results provide a strong evidence of a successful inference based on selecting data and summary statistics that separate  $\vartheta$  and  $d$ .

As for future research, improvements of paper B holds great interest due to the strong inference obtained from first principles. Simulating a realistic tightly focused laser, accounting for QED cascades, modeling electron bunches and including more sophisticated latent parameters are examples of improvements one can make to further elaborate proposals for experiments. Even if these additions pose a computational demand, convergence of ABC sampling can be accelerated by the use of machine learning methods to suggest better sample proposals. Additionally, the use of supercomputer clusters may allow many independent ABC samplers to run in parallel to assemble the posterior. We are content with the findings of paper A, primarily because the bidipole wave is the optimal solution in reaching values of high  $\chi$  but also because the results appeal to upcoming laser-matter facilities.



## References

- [1] A. Einstein, “On the quantum theory of radiation,” *The Old Quantum Theory: The Commonwealth and International Library: Selected Readings in Physics*, p. 167, 2016.
- [2] J. P. Gordon, H. J. Zeiger, and C. H. Townes, “The maser—new type of microwave amplifier, frequency standard, and spectrometer,” *Phys. Rev.*, **99**, pp. 1264–1274, 4 Aug. 1955. DOI: 10.1103/PhysRev.99.1264. [Online]. Available: <https://link.aps.org/doi/10.1103/PhysRev.99.1264>.
- [3] T. H. Maiman *et al.*, “Stimulated optical radiation in ruby,” 1960.
- [4] J. Bromberg, “The birth of the laser,” *Physics Today*, **41**, no. 10, p. 26, 1988.
- [5] D. F. Nelson, R. J. Collins, and W. Kaiser, “Bell labs and the ruby laser,” *Physics today*, **63**, no. 1, p. 40, 2010.
- [6] T. F. Deutsch, “Medical applications of lasers,” *Physics today*, **41**, no. 10, pp. 56–63, 1988.
- [7] T. H. Maiman, “Laser applications,” *Physics Today*, **20**, no. 7, p. 24, 1967.
- [8] M. Hohenleutner *et al.*, “Real-time observation of interfering crystal electrons in high-harmonic generation,” *Nature*, **523**, no. 7562, pp. 572–575, 2015.
- [9] T. Rybka, M. Ludwig, M. F. Schmalz, V. Knittel, D. Brida, and A. Leitensestorfer, “Sub-cycle optical phase control of nanotunnelling in the single-electron regime,” *Nature Photonics*, **10**, no. 10, pp. 667–670, 2016.
- [10] P. B. Corkum and F. Krausz, “Attosecond science,” *Nature physics*, **3**, no. 6, pp. 381–387, 2007.
- [11] M. Schultze *et al.*, “Controlling dielectrics with the electric field of light,” *Nature*, **493**, no. 7430, pp. 75–78, 2013.
- [12] F. Krausz and M. I. Stockman, “Attosecond metrology: From electron capture to future signal processing,” *Nature Photonics*, **8**, no. 3, pp. 205–213, 2014.
- [13] I. Pupeza *et al.*, “High-power sub-two-cycle mid-infrared pulses at 100 mhz repetition rate,” *Nature Photonics*, **9**, no. 11, pp. 721–724, 2015.
- [14] M. J., “Intense laser-plasma interactions,” Ph.D. dissertation, Chalmers University of Technology, 2019.

- [15] M. CLUNG, "Hellwarth (r. w.), giant optical pulsations from ruby," *J. Applied Physics*, **33**, no. 1, pp. 828–829, 1962.
- [16] R. Fork, B. Greene, and C. V. Shank, "Generation of optical pulses shorter than 0.1 psec by colliding pulse mode locking," *Applied Physics Letters*, **38**, no. 9, pp. 671–672, 1981.
- [17] D. Strickland and G. Mourou, "Compression of amplified chirped optical pulses," *Optics communications*, **55**, no. 6, pp. 447–449, 1985.
- [18] I. Ross, P. Matousek, M. Towrie, A. Langley, and J. Collier, "The prospects for ultrashort pulse duration and ultrahigh intensity using optical parametric chirped pulse amplifiers," *Optics Communications*, **144**, no. 1-3, pp. 125–133, 1997.
- [19] V. Bagnoud, I. A. Begishev, M. J. Guardalben, J. Puth, and J. D. Zuegel, "5? hz, > 250? mj optical parametric chirped-pulse amplifier at 1053? nm," *Optics letters*, **30**, no. 14, pp. 1843–1845, 2005.
- [20] H. Kiriya *et al.*, "High-contrast, high-intensity laser pulse generation using a nonlinear preamplifier in a ti: Sapphire laser system," *Optics letters*, **33**, no. 7, pp. 645–647, 2008.
- [21] I. Musgrave *et al.*, "Review of laser diagnostics at the vulcan laser facility," *High Power Laser Science and Engineering*, **3**, 2015.
- [22] C. Hooker *et al.*, "The astra gemini project—a dual-beam petawatt ti: Sapphire laser system," *Journal de Physique IV (Proceedings)*, EDP sciences, vol. 133, 2006, pp. 673–677.
- [23] C. Radier *et al.*, "10 pw peak power femtosecond laser pulses at eli-np," *High Power Laser Science and Engineering*, **10**, e21, 2022.
- [24] D. Papadopoulos *et al.*, "The apollon 10 pw laser: Experimental and theoretical investigation of the temporal characteristics," *High Power Laser Science and Engineering*, **4**, 2016.
- [25] R. Li, X. Liang, Y. Leng, and Z. Xu, "Progress of the sulf 10 pw laser project," *1st AAPPS-DPP meeting*, 2017.
- [26] A. Bashinov, A. Gonoskov, A. Kim, G. Mourou, and A. Sergeev, "New horizons for extreme light physics with mega-science project xcel," *The European Physical Journal Special Topics*, **223**, no. 6, pp. 1105–1112, 2014.
- [27] C. Hernandez-Gomez *et al.*, "The vulcan 10 pw project," *Journal of Physics: Conference Series*, IOP Publishing, vol. 244, 2010, p. 032 006.

- [28] B. Shen *et al.*, “Exploring vacuum birefringence based on a 100 pw laser and an x-ray free electron laser beam,” *Plasma Physics and Controlled Fusion*, **60**, no. 4, p. 044 002, 2018.
- [29] E. National Academies of Sciences, Medicine, *et al.*, *Opportunities in Intense Ultrafast Lasers: Reaching for the Brightest Light*. National Academies Press, 2018.
- [30] J. Reinhardt and W. Greiner, “Quantum electrodynamics of strong fields,” *Reports on Progress in Physics*, **40**, no. 3, p. 219, 1977.
- [31] G. Breit and J. A. Wheeler, “Collision of two light quanta,” *Physical Review*, **46**, no. 12, p. 1087, 1934.
- [32] A. Nikishov and V. Ritus, “Quantum processes in the field of a plane electromagnetic wave and in a constant field  $i$ ,” *Sov. Phys. JETP*, **19**, no. 2, pp. 529–541, 1964.
- [33] J. Schwinger, “On gauge invariance and vacuum polarization,” *Physical Review*, **82**, no. 5, p. 664, 1951.
- [34] J. W. Yoon *et al.*, “Achieving the laser intensity of  $5.5 \times 10^{22}$  w/cm<sup>2</sup> with a wavefront-corrected multi-pw laser,” *Optics express*, **27**, no. 15, pp. 20 412–20 420, 2019.
- [35] T. Blackburn, “Radiation reaction in electronbeam interactions with high-intensity lasers,” *Reviews of Modern Plasma Physics*, **4**, Dec. 2020. DOI: 10.1007/s41614-020-0042-0.
- [36] A. Ilderton and G. Torgrimsson, “Radiation reaction in strong field qed,” *Physics Letters B*, **725**, no. 4-5, pp. 481–486, 2013.
- [37] A. Gonoskov, T. Blackburn, M. Marklund, and S. Bulanov, “Charged particle motion and radiation in strong electromagnetic fields,” *Reviews of Modern Physics*, **94**, no. 4, p. 045 001, 2022.
- [38] V. Ritus, “Radiative corrections in quantum electrodynamics with intense field and their analytical properties,” *Annals of Physics*, **69**, no. 2, pp. 555–582, 1972, ISSN: 0003-4916. DOI: [https://doi.org/10.1016/0003-4916\(72\)90191-1](https://doi.org/10.1016/0003-4916(72)90191-1). [Online]. Available: <https://www.sciencedirect.com/science/article/pii/0003491672901911>.
- [39] A. Fedotov, “Conjecture of perturbative qed breakdown at  $2/3$  1,” *Journal of Physics: Conference Series*, **826**, no. 1, p. 012 027, Mar. 2017. DOI: 10.1088/1742-6596/826/1/012027. [Online]. Available: <https://dx.doi.org/10.1088/1742-6596/826/1/012027>.
- [40] D. Burke *et al.*, “Positron production in multiphoton light-by-light scattering,” *Physical Review Letters*, **79**, no. 9, p. 1626, 1997.

- [41] C. Bula *et al.*, “Observation of nonlinear effects in Compton scattering,” *Physical Review Letters*, **76**, no. 17, p. 3116, 1996.
- [42] J. Cole *et al.*, “Experimental evidence of radiation reaction in the collision of a high-intensity laser pulse with a laser-wakefield accelerated electron beam,” *Physical Review X*, **8**, no. 1, p. 011 020, 2018.
- [43] K. Poder *et al.*, “Experimental signatures of the quantum nature of radiation reaction in the field of an ultraintense laser,” *Phys. Rev. X*, **8**, p. 031 004, 3 Jul. 2018. DOI: 10.1103/PhysRevX.8.031004. [Online]. Available: <https://link.aps.org/doi/10.1103/PhysRevX.8.031004>.
- [44] J. D. Jackson, *Classical electrodynamics*, 1999.
- [45] M. Abraham, *Prinzipien der dynamik des elektrons*. JA Barth, 1903.
- [46] M. Abraham, *Theorie der elektrizität*. BG Teubner, 1918.
- [47] H. A. Lorentz, *The theory of electrons and its applications to the phenomena of light and radiant heat*. Teubner, 1916, vol. 29.
- [48] L. D. Landau, *The classical theory of fields*. Elsevier, 2013, vol. 2.
- [49] J. Larmor, “Lxiii. on the theory of the magnetic influence on spectra; and on the radiation from moving ions,” *The London, Edinburgh, and Dublin Philosophical Magazine and Journal of Science*, **44**, no. 271, pp. 503–512, 1897.
- [50] M. R. Good and E. V. Linder, “Quantum power: A Lorentz invariant approach to Hawking radiation,” *The European Physical Journal C*, **82**, no. 3, pp. 1–6, 2022.
- [51] A. Liénard, *Champ électrique et magnétique produit par une charge électrique concentrée en un point et animée d’un mouvement quelconque*. G. Carré et C. Naud, 1898.
- [52] P. J. Nahin, *Oliver Heaviside: the life, work, and times of an electrical genius of the Victorian age*. JHU Press, 2002.
- [53] P. F. Dahl, *Flash of the Cathode Rays: A History of JJ Thomson’s Electron*. CRC Press, 1997.
- [54] D. J. Griffiths, *Introduction to electrodynamics*, 2005.
- [55] D. A. Burton and A. Noble, “Aspects of electromagnetic radiation reaction in strong fields,” *Contemporary Physics*, **55**, no. 2, pp. 110–121, 2014.
- [56] T. Blackburn, “Radiation reaction in electron–beam interactions with high-intensity lasers,” *Reviews of Modern Plasma Physics*, **4**, no. 1, pp. 1–37, 2020.

- 
- [57] A. H. Compton, "A quantum theory of the scattering of x-rays by light elements," *Physical review*, **21**, no. 5, p. 483, 1923.
- [58] V. B. Berestetskii, E. M. Lifshitz, and L. P. Pitaevskii, *Quantum Electrodynamics: Volume 4*. Butterworth-Heinemann, 1982, vol. 4.
- [59] V. Baier and V. Katkov, "Quantum effects in magnetic bremsstrahlung," *Physics Letters A*, **25**, no. 7, pp. 492–493, 1967.
- [60] T. Heinzl, A. Ilderton, and M. Marklund, "Finite size effects in stimulated laser pair production," *Physics Letters B*, **692**, no. 4, pp. 250–256, 2010.
- [61] I. Turcu, S. Balascuta, F. Negoita, D. Jaroszynski, and P. McKenna, "Strong field physics and qed experiments with eli-np  $2 \times 10$ pw laser beams," *AIP Conference Proceedings*, American Institute of Physics, vol. 1645, 2015, pp. 416–420.
- [62] M. Altarelli *et al.*, "Summary of strong-field qed workshop," *arXiv preprint arXiv:1905.00059*, 2019.
- [63] F. Salgado *et al.*, "Single particle detection system for strong-field qed experiments," *New Journal of Physics*, **24**, no. 1, p. 015 002, 2021.
- [64] H. Gies, F. Karbstein, and C. Kohlfürst, "All-optical signatures of strong-field qed in the vacuum emission picture," *Physical Review D*, **97**, no. 3, p. 036 022, 2018.
- [65] V. Yakimenko *et al.*, "Facet-ii facility for advanced accelerator experimental tests," *Physical Review Accelerators and Beams*, **22**, no. 10, p. 101 301, 2019.
- [66] H. Abramowicz *et al.*, "Letter of intent for the luxe experiment," *arXiv preprint arXiv:1909.00860*, 2019.
- [67] C. Baumann, E. Nerush, A. Pukhov, and I. Y. Kostyukov, "Probing non-perturbative qed with electron-laser collisions," *Scientific reports*, **9**, no. 1, pp. 1–8, 2019.
- [68] D. Blaschke *et al.*, "Dynamical schwinger effect and high-intensity lasers. realising nonperturbative qed," *The European Physical Journal D*, **55**, no. 2, pp. 341–358, 2009.
- [69] V. Yakimenko *et al.*, "Prospect of studying nonperturbative qed with beam-beam collisions," *Physical review letters*, **122**, no. 19, p. 190 404, 2019.
- [70] A. Matheron *et al.*, "Probing strong-field qed in beam-plasma collisions," *arXiv preprint arXiv:2209.14280*, 2022.

- [71] A. Gonoskov *et al.*, “Probing nonperturbative qed with optimally focused laser pulses,” *Physical review letters*, **111**, no. 6, p. 060 404, 2013.
- [72] C. Olofsson and A. Gonoskov, “Attaining a strong-field qed signal at laser-electron colliders with optimized focusing,” *Physical Review A*, **106**, no. 6, p. 063 512, 2022.
- [73] A. Fedotov, N. Narozhny, G. Mourou, and G. Korn, “Limitations on the attainable intensity of high power lasers,” *Physical review letters*, **105**, no. 8, p. 080 402, 2010.
- [74] A. Macchi, *A superintense laser-plasma interaction theory primer*. Springer Science & Business Media, 2013.
- [75] J. Magnusson *et al.*, “Laser-particle collider for multi-gev photon production,” *Physical review letters*, **122**, no. 25, p. 254 801, 2019.
- [76] N. Elkina *et al.*, “Qed cascades induced by circularly polarized laser fields,” *Physical Review Special Topics-Accelerators and Beams*, **14**, no. 5, p. 054 401, 2011.
- [77] H. T. Kim *et al.*, “Stable multi-gev electron accelerator driven by waveform-controlled pw laser pulses,” *Scientific reports*, **7**, no. 1, p. 10 203, 2017.
- [78] S. Bulanov, V. Mur, N. Narozhny, J. Nees, and V. Popov, “Multiple colliding electromagnetic pulses: A way to lower the threshold of  $e^+ e^-$  pair production from vacuum,” *Physical review letters*, **104**, no. 22, p. 220 404, 2010.
- [79] I. M. Bassett, “Limit to concentration by focusing,” *Optica Acta: International Journal of Optics*, **33**, no. 3, pp. 279–286, 1986.
- [80] T. M. Jeong, S. V. Bulanov, P. V. Sasorov, S. S. Bulanov, J. K. Koga, and G. Korn, “ $4\pi$ -spherically focused electromagnetic wave: Diffraction optics approach and high-power limits,” *Optics express*, **28**, no. 9, pp. 13 991–14 006, 2020.
- [81] J. C. Maxwell, “Viii. a dynamical theory of the electromagnetic field,” *Philosophical transactions of the Royal Society of London*, no. 155, pp. 459–512, 1865.
- [82] W. K. Panofsky and M. Phillips, *Classical electricity and magnetism*. Courier Corporation, 2005.
- [83] A. Gonoskov *et al.*, “Anomalous Radiative Trapping in Laser Fields of Extreme Intensity,” *Physical Review Letters*, **113**, no. 1, p. 014 801, Jul. 2014, ISSN: 0031-9007. DOI: 10.1103/PhysRevLett.113.014801. [Online]. Available: <http://link.aps.org/doi/10.1103/PhysRevLett.113.014801> %20<https://link.aps.org/doi/10.1103/PhysRevLett.113.014801>.

- [84] A. Gonoskov *et al.*, “Ultrabright GeV photon source via controlled electromagnetic cascades in laser-dipole waves,” *Physical Review X*, **7**, no. 4, p. 41 003, Oct. 2017, ISSN: 21603308. DOI: 10.1103/PhysRevX.7.041003. [Online]. Available: <https://link.aps.org/doi/10.1103/PhysRevX.7.041003>.
- [85] J. Magnusson *et al.*, “Multiple colliding laser pulses as a basis for studying high-field high-energy physics,” *Physical Review A*, **100**, no. 6, 2019, ISSN: 24699934. DOI: 10.1103/PhysRevA.100.063404.
- [86] J. Magnusson *et al.*, “Laser-particle collider for multi-GeV photon production,” *Physical Review Letters*, **122**, no. 25, Jun. 2019. DOI: 10.1103/physrevlett.122.254801. [Online]. Available: <https://doi.org/10.1103/physrevlett.122.254801>.
- [87] E. S. Efimenko *et al.*, “Laser-driven plasma pinching in e-e+ cascade,” *Physical Review E*, **99**, no. 3, p. 031 201, Mar. 2019, ISSN: 24700053. DOI: 10.1103/PhysRevE.99.031201. [Online]. Available: <https://journals.aps.org/pre/abstract/10.1103/PhysRevE.99.031201>.
- [88] E. S. Efimenko *et al.*, “Extreme plasma states in laser-governed vacuum breakdown,” *Scientific Reports*, **8**, no. 1, p. 2329, Mar. 2018, ISSN: 20452322. DOI: 10.1038/s41598-018-20745-y. [Online]. Available: <http://www.nature.com/articles/s41598-018-20745-y%20https://doi.org/10.1038/s41598-018-20745-y>.
- [89] I. Gonoskov, A. Aiello, S. Heugel, and G. Leuchs, “Dipole pulse theory: Maximizing the field amplitude from  $4\pi$  focused laser pulses,” *Physical Review A*, **86**, no. 5, p. 053 836, 2012.
- [90] C. Sheppard and K. Larkin, “Optimal concentration of electromagnetic radiation,” *Journal of Modern Optics*, **41**, no. 7, pp. 1495–1505, 1994.
- [91] W. M. Bolstad and J. M. Curran, *Introduction to Bayesian statistics*. John Wiley & Sons, 2016.
- [92] D. Fink, “A compendium of conjugate priors,” See <http://www.people.cornell.edu/pages/df36/CONJINTRnew%20TEX.pdf>, **46**, 1997.
- [93] S. T. Tokdar and R. E. Kass, “Importance sampling: A review,” *Wiley Interdisciplinary Reviews: Computational Statistics*, **2**, no. 1, pp. 54–60, 2010.
- [94] A. Doucet, N. d. Freitas, and N. Gordon, “An introduction to sequential monte carlo methods,” *Sequential Monte Carlo methods in practice*, Springer, 2001, pp. 3–14.

- [95] S. Brooks, A. Gelman, G. Jones, and X.-L. Meng, *Handbook of markov chain monte carlo*. CRC press, 2011.
- [96] S. A. Sisson, Y. Fan, and M. Beaumont, *Handbook of approximate Bayesian computation*. CRC Press, 2018.
- [97] V. Yakimenko *et al.*, “FACET-II facility for advanced accelerator experimental tests,” *Physical Review Accelerators and Beams*, **22**, no. 10, Oct. 2019. DOI: 10.1103/physrevaccelbeams.22.101301. [Online]. Available: <https://doi.org/10.1103/physrevaccelbeams.22.101301>.



## 5 Research papers

In this final chapter the reader can find the two appended papers :

### **Paper A**

C. OLOFSSON AND A. GONOSKOV. "Attaining a strong-field QED signal at laser-electron colliders with optimized focusing". *Phys. Rev. A* **106**, 063512 .

DOI: <https://doi.org/10.1103/PhysRevA.106.063512>

### **Paper B**

C. OLOFSSON AND A. GONOSKOV. "Prospects for statistical tests of strong-field quantum electrodynamics with high-intensity lasers". *arXiv preprint*: **arXiv:2303.00568**


DOI: <https://doi.org/10.48550/arXiv.2303.00568>



# Paper A

C. OLOFSSON AND A. GONOSKOV. "Attaining a strong-field QED signal at laser-electron colliders with optimized focusing". *Phys. Rev. A* **106**, 063512



**Attaining a strong-field QED signal at laser-electron colliders with optimized focusing**Christoffer Olofsson  and Arkady Gonoskov*Department of Physics, University of Gothenburg, 41296 Gothenburg, Sweden* (Received 7 July 2022; revised 31 October 2022; accepted 6 December 2022; published 22 December 2022)

Colliding bunches of high-energy electrons with intense laser pulses provides a basis for studying strong-field QED processes enabled by high values of quantum nonlinearity parameter  $\chi$ . Nevertheless, the signal deconvolution is intricate due to the probabilistic nature of the processes and shot-to-shot variation of the impact parameter, which disfavors the use of tight focusing. We propose a concept for distinguishing the signal of high- $\chi$  emissions that enables the use of optimal focusing to attain the highest  $\chi \approx 5.25[\epsilon/(1 \text{ GeV})][P/(1 \text{ PW})]^{1/2}[(1 \text{ }\mu\text{m})/\lambda]$  for a given electron energy  $\epsilon$ , laser power  $P$ , and wavelength  $\lambda$ . Reaching such a  $\chi$  with  $f/2$  focusing requires more than 10 times higher power.

DOI: [10.1103/PhysRevA.106.063512](https://doi.org/10.1103/PhysRevA.106.063512)**I. INTRODUCTION**

High-intensity laser facilities [1–5] in combination with conventional or laser-based electron accelerators open up opportunities to study extreme regimes of radiation reaction (RR) and of other effects due to strong-field quantum electrodynamics (SFQED) [6–8]. The effect of laser-generated electromagnetic fields on an electron is characterized by the dimensionless acceleration in its rest frame  $\chi = \gamma E_{\text{cr}}^{-1} \{[\mathbf{E} + (\mathbf{v}/c) \times \mathbf{B}]^2 - (\mathbf{E} \cdot \mathbf{v}/c)^2\}^{1/2}$ , where  $\mathbf{v}$  and  $\gamma$  are the electron velocity and gamma factor,  $c$  is the speed of light, and  $\mathbf{E}$  and  $\mathbf{B}$  are the electric- and magnetic-field vectors. The critical field of QED is defined as  $E_{\text{cr}} = m^2 c^3 / e \hbar$ , where  $\hbar$  is the reduced Planck constant and  $m$  and  $e$  are the electron mass and charge. The experimental objectives range from testing existing predictions at  $\chi \gtrsim 1$ , which designates the quantum regime of RR, to the detection of early signs of unknown behavior at  $\chi \gtrsim 1600$ , which demarcates qualitatively unexplored regimes characterized by the conjectured breakdown of perturbative nonlinear QED [9–11].

In the 1990s the collision of 46.6-GeV electrons with focused laser pulses was used to observe multiphoton Compton scattering [12] and multiphoton Breit-Wheeler pair creation [13]. Revisiting this experimental configuration with extended experimental program is a matter of several initiatives, including the E320 collaboration at FACET-II [14] and the LUXE collaboration at the European XFEL [15]. Another experimental alternative is based on the replacement of conventional acceleration by laser wake-field acceleration (LWFA). In recent experiments, signatures of RR at  $\chi \sim 0.1$  have been observed by colliding LWFA electrons with a laser pulse focused by an  $f/2$  parabolic mirror [16,17]. For further studies at higher  $\chi$ , apart from increasing electron energy and laser

power, it is natural to consider how large an increase of  $\chi$  we can get from more advanced focusing.

It is reasonable to think that this question has little practical meaning because a smaller strong-field region formed by tighter focusing implies an enhanced role of the shot-to-shot variation of the impact parameter, which is present due to limited capabilities for laser–electron-beam alignment. In addition,  $4\pi$  focusing may require unprecedentedly large parabolic mirrors, while reaching strong fields itself may require low vacuum [18] to prevent early cascade development [19]. Finally, it is unclear how to distinguish the signal of SFQED at high  $\chi$  from the dominating signal of emissions at low  $\chi$ .

In this paper we consider the problem of detecting and measuring the evidences of SFQED predictions that has not yet been experimentally verified. Specifically, we elaborate a strategy to reveal such evidences without accessing the regimes when these phenomena become prominent and significantly change the interaction physics. This is done under the assumption that the influence of these phenomena on the interaction process gradually rises with  $\chi$ . In this case high accuracy of measurements and/or statistical analysis can be used to infer the sought signal from experiments with a  $\chi$  value well below than that needed for the prominent change of physics. One example of a possible objective is to detect the effective mass change discussed in Ref. [14].

As the main result of the paper, we propose a way to extract the signal of SFQED events occurring at high  $\chi$  and for electrons having known initial energy such that high localization of the strong-field region is no longer an obstacle. Assuming this possibility, we determine the optimal focusing geometry, which we call a bidipole wave, and identify prospects and limitations of the proposed concept.

**II. SIGNAL DISTINGUISHING**

Since emissions probabilistically happen at unknown field strength and  $\gamma$  (in the case of prior emissions), it is not possible to do a direct measurement of the SFQED emission rate as a function of  $\chi$ , fractional photon energy  $\hbar\omega/mc^2\gamma$ , and other

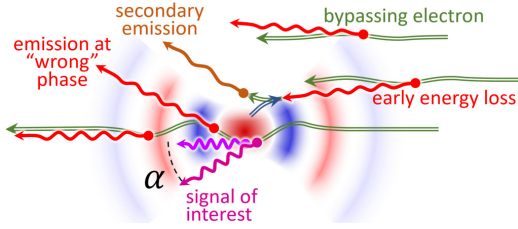


FIG. 1. Schematic illustration of interaction scenarios for various electrons passing through a tightly focused laser pulse.

parameters of interest. Instead, we have to make inferences by comparing experimental and numerical results for some measurable quantities or distributions that notably depend on this rate but preferably independent of unmeasurable shot-to-shot variations. The influence of the impact parameter becomes largely eliminated if the electron bunch is underfocused or diverged such that tight laser focusing occurs somewhere within a nearly uniform flux of electrons. Despite yielding a smaller number of emissions in the strong-field region, we choose this layout because it corresponds to data accumulation from repeated experiments and, more importantly, permits reaching higher  $\chi$  by arbitrary tight focusing. An explicit signal of the high- $\chi$  SFQED rate is carried by electrons that have emitted a single photon at about maximal  $\chi$ . Unfortunately, at the detector these electrons can hardly be distinguished from the majority of those bypassing the strong-field region, emitting multiple photons and/or at low  $\chi$ , and those being generated by the Breit-Wheeler process (see Fig. 1). However, a fortunate opportunity to distinguish an informative signal occurs for photons based on their energy and deviation angle  $\alpha$ , the angle between propagation directions of a photon and initial electrons. First, among electrons having initial energy only the ones passing through the strong-field region have the chance to emit photons with large  $\alpha \sim a_{\max}/\gamma$ , where  $a_{\max}$  is the peak field amplitude in units of  $m c \omega_0 / e$ , with  $\omega_0$  the laser frequency. Note that  $\alpha$  is required to be measurable but can still be assumed small due to large  $\gamma$  so that electrons deviate by a distance negligible as compared to the wavelength  $\lambda$  (in Fig. 1 the deviation is exaggerated for illustrative purposes). Second, the higher the energy of a detected photon the less likely it was emitted after another emission or by a newly generated particle. It is clear that among photons with large energy and  $\alpha$  we can expect a large part of those carrying the signal. As we show further, this makes possible reaching a given confidence level of statistical inferences with the number of shots many orders of magnitude smaller than that required in the case of electron-based diagnostics. Finally, note that Fig. 1 shows an unfavorable phase dependence  $\alpha = 0$  when the field peaks and vice versa. Using circular polarization (CP) makes  $\alpha$  and  $\chi$  correlated (see the insert on Fig. 2 and also Fig. 3), permitting direct measurements of the rate as a function of  $\chi$ .

### III. OPTIMAL FOCUSING

The possibility of creating the strongest field for a given power  $P$  by the dipole wave [20–22] using multiple colliding laser pulses [23] has been recognized to enable many possi-

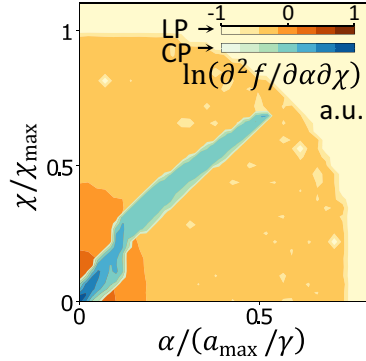


FIG. 2. Relative time that the electrons spend with various  $\alpha$  and  $\chi$  while passing through the bidipole wave for the CP and LP cases shown in Fig. 3.

bilities, ranging from particle trapping and photon generation [18,24–26] to the creation of sustained electromagnetic cascades and extreme electron-positron plasma states [27,28]. Nevertheless, the problem of maximizing  $\chi$  for a given power has received little attention in the literature. In Ref. [29] the analysis was restricted to the case of several beams focused to a point from the directions laying in a single plane. Here we consider the general case.

To quantify the role of focusing we note that in the focal region the intensity is proportional to  $P$  and inversely proportional to the focal area being proportional to  $\lambda^2$ . Therefore, the field strength scales proportionally to  $\lambda^{-1} P^{1/2}$  and  $\chi \propto \gamma \lambda^{-1} P^{1/2}$ . Thus, a focusing geometry can be quantified by a single dimensionless parameter  $\kappa$  that determines the peak  $\chi$  value (we assume that  $|\mathbf{v}| \approx c$  and  $\gamma \gg a_{\max}$ ):

$$\chi_{\max} = \kappa \left( \frac{\varepsilon}{1 \text{ GeV}} \right) \left( \frac{P}{1 \text{ PW}} \right)^{1/2} \left( \frac{\lambda}{1 \mu\text{m}} \right)^{-1}. \quad (1)$$

The problem of maximizing  $\kappa$  belongs to the class of optimization problems in optics. Using multipole expansion, Bassett showed that the dipole component provides the highest possible energy density for a given  $P$  and this optimal component also provides the strongest field strength  $a_0 \approx 780 [P / (1 \text{ PW})]^{1/2}$  [20].

To determine the optimal geometry we assume that the maximal value of  $\chi$  is achieved at the origin of the spherical coordinate system  $(r, \theta, \phi)$  with the electric field pointing towards  $\theta = 0$ . Assuming that the incoming wave is monochromatic, the field can be expressed as the real part of  $\exp(-i\omega_0 t)$  multiplied by some complex field  $(\mathbf{E}^X, \mathbf{B}^X)$ , which in turn can be expressed using the basis of electric  $(\mathbf{E}^E, \mathbf{B}^E)$  and magnetic  $(\mathbf{E}^B, \mathbf{B}^B)$  multipoles (exact solutions of Maxwell's equations) given by [30]

$$\begin{aligned} E_r^E &= l(l+1)r^{-1}j_l(kr)Y_l^m(\theta, \phi), \\ E_\theta^E &= r^{-1}\partial_r[rj_l(kr)]\partial_\theta Y_l^m(\theta, \phi), \\ E_\phi^E &= im \sin^{-1}\theta r^{-1}\partial_r[rj_l(kr)]Y_l^m(\theta, \phi), \end{aligned}$$

$$\begin{aligned}
 \mathbf{B}_r^E &= 0, & \mathbf{B}_\theta^E &= km \sin^{-1} \theta j_l(kr) Y_l^m(\theta, \phi), \\
 \mathbf{B}_\phi^E &= ik j_l(kr) \partial_\theta [Y_l^m(\theta, \phi)], \\
 \mathbf{E}^B &= -\mathbf{B}^E, & \mathbf{B}^B &= \mathbf{E}^E,
 \end{aligned} \quad (2)$$

where  $l = 1, 2, 3, \dots, m = -l, -l + 1, \dots, l, k = \omega_0/c$ , and  $j_l(kr)$  and  $Y_l^m(\theta, \phi)$  are spherical Bessel functions and spherical harmonics, respectively. The subscripts denote vector components along the unit vectors.

Bassett showed that in terms of incoming power the multipolar components are additive, i.e., for any combination of them, the incoming power is the sum of incoming powers of the components (see Sec. 3 in Ref. [20]). Following Bassett, we consider the limit  $r \rightarrow 0$  and note that only six components contribute to the field at  $r = 0$  ( $\mathbf{E}$  is formed by  $\mathbf{E}_{l,m}^E$  and  $\mathbf{B}$  is formed by  $\mathbf{B}_{l,m}^B$ , in both cases  $l = 1$  and  $m = -1, 0, 1$ ),

$$\mathbf{E}_{1,-1}^E = \mathbf{B}_{1,-1}^B = k(6\pi)^{-1/2}(\hat{\mathbf{x}} - i\hat{\mathbf{y}}), \quad (3)$$

$$\mathbf{E}_{1,0}^E = \mathbf{B}_{1,0}^B = k(3\pi)^{-1/2}\hat{\mathbf{z}}, \quad (4)$$

$$\mathbf{E}_{1,1}^E = \mathbf{B}_{1,1}^B = -k(6\pi)^{-1/2}(\hat{\mathbf{x}} + i\hat{\mathbf{y}}), \quad (5)$$

where  $\hat{\mathbf{x}}$ ,  $\hat{\mathbf{y}}$ , and  $\hat{\mathbf{z}}$  are the Cartesian system unit vectors pointing towards  $(\theta = \pi/2, \phi = 0)$ ,  $(\theta = \pi/2, \phi = \pi/2)$ , and  $(\theta = 0)$ , respectively. According to our assumption,  $\mathbf{E}^\chi$  is pointing towards  $\theta = 0$  and thus it is formed exclusively by the component  $\mathbf{E}_{1,0}^E$ . Without loss of generality, we can assume that the coordinate system is oriented so that  $\mathbf{B}^\chi(r = 0)$  is laying in the  $xz$  plane and thus it is formed by a combination of  $\mathbf{B}_{1,0}^B$  and  $2^{1/2}(\mathbf{B}_{1,-1}^B - \mathbf{B}_{1,1}^B)$  components (the factor is chosen to provide synchronous peaking). The components  $\mathbf{E}_{1,0}^E$  and  $\mathbf{B}_{1,0}^B$  correspond to the electric and magnetic dipole waves with symmetry axis along  $\hat{\mathbf{z}}$ , whereas  $2^{1/2}(\mathbf{B}_{1,-1}^B - \mathbf{B}_{1,1}^B)$  corresponds to the magnetic dipole wave with symmetry axis along  $\hat{\mathbf{x}}$ . Given that the power of components is additive, we can describe all cases by splitting the total power  $P$  into three portions:  $aP$  is delivered by the electric dipole wave, whereas the portions  $bP$  and  $(1 - a - b)P$  are delivered by the magnetic dipole waves with symmetry axes along  $\hat{\mathbf{z}}$  and  $\hat{\mathbf{x}}$ , respectively;  $0 \leq a, b \leq 1$ , and  $a + b \leq 1$ . The strength of components in relativistic units is given by

$$\mathbf{E} = a_d [P/(1 \text{ PW})]^{1/2} a^{1/2} \hat{\mathbf{z}}, \quad (6)$$

$$\mathbf{B} = a_d [P/(1 \text{ PW})]^{1/2} [b^{1/2} \hat{\mathbf{z}} + (1 - a - b)^{1/2} \hat{\mathbf{x}}], \quad (7)$$

where  $a_d \approx 780$ . If we were interested in the maximal energy density  $[(E^2 + B^2)/8\pi]$  all the cases were indifferent because the energy density is independent of  $a$  and  $b$ . Nevertheless, searching for the strongest possible acceleration yields one specific optimum. First we note that the maximal Lorentz force is achieved if the electron propagates along the  $y$  axis. In this case the absolute value of the Lorentz force and the  $\chi$  value is proportional to

$$\chi \propto \{[a^{1/2} + (1 - a - b)^{1/2}]^2 + b\}^{1/2}. \quad (8)$$

Searching for the maximum of  $\chi^2$ , we first notice that  $\partial\chi^2/\partial b \leq 0$  for all  $a$  and  $b$ , meaning that the maximum is achieved at  $b = 0$ . Next we compute  $\partial\chi^2/\partial a$  and determine that the maximum is achieved at  $a = \frac{1}{2}$ .

As one can see, the maximum corresponds to the equal destitution of energy between electric and magnetic dipole waves that have perpendicular axes. That is why we choose to call this geometry a bidipole wave. The field strength is  $|\mathbf{E}^\chi| = |\mathbf{B}^\chi| = a_{\max} = a_d [P/(1 \text{ PW})]^{1/2} / \sqrt{2} \approx 550 [P/(1 \text{ PW})]^{1/2}$  (in relativistic units) and the value of  $\kappa$  is approximately 5.25.

So far we have been considering monochromatic radiation. Lifting this limitation, i.e., considering the electromagnetic pulse shape as another matter of optimization, yields an ill-posed maximization problem: Higher frequency gives smaller focal volume and thereby higher field strength for the same power, which means that  $\chi$  is unbound from above in the case of an unrestricted spectrum. This is also manifested by the  $\chi_{\max}$  dependence on the wavelength shown in Eq. (1). Nevertheless, a fortunate possibility to assess practically important pulsed solutions is provided by the theory of dipole pulses developed in Ref. [21]. Since the bidipole wave is a sum of two dipole waves, we can generalize our result and define a bidipole pulse as a sum of two dipole pulses (one electric and one magnetic, both synchronized in time, with perpendicular axes of symmetry). For example, using this we can answer one, probably quite practical, question: What benefit can we get from the shortness of a focused Gaussian-like pulse? Using the theory of dipole pulses, we obtain that the relative increase of  $\chi$  is  $3 \ln 2 \tau_0^{-2} / \pi^2$ , where  $\tau_0$  is the pulse duration in cycles, determined according to the full width at half maximum for the intensity. Practically this means that the benefit is moderate: Even for a two-cycle pulse it is about 5%, while for common Ti:sapphire pulses (approximately five cycles) it is less than 1%.

#### IV. BIDIPOLE WAVE STRUCTURE

We continue by considering the structure of the bidipole wave and the way to generate it in practice. To within a constant factor, the electric-field vector in the far-field region can be given by

$$\mathbf{E}(r \rightarrow \infty) \propto r^{-1}(\mathbf{E}^e + \mathbf{E}^b), \quad (9)$$

$$\mathbf{E}^e = (\hat{\mathbf{z}} \times \mathbf{n}) \times \mathbf{n}, \quad \mathbf{E}^b = (\hat{\mathbf{x}} \times \mathbf{n}), \quad (10)$$

where  $\mathbf{n} = \mathbf{r}/r$ , whereas  $\mathbf{E}^e$  and  $\mathbf{E}^b$  are proportional to the electric-field vectors of the radiation forming electric and magnetic dipole waves, respectively. The signs are chosen so that the constructive summation of the electric and magnetic components is provided for a charge propagating towards the negative  $y$  direction.

Along each direction the dipole waves are formed by linearly polarized, in-phase waves and thus the bidipole wave is also formed by linearly polarized wave. Let us demonstrate that the distribution of intensity  $I$  of this wave is symmetric about the  $y$  axis. To do so we compute the intensity as a function of  $\mathbf{n}$ :

$$\mathbf{E}^e = n_x n_z \hat{\mathbf{x}} - (n_x^2 + n_y^2) \hat{\mathbf{z}} + n_y n_z \hat{\mathbf{y}}, \quad \mathbf{E}^b = n_y \hat{\mathbf{z}} - n_z \hat{\mathbf{y}},$$

$$I \propto |\mathbf{E}^e + \mathbf{E}^b|^2 = n_x^2 n_z^2 + (n_x^2 + n_y^2 - n_y)^2 + n_z^2 (n_y - 1)^2.$$

To demonstrate the axial symmetry of  $I$  we introduce a spherical coordinate system  $(\theta_y, \varphi)$  so that the unit vector has the

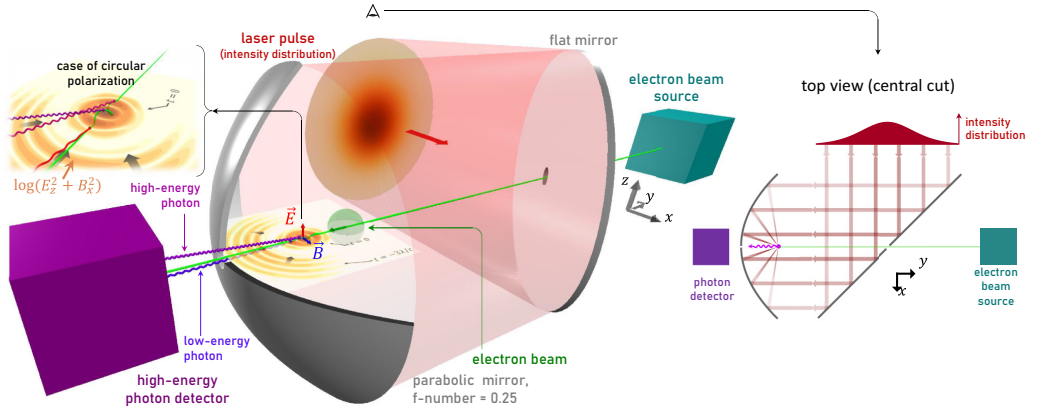


FIG. 3. Schematic representation of a possible experimental setup. The inset shows the case of circular polarization (deviation angles are exaggerated).

components

$$\begin{aligned} n_y &= \cos \theta_y, & n_x &= \sin \theta_y \cos \varphi, \\ n_z &= \sin \theta_y \sin \varphi. \end{aligned}$$

Given that  $\partial n_y / \partial \varphi = 0$ ,  $\partial n_x / \partial \varphi = -n_z$ , and  $\partial n_z / \partial \varphi = n_x$ , we can compute

$$\frac{\partial I}{\partial \varphi} \propto 2n_z n_x (1 - n_z^2 - n_y^2 - n_x^2) = 0, \quad (11)$$

which proves the axial symmetry.

If  $\varphi = 0$  is chosen such that  $\cos(\varphi) = 1$  and  $\sin(\varphi) = 0$ , then in the expression for  $I$  only the middle term remains and

$$I \propto (1 - \cos \theta_y)^2 / r^2. \quad (12)$$

As we can see, the radiation arrives predominantly from the negative  $y$  hemisphere.

One possible way to form the bidipole wave is the reflection of an appropriate laser beam propagating towards the negative  $y$  direction from a parabolic mirror. Let us compute the polarization and intensity distribution in such a beam. During reflection the electric-field component along the normal  $\mathbf{N}$  to the mirror is reversed. Thus, to within a factor the electric field before reflection is given by  $\mathbf{E}^p = \mathbf{E} - 2(\mathbf{E} \cdot \mathbf{N})\mathbf{N}$ , where the normal can be expressed as  $\mathbf{N} = (\hat{\mathbf{y}} - \mathbf{n})/|\hat{\mathbf{y}} - \mathbf{n}|$ . We note that  $(\mathbf{E} \cdot \mathbf{N}) = n_z(n_y - 1)/|\hat{\mathbf{y}} - \mathbf{n}|$  and compute the  $x$  component of  $\mathbf{E}^p$ :

$$\begin{aligned} E_x^p &= n_x n_z - 2n_z(n_y - 1)(-n_x)[n_x^2 + n_z^2 + (n_y - 1)^2]^{-1} \\ &= n_x n_z + 2n_z(n_y - 1)n_x[n_x^2 + n_z^2 + (n_y - 1)^2]^{-1} \\ &= 0. \end{aligned}$$

As we can see, the beam to be reflected has linear polarization exactly along the  $z$  axis everywhere. Due to such a fortunate property, this configuration has been considered by Sheppard and Larkin [31] as a notably practical option among all mixed dipole waves that yield the highest electromagnetic-field density under focusing of a given power. As we demonstrated, exactly this option also gives the highest value of  $\chi$ . Using

Eq. (12), we can compute the intensity at the mirror and, using local  $\mathbf{N}$ , the intensity distribution in the beam to be reflected,

$$I^p(R) \propto [(R/2L)^2 + 1]^{-4}, \quad (13)$$

where  $L$  is the distance to the mirror and  $R$  is the distance to the  $z$  axis in the transverse plane. The resultant scheme of potential experiments is illustrated in Fig. 3.

The infinite parabolic mirror that forms the bidipole wave by reflecting an intensity-shaped beam has to be limited in practice. To facilitate more practical consideration of the use of bidipole wave in experiments, we consider how the peak value of  $\chi$  depends on the parabolic mirror radius  $R_{\max}$ . The limitation  $R < R_{\max}$  can be expressed via the f-number equal to  $L/2R_{\max}$  or via the opening angle  $\zeta = \pi/2 + \arctan(R_{\max}/4L - L/R_{\max})$  of the cone that encompasses the

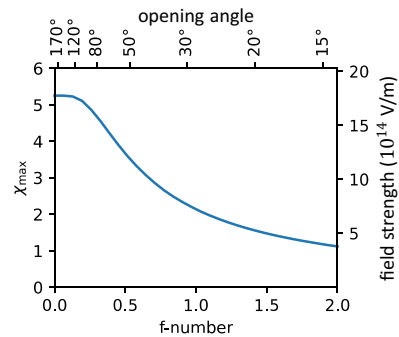


FIG. 4. Dependence of  $\chi_{\max}$  on the f-number that characterizes the radius of the parabolic mirror shown in Fig. 3. The top axis shows the corresponding values of the opening angle. The shown values are numerically obtained for  $P = 1$  PW,  $\varepsilon = 1$  GeV, and  $\lambda = 1$   $\mu\text{m}$ , whereas the values for other cases can be obtained using scaling  $\chi_{\max} \propto \varepsilon \lambda^{-1} P^{1/2}$ . The axis on the right shows the corresponding peak values of the electric- or magnetic-field strength that scales proportionally to  $\lambda^{-1} P^{1/2}$ .



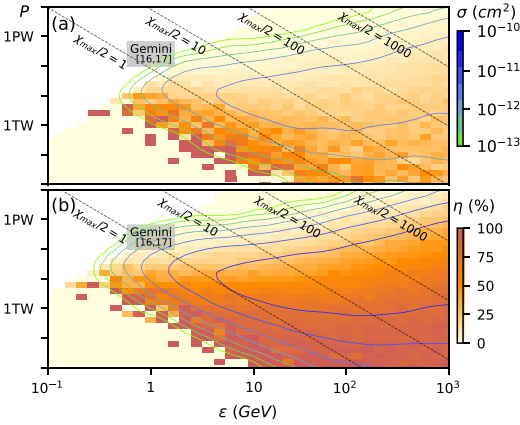


FIG. 5. Effective cross section  $\sigma$  and signal ratio  $\eta$  computed numerically for (a) linear and (b) circular polarization.

rays coming to the focus. In Fig. 4 we show numerically computed peak value  $\chi_{\max}$  as a function of the f-number. We assume the shape given by Eq. (13) with restriction  $R < R_{\max}$  and keep the total incoming power  $P = 1$  PW in all cases. We assume that  $\epsilon = 1$  GeV and  $\lambda = 1$   $\mu\text{m}$ , whereas the values for other cases can be obtained using scaling  $\chi_{\max} \propto \epsilon \lambda^{-1} P^{1/2}$ . The right axis shows the corresponding peak values of the electric- or magnetic-field strength that scales proportionally to  $\lambda^{-1} P^{1/2}$ .

## V. NUMERICAL ANALYSIS

Having determined the optimal focusing, we can assess the concept capabilities, which we characterize by a signal ratio  $\eta = N_{\text{signal}}/N_{\text{total}}$  and an effective cross section  $\sigma$ . Here  $N_{\text{total}}$  is the number of photons detected with  $\alpha > 0.6a_{\max}/\gamma$  and  $\hbar\omega > mc^2\gamma/2$ , whereas among them  $N_{\text{signal}}$  photons are emitted at  $\chi > \chi_{\max}/2$  and by electrons that had not lost more than 1% of the initial energy prior to the emission. The cross section is defined as  $\sigma = N_{\text{signal}}/n_e\tau_I c$ , where  $n_e$  is the density of streaming electrons and  $\tau_I$  is the laser pulse duration. In Fig. 5 we demonstrate the results of simulations for various  $P$  and  $\epsilon$  values that can be relevant to current and upcoming experimental capabilities. We consider a laser pulse that has a Gaussian profile with a duration of five cycles (FWHM for intensity):  $\lambda = 0.8$   $\mu\text{m}$ . In the case of CP the peak amplitude is  $a_{\max}^{\text{CP}} = a_{\max}/\sqrt{2}$  and we use a modified selection rule  $\alpha > 0.7a_{\max}^{\text{CP}}/\gamma$ .

To exemplify the results, let us estimate the number of shots needed to reach 3- $\sigma$  confidence level for detecting a 1% deviation of the rate at  $\chi > 10$ . Assuming current progress on LWFA [32], we consider a 10-GeV electron bunch of total charge 100 pC ( $6 \times 10^8$  electrons) that is spread over a spherical volume with 5  $\mu\text{m}$  diameter so that  $n_e \approx 10^{19}$  cm<sup>-3</sup>. Using  $N$  shots and cumulative  $N_{\text{total}}$  as a test statistic means that  $3\sigma_N \leq 0.01N_{\text{signal}}$ , where the variance of  $N_{\text{total}}$  is  $\sigma_N^2 \approx N_{\text{total}}$ . From Fig. 5 we see that for  $\epsilon = 10$  GeV the value  $\chi_{\max}/2 = 10$  is achieved at  $P \approx 100$  TW with  $\sigma \sim 10^{-11}$  cm<sup>2</sup> and  $\eta \sim 0.1$ . Substituting these values, we estimate that we have approximately  $5 \times 10^4$  photons per shot, while we need approximately  $(3/0.01\eta)^2 \approx 10^7$  photons and thus  $N \sim 200$  shots ( $N \propto 1/\sigma\eta^2$ ).

Let us compare this to the number of shots required in the case of using electron energy loss for the test statistic. Assuming the best case scenario, we consider all the electrons passing through a five-cycle laser pulse with  $a_{\max} \approx 200$  to reach  $\chi = 10$ . At  $\chi \sim 10$  the mean free path is approximately equal to  $15\lambda\chi^{1/3}/a_{\max} \approx 0.15\lambda$  [7] and electrons need to propagate about  $2\lambda$  to reach  $\chi = 10$ . Thus, only a fraction  $\eta \sim \exp(-2/0.15) \approx 10^{-6}$  of initial electrons can keep high  $\gamma$  to be affected by the deviation at  $\chi > 10$ . This means that we need cumulatively  $(3/0.01\eta)^2 \approx 10^{17}$  electrons and having  $6 \times 10^8$  electrons per shot, this requires approximately  $10^8$  shots.

## VI. CONCLUSION

We have shown that for laser-electron colliders the energy and deviation angle of emitted photons can be used to attain the characteristics of high- $\chi$  SFQED rates despite the background of low- $\chi$  emissions. This permits using tight focusing to boost  $\chi$  values, for which we determined the limit given by the so-called bidipole wave. The concept prospects were characterized by the effective cross section and signal ratio, indicating that PW–10-GeV–class facilities can study  $\chi \sim 10$ –100, while  $\chi \sim 10^3$  requires higher energy and/or power in combination with cascade suppression. The latter encourages further studies on electron injection [26,33] as well as on the use of shorter pulses [34] or pulse steepening [35–39].

## ACKNOWLEDGMENTS

The authors acknowledge support from the Swedish Research Council (Grants No. 2017-05148 and No. 2019-02376) and computational resources provided by the Swedish National Infrastructure for Computing.

- [1] ELI whitebook, <https://eli-laser.eu/media/1019/eli-whitebook.pdf>.
- [2] XCELS whitebook, <https://xcel.s.ipfran.ru/img/XCELS-Project-english-version.pdf>.
- [3] Y. Kitagawa, H. Fujita, R. Kodama, H. Yoshida, S. Matsuo, T. Jitsuno, T. Kawasaki, H. Kitamura, T. Kanabe, S. Sakabe, K. Shigemori, N. Miyanaga, and Y. Izawa, Prepulse-free petawatt

laser for a fast ignitor, *IEEE J. Quantum Electron.* **40**, 281 (2004).

- [4] J. Kawanaka, K. Tsubakimoto, H. Yoshida, K. Fujioka, Y. Fujimoto, S. Tokita, T. Jitsuno, N. Miyanaga, and Gekko-EXA Design Team, Conceptual design of sub-exa-watt system by using optical parametric chirped pulse amplification, *J. Phys.: Conf. Ser.* **688**, 012044 (2016).

- [5] C. N. Danson, C. Haefner, J. Bromage, T. Butcher, J.-C. F. Chanteloup, E. A. Chowdhury, A. Galvanauskas, L. A. Gizzi, J. Hein, D. I. Hillier, N. W. Hopps, Y. Kato, E. A. Khazanov, R. Kodama, G. Korn, R. Li, Y. Li, J. Limpert, J. Ma, C. H. Nam *et al.*, Petawatt and exawatt class lasers worldwide, *High Power Laser Sci. Eng.* **7**, e54 (2019).
- [6] A. Di Piazza, C. Muller, K. Z. Hatsagortsyan, and C. H. Keitel, Extremely high-intensity laser interactions with fundamental quantum systems, *Rev. Mod. Phys.* **84**, 1177 (2012).
- [7] A. Gonoskov, T. G. Blackburn, M. Marklund, and S. S. Bulanov, Charged particle motion and radiation in strong electromagnetic fields, *Rev. Mod. Phys.* **94**, 045001 (2022).
- [8] A. Fedotov, A. Ilderton, F. Karbstein, B. King, D. Seipt, H. Taya, and G. Torgrimsson, Advances in QED with intense background fields, [arXiv:2203.00019](https://arxiv.org/abs/2203.00019).
- [9] V. Ritus, Radiative corrections in quantum electrodynamics with intense field and their analytical properties, *Ann. Phys. (NY)* **69**, 555 (1972).
- [10] N. B. Narozhny, Expansion parameter of perturbation theory in intense-field quantum electrodynamics, *Phys. Rev. D* **21**, 1176 (1980).
- [11] A. Fedotov, Conjecture of perturbative QED breakdown at  $\alpha\chi^{2/3} \gtrsim 1$ , *J. Phys.: Conf. Ser.* **826**, 012027 (2017).
- [12] C. Bula, K. T. McDonald, E. J. Prebys, C. Bamber, S. Boege, T. Kotseroglou, A. C. Melissinos, D. D. Meyerhofer, W. Ragg, D. L. Burke, R. C. Field, G. Horton-Smith, A. C. Odian, J. E. Spencer, D. Walz, S. C. Berridge, W. M. Bugg, K. Shmakov, and A. W. Weidemann, Observation of Nonlinear Effects in Compton Scattering, *Phys. Rev. Lett.* **76**, 3116 (1996).
- [13] D. L. Burke, R. C. Field, G. Horton-Smith, J. E. Spencer, D. Walz, S. C. Berridge, W. M. Bugg, K. Shmakov, A. W. Weidemann, C. Bula, K. T. McDonald, E. J. Prebys, C. Bamber, S. J. Boege, T. Koffas, T. Kotseroglou, A. C. Melissinos, D. D. Meyerhofer, D. A. Reis, and W. Ragg, Positron Production in Multiphoton Light-by-Light Scattering, *Phys. Rev. Lett.* **79**, 1626 (1997).
- [14] V. Yakimenko, L. Alsberg, E. Bong, G. Bouchard, C. Clarke, C. Emma, S. Green, C. Hast, M. J. Hogan, J. Seabury, N. Lipkowitz, B. O'Shea, D. Storey, G. White, and G. Yocky, FACET-II facility for advanced accelerator experimental tests, *Phys. Rev. Accel. Beams* **22**, 101301 (2019).
- [15] H. Abramowicz, M. Altarelli, R. Aßmann, T. Behnke, Y. Benhammou, O. Borysov, M. Borysova, R. Brinkmann, F. Burkart, K. Büber, O. Davidi, W. Decking, N. Elkina, H. Harsh, A. Hartin, I. Hartl, B. Heinemann, T. Heinzl, N. Tal Hod, M. Hoffmann *et al.* (unpublished).
- [16] J. M. Cole, K. T. Behm, E. Gerstmayr, T. G. Blackburn, J. C. Wood, C. D. Baird, M. J. Duff, C. Harvey, A. Ilderton, A. S. Joglekar, K. Krushelnick, S. Kuschel, M. Marklund, P. McKenna, C. D. Murphy, K. Poder, C. P. Ridgers, G. M. Samarin, G. Sarri, D. R. Symes *et al.*, Experimental Evidence of Radiation Reaction in the Collision of a High-Intensity Laser Pulse with a Laser-Wakefield Accelerated Electron Beam, *Phys. Rev. X* **8**, 011020 (2018).
- [17] K. Poder, M. Tamburini, G. Sarri, A. Di Piazza, S. Kuschel, C. D. Baird, K. Behm, S. Bohlén, J. M. Cole, D. J. Corvan, M. Duff, E. Gerstmayr, C. H. Keitel, K. Krushelnick, S. P. D. Mangles, P. McKenna, C. D. Murphy, Z. Najmudin, C. P. Ridgers, G. M. Samarin *et al.*, Experimental Signatures of the Quantum Nature of Radiation Reaction in the Field of an Ultraintense Laser, *Phys. Rev. X* **8**, 031004 (2018).
- [18] A. Gonoskov, A. Bashinov, I. Gonoskov, C. Harvey, A. Ilderton, A. Kim, M. Marklund, G. Mourou, and A. Sergeev, Anomalous Radiative Trapping in Laser Fields of Extreme Intensity, *Phys. Rev. Lett.* **113**, 014801 (2014).
- [19] S. S. Bulanov, T. Z. Esirkepov, A. G. R. Thomas, J. K. Koga, and S. V. Bulanov, Schwinger Limit Attainability with Extreme Power Lasers, *Phys. Rev. Lett.* **105**, 220407 (2010).
- [20] I. M. Bassett, Limit to concentration by focusing, *Opt. Acta* **33**, 279 (1986).
- [21] I. Gonoskov, A. Aiello, S. Heugel, and G. Leuchs, Dipole pulse theory: Maximizing the field amplitude from  $4\pi$  focused laser pulses, *Phys. Rev. A* **86**, 053836 (2012).
- [22] T. M. Jeong, S. V. Bulanov, P. V. Sasorov, S. S. Bulanov, J. K. Koga, and G. Korn,  $4\pi$ -spherically focused electromagnetic wave: Diffraction optics approach and high-power limits, *Opt. Express* **28**, 13991 (2020).
- [23] S. S. Bulanov, V. D. Mur, N. B. Narozhny, J. Nees, and V. S. Popov, Multiple Colliding Electromagnetic Pulses: A Way to Lower the Threshold of  $e^+e^-$  Pair Production from Vacuum, *Phys. Rev. Lett.* **104**, 220404 (2010).
- [24] A. Gonoskov, A. Bashinov, S. Bastrakov, E. Efimenko, A. Ilderton, A. Kim, M. Marklund, I. Meyerov, A. Muraviev, and A. Sergeev, Ultrabright GeV Photon Source via Controlled Electromagnetic Cascades in Laser-Dipole Waves, *Phys. Rev. X* **7**, 041003 (2017).
- [25] J. Magnusson, A. Gonoskov, M. Marklund, T. Z. Esirkepov, J. K. Koga, K. Kondo, M. Kando, S. V. Bulanov, G. Korn, C. G. R. Geddes, C. B. Schroeder, E. Esarey, and S. S. Bulanov, Multiple colliding laser pulses as a basis for studying high-field high-energy physics, *Phys. Rev. A* **100**, 063404 (2019).
- [26] J. Magnusson, A. Gonoskov, M. Marklund, T. J. Esirkepov, J. Koga, K. Kondo, M. Kando, S. Bulanov, G. Korn, and S. S. Bulanov, Laser-Particle Collider for Multi-GeV Photon Production, *Phys. Rev. Lett.* **122**, 254801 (2019).
- [27] E. S. Efimenko, A. V. Bashinov, A. A. Gonoskov, S. I. Bastrakov, A. A. Muraviev, I. B. Meyerov, A. V. Kim, and A. M. Sergeev, Laser-driven plasma pinching in  $e^-e^+$  cascade, *Phys. Rev. E* **99**, 031201(R) (2019).
- [28] E. S. Efimenko, A. V. Bashinov, S. I. Bastrakov, A. A. Gonoskov, A. A. Muraviev, I. B. Meyerov, A. V. Kim, and A. M. Sergeev, Extreme plasma states in laser-governed vacuum breakdown, *Sci. Rep.* **8**, 2329 (2018).
- [29] E. G. Gelfer, A. A. Mironov, A. M. Fedotov, V. F. Bashmakov, E. N. Nerush, I. Y. Kostyukov, and N. B. Narozhny, Optimized multibeam configuration for observation of QED cascades, *Phys. Rev. A* **92**, 022113 (2015).
- [30] W. Panofsky, *Classical Electricity and Magnetism* (Dover, Mineola, 2005).
- [31] C. Sheppard and K. Larkin, Optimal concentration of electromagnetic radiation, *J. Mod. Opt.* **41**, 1495 (1994).
- [32] A. J. Gonsalves, K. Nakamura, J. Daniels, C. Benedetti, C. Pieronek, T. C. H. de Raadt, S. Steinke, J. Bin, S. Bulanov, J. van Tilborg, C. G. R. Geddes, C. B. Schroeder, C. Tóth, E. Esarey, K. Swanson, L. Fan-Chiang, G. Bagdasarov, N. Bobrova, V. Gasilov, G. Korn *et al.*, Petawatt Laser Guiding and Electron Beam Acceleration to 8 GeV in a Laser-Heated

- Capillary Discharge Waveguide, *Phys. Rev. Lett.* **122**, 084801 (2019).
- [33] T. G. Blackburn, A. Ilderton, M. Marklund, and C. P. Ridgers, Reaching supercritical field strengths with intense lasers, *New J. Phys.* **21**, 053040 (2019).
- [34] D. E. Rivas, A. Borot, D. E. Cardenas, G. Marcus, X. Gu, D. Herrmann, J. Xu, J. Tan, D. Kormin, G. Ma, W. Dallari, G. D. Tsakiris, I. B. Földes, S.-w. Chou, M. Weidman, B. Bergues, T. Wittmann, H. Schröder, P. Tzallas, D. Charalambidis, O. Razskazovskaya, V. Pervak, F. Krausz, and L. Veisz, Next generation driver for attosecond and laser-plasma physics, *Sci. Rep.* **7**, 5224 (2017).
- [35] T. K. Gustafson, J. P. Taran, H. A. Haus, J. R. Lifshitz, and P. L. Kelley, Self-modulation, self-steepening, and spectral development of light in small-scale trapped filaments, *Phys. Rev.* **177**, 306 (1969).
- [36] P. Kaw, Relativistic nonlinear propagation of laser beams in cold overdense plasmas, *Phys. Fluids* **13**, 472 (1970).
- [37] A. A. Gonoskov, A. V. Korzhimanov, V. I. Eremin, A. V. Kim, and A. M. Sergeev, Multicascade Proton Acceleration by a Superintense Laser Pulse in the Regime of Relativistically Induced Slab Transparency, *Phys. Rev. Lett.* **102**, 184801 (2009).
- [38] S. A. Reed, T. Matsuoka, S. Bulanov, M. Tampo, V. Chvykov, G. Kalintchenko, P. Rousseau, V. Yanovsky, R. Kodama, D. W. Litzenberg, K. Krushelnick, and A. Maksimchuk, Relativistic plasma shutter for ultraintense laser pulses, *Appl. Phys. Lett.* **94**, 201117 (2009).
- [39] H. Y. Wang, C. Lin, Z. M. Sheng, B. Liu, S. Zhao, Z. Y. Guo, Y. R. Lu, X. T. He, J. E. Chen, and X. Q. Yan, Laser Shaping of a Relativistic Intense, Short Gaussian Pulse by a Plasma Lens, *Phys. Rev. Lett.* **107**, 265002 (2011).



# Paper B

C. OLOFSSON AND A. GONOSKOV. "Prospects for statistical tests of strong-field quantum electrodynamics with high-intensity lasers". *arXiv preprint: arXiv:2303.00568*





# Prospects for statistical tests of strong-field quantum electrodynamics with high-intensity lasers

C. Olofsson\* and A. Gonoskov†

*Department of Physics, University of Gothenburg, SE-41296 Gothenburg, Sweden*

(Dated: March 2, 2023)

Exploiting high-energy electron beams colliding into high-intensity laser pulses brings an opportunity to reach high values of the dimensionless rest-frame acceleration  $\chi$  and thereby invoke processes described by strong-field quantum electrodynamics (SFQED). Measuring deviations from the results of perturbative SFQED at high  $\chi$  can be valuable for testing the existing predictions, as well as for guiding further theoretical developments. Nevertheless such experimental measurements are challenging due to the probabilistic nature of the interaction processes, a strong background produced by low- $\chi$  interactions and limited capabilities to control and measure the alignment and synchronization in such collision experiments. Here we elaborate a methodology of using approximate Bayesian computations (ABC) for retrieving statistically justified inferences based on the results of many repeated experiments even in case of partially unknown collision parameters that vary from experiment to experiment. As a proof of principles, we consider the problem of inferring the effective mass change due to coupling with strong-field environment.

## I. INTRODUCTION

Although fundamental principles of quantum electrodynamics (QED) are known for their precise experimental validations, the implications they purport for sufficiently strong electromagnetic fields remain theoretically intricate and lack experimental data. Colliding accelerated electrons with high-intensity laser pulses can be seen as a newly emerging pathway to such experimental data [1–4]. The local interaction is characterized by the dimensionless ratio of the electron acceleration in its rest frame to the acceleration that would be caused by the Schwinger field  $E_{\text{crit}}$ :

$$\chi = \frac{\gamma_e}{E_{\text{crit}}} \sqrt{\left(\vec{E} + (\vec{v}/c) \times \vec{B}\right)^2 - \left(\vec{E} \cdot \vec{v}/c\right)^2} \quad (1)$$

where  $\vec{v}$ ,  $\gamma_e$  are the velocity and Lorentz factor of the electron, whereas  $\vec{E}$ ,  $\vec{B}$  are the electromagnetic field vectors. Here,  $E_{\text{crit}} = m_e^2 c^3 / q_e \hbar \approx 10^{18} \text{ V m}^{-1}$  where  $\hbar$  is the reduced Planck constant,  $c$  is the speed of light and  $m_e$ ,  $q_e$  are the mass and charge of the electron respectively. At  $\chi \ll 1$  the electrons are subject to classical emission and corresponding radiation reaction. Emission of photons and corresponding recoils at  $\chi \sim 1$  are described by non-linear Compton scattering and have been experimentally observed in several experiments [5–8]. Measuring quantitative properties of the photon emission (e.g. energy, angular or polarization distribution) at  $\chi \sim 1$  can be perceived as a logical next step, while results for  $\chi \gg 1$  can potentially facilitate theoretical developments or even lead to fundamental discoveries (see Ref. [9] and references therein).

A severe obstacle for the outlined efforts is the interaction complexity. The value of  $\chi$  for each electron in the beam varies in time and overall depends on the electron position relative to the laser pulse location, which can also vary from experiment to experiment due to spatio-temporal mismatches. For contemporary laser pulse durations, many electrons can lose a significant part of their initial energy prior to reaching the strong-field region, where they have a chance to emit at high  $\chi$ . Additionally, due to the Breit-Wheeler process the emitted photons can decay into electron-positron pairs, which can lead to the onset of an electromagnetic cascade. In combination, this means that the measurable post-collision distributions of photons, electrons and positrons are predominantly determined by low- $\chi$  emissions, giving no direct information about emissions at high- $\chi$ , even if they had been invoked.

One known way of dealing with such difficulties is Bayesian binary hypothesis testing, which is based on comparing experimental results with the outcomes computed on the basis of each of two competing theories. However, even in the absence of a distinct hypothesis to be tested, one can use a similar technique to determine parameters that quantify deviations from the approximate theory (sometimes referred to as parameter calibration procedure [10–12]), which in our case can be the theory on non-linear Compton scattering valid for moderate  $\chi$  values. One practicality of this approach is the possibility to gain statistically rigorous knowledge from many experiments even in case of low repeatability. For example, the inference about high  $\chi$  events is feasible regardless if the alignment of the laser-beam setup varies uncontrollably between experiments which we cannot measure.

In this paper we consider the possibility of using the technique of approximate Bayesian computation (ABC) in the forthcoming experiments [10, 13, 14]. As a proof-

\* christoffer.olofsson@physics.gu.se

† arkady.gonoskov@physics.gu.se

of-principle problem we elaborate the use of this method for measuring the constant that quantifies the effective mass shift [9, 15–17]. We assess the use of the ABC technique in the context of possible experimental conditions and analyze main requirements, difficulties and opportunities for improvements. The paper is arranged as follows. In Sec. II we motivate the use of likelihood-free inference and state the ABC algorithm. In Sec. III we demonstrate a proof-of-principle approach to infer the effective mass change, assessing the difficulties and limitations. Sec. IV provides the numerical aspects in simulating the experiment and gives the prospects of the outlined methodology. We make conclusions in Sec. V.

## II. METHODOLOGY

Before turning to the subject-specific analysis, let us consider the methodology using a general problem formulation. Suppose we study a probabilistic process by carrying out experiments. Each experiment yields measurement data  $x_{\text{obs}}$ . We have a model  $M(\theta, z)$  that gives predictions  $x = M(\theta, z)$  for this data for any given value of a model parameter  $\theta$  and a latent parameter  $z$ . Here  $\theta$  is a fundamental parameter that quantifies the process itself and thus its unique value is of interest, whereas  $z$  denotes an unmeasured parameter that can vary from experiment to experiment and determines the outcome  $x$  in accordance with model  $M$ . We assume that there exist a value of  $\theta$  for which the model describes (to some extent) observations given an appropriate value of  $z$  for each experiment. Our task is to infer the probability distribution for the value of  $\theta$  from a series of repeated experimental measurements. Put differently, the objective is to infer the most probable range for  $\theta$  given the observed data  $x_{\text{obs}}$ . Bayesian statistics provides a framework for the outlined problem. The probability distribution to be determined is referred to as a posterior distribution  $p(\theta|x_{\text{obs}})$ , which explicitly indicates the data  $x_{\text{obs}}$  used for making the inference. Let us start from the case of no latent parameter. The posterior can then be calculated using Bayes' theorem

$$p(\theta|x_{\text{obs}}) = \frac{p(x_{\text{obs}}|\theta) \cdot p(\theta)}{p(x_{\text{obs}})} \quad (2)$$

where  $p(\theta)$  quantifies the prior knowledge about possible values of  $\theta$ , the likelihood  $p(x_{\text{obs}}|\theta)$  conveys how likely a measurement yielding  $x_{\text{obs}}$  is for a given  $\theta$  and  $p(x_{\text{obs}}) = \int p(x_{\text{obs}}|\theta)p(\theta)d\theta$  appears as a normalizing factor. To incorporate the dependence on the latent parameter we integrate over all its possible values, denoting  $p(x_{\text{obs}}|\theta, z)$  as the corresponding joint likelihood

$$p(\theta|x_{\text{obs}}) = \frac{\int p(x_{\text{obs}}|\theta, z)p(z)dz \cdot p(\theta)}{\iint p(x_{\text{obs}}|\theta, z)p(z)p(\theta)dzd\theta}, \quad (3)$$

where  $p(z)$  specifies prior knowledge related to values of the latent parameter  $z$ . Now we can sequentially account

for all observations, each time using the obtained posterior as the prior for processing the next observation. Note that we do not update the prior for  $z$  because its value is assumed to be different in all the experiments.

A closed form of the posterior rarely exist and numerical approaches are often used. A common strategy is to approximate the posterior by collecting a finite number of samples from it. Methods such as importance sampling, Markov chain Monte Carlo (MCMC) and sequential Monte Carlo (SMC) [18–20] are prevalent choices. However, all of the above will require direct evaluation of the likelihood which can be computationally prohibitive for highly dimensional datasets [21]. If the model  $M$  is implicitly defined through a computer simulation, its concomitant likelihood can be intractable [13]. A remedy is offered by the rapidly developing field of simulation-based inference [22] in which the direct calculation of the likelihood is averted. To motivate its use we adopt and develop the discussion made in Ref. [21].

Consider the standard rejection sampling algorithm with the goal of sampling a target density  $T(\theta)$  provided some auxiliary sampling density  $A(\theta)$  with the requirement  $A(\theta) > 0$  if  $T(\theta) > 0$ . Then, the algorithm reads

---

### Algorithm 1 Standard rejection sampling algorithm

---

- 1: Sample a proposal  $\theta^* \sim A(\theta)$ .
  - 2: Admit the proposal with a probability of  $\frac{T(\theta^*)}{CA(\theta^*)}$  where  $C \geq \text{argmax}_{\theta} [\frac{T(\theta)}{A(\theta)}]$ .
  - 3: If  $\theta^*$  was not admitted, discard the proposal and repeat steps (1)-(2) as many times necessary.
- 

After  $N$  trials a collection of samples from  $T(\theta)$  is obtained. The connection to Bayesian statistics is made by selecting  $T(\theta) = p(\theta|x_{\text{obs}})$  and  $A(\theta) = p(\theta)$ . Then, Eq. (2) implies that the acceptance rate in Alg. 1 becomes proportional to the likelihood  $\frac{p(\theta^*|x_{\text{obs}})}{p(\theta^*)} \propto p(x_{\text{obs}}|\theta^*)$  which is incalculable by our premise. Still, it is possible to determine whether to accept proposals or not without explicit computation of the likelihood. To show this we first note that the model  $M(\theta, z)$  is capable of generating samples of observations  $x \sim p(x_{\text{obs}}|\theta, z)$  provided values of  $\theta$  and  $z$ . Now, the probability to produce  $x = x_{\text{obs}}$  coincides with  $p(x_{\text{obs}}|\theta, z)$  which calls for modifications to Alg. 1 so that it reads

---

### Algorithm 2 : Likelihood-free rejection sampling

---

- 1: Sample proposals  $\theta^* \sim p(\theta)$ ,  $z^* \sim p(z)$ .
  - 2: Generate data  $x^* = M(\theta^*, z^*)$  from the model.
  - 3: If  $x^* = x_{\text{obs}}$  the proposal is admitted, if not it is discarded.
  - 4: Repeat (1)-(3) as many time necessary.
- 

While avoiding direct computation of the Likelihood, step 3 of Alg. 2 introduces a notable impediment. To



illustrate it, consider the binning of data from an experiment into  $\dim(x_{\text{obs}}) = B$  bins so that

$$x_{\text{obs}} = [c_1, c_2, c_3, \dots, c_B], \quad (4)$$

$$x = [c'_1, c'_2, c'_3, \dots, c'_B] \quad (5)$$

where  $c_b, c'_b \in \mathbb{Z}$  denote integer counts belonging to the  $b$ :th bin. Then, denote  $p_b$  as the probability to coincide  $c_b = c'_b$  at bin  $b$ , assuming that this is independent between bins. Then, the probability to accept a proposal  $\theta^*$  becomes

$$p(x = x_{\text{obs}}) = \prod_{b=1}^{b=B} p_b \quad (6)$$

which approaches zero in the limit of highly dimensional datasets  $B \rightarrow \infty$ . The acceptance rate in Eq. (6) is lower or even infeasible for continuous data in which  $c_b, c'_b \in \mathbb{R}$  are real numbers. Hence, the appeal for a precise match has to be relieved in making the sampling efficiency practical. Realizing that this rate becomes significantly higher by admitting samples if  $x \approx x_{\text{obs}}$  prompts us to define a rule when data are *sufficiently close*

$$\|x - x_{\text{obs}}\| \leq \epsilon \quad (7)$$

where  $\|\cdot\|$  is a suitable distance metric and  $\epsilon$  is a threshold. Accepted samples in accordance with Eq. (7) are inevitably drawn from an approximate posterior  $\hat{p}(\theta|x_{\text{obs}})$  and its accuracy is solely dictated by  $\epsilon$  which also affects the sampling efficiency. However, consider the aforementioned example with an Euclidean distance metric so that Eq. (7) reads

$$\left( \sum_{b=1}^{b=B} (c_b - c'_b)^2 \right)^{1/2} \leq \epsilon \quad (8)$$

and examine the favorable case in which  $c_b - c'_b \sim \Delta \ll 1$  varies negligibly between bins. We can then naively state Eq. (8) as

$$\dim(x_{\text{obs}}) \leq (\epsilon/\Delta)^2. \quad (9)$$

Evidently, Eq. (9) states that the dimension of  $x_{\text{obs}}$  is bounded from above by the threshold  $\epsilon$  and the error  $\Delta$ . However, for the quality of inference  $\epsilon \rightarrow 0$  is desired, which puts a stringent limit on the dimensionality of  $x_{\text{obs}}$ . To mitigate this, one can introduce so-called *summary statistics*

$$S : \mathbb{R}^B \mapsto \mathbb{R}^\beta \quad (10)$$

being a function that transforms data of potentially noisy nature into a vector of indicative characteristics

ought to unambiguously characterize the data with respect to all possible  $\theta$ . Clearly, the dimensionality  $\beta$  of the space of such vectors can be much less than the number of cells  $B$ . Moreover, the function of summary statistics can even be defined in an agnostic way with respect to the binning choice. As an example, one could construct a vector containing the sample mean  $\mu$  and variance  $\sigma^2$  of  $x_{\text{obs}}$ :  $S(x_{\text{obs}}) = (\mu, \sigma^2)$ .

By converting  $x_{\text{obs}} \rightarrow S(x_{\text{obs}})$ , the third step of Alg. 2 can be reformulated to accept samples if

$$\|S(x) - S(x_{\text{obs}})\| \leq \epsilon. \quad (11)$$

Although we now have methodologically accurate and in some cases practically feasible routine for sampling the posterior there are two more standard improvements. First, Eq. (11) implies an acceptance probability of either zero or one and thus doesn't account for how close the match is. To enhance the contribution of the cases yielding more accurate agreement relative to the ones giving a marginal agreement, one can use a so-called *kernel function*

$$K_\epsilon : \mathbb{R}^\beta \mapsto \mathbb{R} = K_\epsilon \left( \frac{\|S(x) - S(x_{\text{obs}})\|}{\epsilon} \right), \quad (12)$$

which defines a probability transition from one in case of a perfect match ( $K_\epsilon(0) = 1$ ) to zero in cases of deviation by the summary-statistics distance of order  $\epsilon$  and greater.

The second improvement concerns the fact that Alg. 1 implies either accepting or rejecting cases, which means that many accepted cases are needed to mitigate the noise related to this additional probabilistic element in the algorithm. Effectively this means that we marginally benefit from cases of low acceptance probability. To avoid this, one can instead interpret the acceptance probability as the weight of samples, thereby accounting for all the proposals that yield non-zero acceptance probability.

We can now return back to the inclusion of the latent variable  $z$ . In this case, we can generate several proposals  $z^* \sim p(z)$  based on our prior knowledge of it and again accept the cases of good enough matches based on the outlined procedure. Effectively, we try to guess  $z$  using as many attempts as needed. Finally, we note that we can sequentially update our posterior using each  $x_{\text{obs}}$  in a sequence of measurements. To do so, we can compute the posterior for each new measurement using the previous posterior as the prior. The algorithm for processing the  $i$ -th observation ( $i = 1$  denote the first measurement in the sequence)  $x_{\text{obs}}^i$  for computing the posterior  $p(\theta | x_{\text{obs}}^i, x_{\text{obs}}^{i-1}, \dots, x_{\text{obs}}^1)$  from the previous  $p(\theta | x_{\text{obs}}^{i-1}, \dots, x_{\text{obs}}^1)$  then takes the form

---

**Algorithm 3** : ABC sampling with latent variable
 

---

- 1: Sample proposals  $\theta^* \sim p(\theta \mid x_{\text{obs}}^{i-1}, \dots, x_{\text{obs}}^1), z^* \sim p(z)$ .
- 2: Perform a simulation and retrieve  $x^* = M(\theta^*, z^*)$  and compute the weight:

$$w^* = \frac{K_\epsilon (\|S(x_{\text{obs}}^i) - S(x^*)\|/\epsilon)}{p(\theta^* \mid x_{\text{obs}}^{i-1}, \dots, x_{\text{obs}}^1) p(z^*)} \quad (13)$$

- 3: If  $w^* > 0$ , accept the proposal with the computed weight.
  - 4: Repeat steps (1) – (3) as many times as needed to approximate the posterior  $p(\theta \mid x_{\text{obs}}^i, \dots, x_{\text{obs}}^1)$ .
- 

In practice, one central difficulty of the ABC routine is choosing valid summary statistics, i.e. summary statistics that differentiate all the cases in terms of  $\theta$  and  $z$ . This means that summary statistics doesn't yield close states for any two different pairs of  $\theta$  and  $z$ . Clearly, if this is not the case the procedure admits the acceptance of cases of wrong  $\theta^*$  when  $z^*$  provides a compensation to make  $S(x^*(\theta^*, z^*))$  close to  $S(x_{\text{obs}}(\theta^{\text{true}}, z^{\text{true}}))$ . This can totally preclude the convergence of the ABC sampling procedure. Finding robust summary statistics is known to be a problem-dependent task that requires analysis of possible cases. In the next section we consider a proof-of-principle problem that includes a dependency on the latent variable. In doing so, we determine valid summary statistics and elaborate possible experimental strategies relevant to the tests of SFQED based on the collision of electron beams with focused laser pulses.

### III. PROBLEM STATEMENT

As a proof-of-principle case, we consider the problem of detecting and measuring the extent of effective mass shift for the electron due to its coupling with the strong-field environment [9, 15–17]. The task is to infer the value of the parameter that quantifies this effect from the measured angular-energy spectra of photons emitted during the collision of high-energy electron beams with focused laser pulses. We make several assumptions to simplify the problem while keeping some indicative difficulties that show the capabilities of the methodology in question. In particular, we assume that the spatio-temporal mismatches between the electron beam and focused laser field are not measurable and vary from collision to collision. This leads to fluctuations of the electromagnetic field amplitude observed by the electrons. This in turn makes it impossible to relate the change of electron dynamics in a particular experiment (collision) to any certain amplitude, which has to be determined in the case of a straightforward measurement of the effective mass shift. To show how the ABC methodology resolves this difficulty we model the aforementioned variations by assuming that the electron beam propagates through a 1D laser pulse with an unknown amplitude that varies from collision to collision. In terms of introduced terminology, we introduce a latent

parameter being a factor  $< 1$  that reduces the laser field amplitude everywhere in each experiment, but varies uncontrollably from experiment to experiment. In what follows, we detail this *model* of hypothetical experiments.

The presence of a strong background electromagnetic field is conjectured to drive the expansion parameter of QED to  $\alpha_f \chi^{2/3}$  where  $\alpha_f \approx 1/137$  is the fine-structure constant [9, 15–17]. For values  $\alpha_f \chi^{2/3} \gtrsim 1$  the theory is rendered nonperturbative. In this domain, photons, electrons and positrons can be thought to acquire an effective mass as a result of radiative corrections. Specifically, one can show that the effective mass of the electron  $\tilde{m}_e$  can be estimated to be [15]

$$\tilde{m}_e^2 = m_e^2 + \delta m_e^2 = m_e^2 (1 + 0.84 \alpha_f \chi^{2/3}) \quad (14)$$

which implies an effective value of  $\chi$  (mass enters Eq. (1) through  $E_{\text{crit}}$ )

$$\tilde{\chi}^{2/3} = \frac{\chi^{2/3}}{1 + 0.84 \alpha_f \chi^{2/3}}. \quad (15)$$

To benchmark this effect and measure its extent one can consider the value of 0.84 as a model parameter  $\theta$  to be determined based on experiments:

$$\tilde{\chi}^{2/3} = \frac{\chi^{2/3}}{1 + \theta \alpha_f \chi^{2/3}}. \quad (16)$$

Replacement of effective quantities  $\tilde{m}_e, \tilde{\chi}$  affects the rate of photon emission and pair formation. As for the former, we can write the rate as [23, 24]:

$$\frac{\partial I}{\partial \omega}(\delta, \theta) = \frac{\sqrt{3} \tilde{m}_e q_e^2 c \tilde{\chi} (1 - \delta)}{2\pi \gamma_e \hbar} \left( F_1(\zeta) + \frac{3}{2} \delta \tilde{\chi} \zeta F_2(\zeta) \right) \quad (17)$$

where  $\zeta = \frac{2}{3\tilde{\chi}} \frac{\delta}{1-\delta}$ ,  $\delta = \frac{\hbar \omega}{\tilde{m}_e c^2 \gamma_e}$  is the photon energy with frequency  $\omega$  normalized to the emitting electron energy and  $F_1(x), F_2(x)$  denote the first and second Synchrotron functions defined by

$$F_1(y) = y \int_y^\infty K_{5/3}(y) dy, \quad F_2(y) = y K_{2/3}(y) \quad (18)$$

with  $K_\nu(y)$  being the modified Bessel function of the second kind.

Hence, one measurable property  $x_{\text{obs}}$  might be the post-collision spectrum of photons. Indeed, the effect attributed to  $\theta$  may be slight and the probabilistic nature of emissions become increasingly difficult to measure by the onset of electromagnetic cascades and low-energy emissions when  $\chi \gg 1$ . For our proof-of-principle, we disregard pair formation and center in on the process of nonlinear Compton scattering to elude this difficulty. Additionally, we neglect the energy loss of electrons in their

propagation direction under the assumption  $a_0/\gamma_e \ll 1$  where  $a_0 = \frac{q_e E_0}{m_e \omega_L \xi}$  is the peak dimensionless amplitude of the laser having frequency  $\omega_L$  and peak electric field  $E_0$ . To define the simulator, we select an elementary geometry resembling the interaction between a focused laser pulse and a counter-propagating electron bunch, both susceptible to misalignment. We accomplish this by simulating a single electron of momentum  $p_z = -m_e c \gamma$  to impinge a plane wave laser pulse with electric field

$$E_x(z, t) = (1 - d)E_0 \sin(k\xi) \cos^2\left(\frac{\pi\xi}{L}\right) \Pi\left(\frac{\xi}{L}\right) \quad (19)$$

where  $\xi = z - ct$  is the moving coordinate,  $k$  and  $L$  are the wavenumber and pulse length of the laser respectively and  $\Pi(x)$  is defined as a function equating to unity when  $|x| < 1/2$  and zero otherwise. Here we introduce the latent parameter  $0 \leq d \leq 1$  to express the misalignment in the experimental scheme, reducing the laser amplitude experienced by the electrons.

However, the unruliness of  $d$  can obstruct ABC sampling. This becomes evident by comparing the spectra produced by Eq. (17) with  $\theta = 0, d \neq 0$  and  $\theta \neq 0, d = 0$ . Writing the order of estimate for Eq. (16) as

$$\tilde{\chi}(\theta, d) \sim (1 - d)\chi_0 \left(1 + \theta\alpha_f ((1 - d)\chi_0)^{2/3}\right)^{-3/2} \quad (20)$$

where  $\chi_0 = \gamma_e (E_0/E_{\text{crit}})$  is the peak value of  $\chi$ . The two cases can yield comparable values  $\tilde{\chi}(\theta \neq 0, d = 0) \sim \tilde{\chi}(\theta = 0, d \neq 0)$  if

$$d \sim 1 - \left(1 + \theta\alpha_f \chi_0^{2/3}\right)^{-3/2}. \quad (21)$$

As a result, the value of  $\tilde{\chi}$  can be similar for several combinations of  $\theta$  and  $d$ , generating similar energy spectra. Hence, any summary statistic obtained from such data can be near-identical, obscuring the effect of  $d$  to that of  $\theta$  or vice versa. Conclusively, the energy spectrum is not indicative enough to infer the value of  $\theta$ . This can be remedied by including information into  $x_{\text{obs}}$  such that the effects of  $\theta$  and  $d$  become disentangled. If a complementary property of the emission is found such that the induced deviation of either parameter becomes uncorrelated, it is possible to disentangle their effects on  $x_{\text{obs}}$ .

We now seek such a property to be included into  $x_{\text{obs}}$  and the choice of summary statistics to eliminate the latent variable  $d$ . To commence the discussion we remark that electrons conserve their transverse momentum within the laser field [25]

$$\vec{p}_\perp = q_e \int \vec{E}_\perp dt \quad (22)$$

in which  $\vec{p}_\perp$  and  $\vec{E}_\perp$  denote the transverse components of the electron momentum and electric field respectively. Therefore, at each instance of time, the electron propagates towards the direction that deviates from the initial direction by an angle  $\alpha$ :

$$\alpha = \arctan\left(\frac{|\vec{p}_\perp|}{|\vec{p}_z|}\right), \quad (23)$$

where we assume that the motion remains highly relativistic. Evidently, emitted photons retain this angle and if the pulse is circularly polarized, this becomes correlated to the value of  $\chi$  [26]. Note that in the case of highly relativistic motion with  $\alpha \ll 1$ , the change of effective mass doesn't affect the deviation angle because it cannot change  $\vec{p}_z$  due to momentum conservation (the gamma factor changes instead), while  $\vec{p}_\perp$  is totally defined by the vector potential according to Eq. (22).

Accounting for the angular distribution of the emission leads us to redefine  $x_{\text{obs}}$  as a fractional energy distribution per unit frequency  $\Delta\omega$  and unit angle  $\Delta\alpha$ :  $x_{\text{obs}}(\delta, \delta + \Delta\delta, \alpha, \alpha + \Delta\alpha)$  as a function of  $\delta$  and  $\alpha$ .

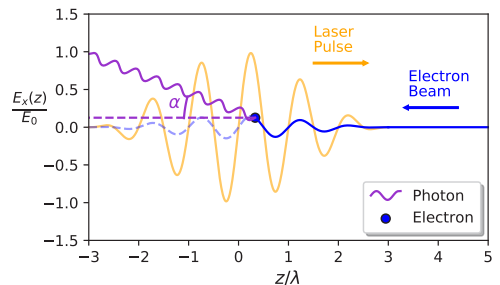


FIG. 1. Representation of the numerical implementation of the experiment (deviation angle is exaggerated).

We are now in a position to determine the summary statistics  $S(x_{\text{obs}})$  necessary to eliminate  $d$ . Presumably, there exist several configurations that provide this as there is no prescribed way of formulating  $S$ . To identify some robust and simple enough option we evaluate moments of the two-dimensional data  $x_{\text{obs}}$  to order  $i$  and  $j$ :

$$M_{ij} = \iint x_{\text{obs}}(\delta, \delta + \Delta\delta, \alpha, \alpha + \Delta\alpha) \delta^i \alpha^j d\delta d\alpha. \quad (24)$$

Now, let us try to select a set of moments such that any combination  $(\theta, d)$  maps to a presumably unique value of this set. Fig. 2 illustrates contours of four distinct moments  $M_{ij}$  in the space of  $\theta$  and  $d$ . The set of moments

in Fig. 2 (a) is a practical choice as the contours are not parallel anywhere, suggesting a unique pair for every  $\theta$  and  $d$ . In contrast, Fig. 2 (b) depicts a scenario when the contours become parallel at several points in the parameter space, meaning that the values of the plotted moments do not unambiguously indicate a single pair of  $\theta$  and  $d$ . We conclude that selecting  $S(x_{\text{obs}}) = (M_{00}, M_{12})$  is a valid choice for ABC sampling.

#### IV. ANALYSIS

In our simulations, the plane wave pulse is designated by a wavelength of  $\lambda = 0.8 \mu\text{m}$ , pulse length  $L = 6\lambda$  and peak amplitude  $a_0 = 100$  (excluding the factor of  $(1-d)$ ). Electrons are assigned an initial energy of 170 GeV ( $\gamma_e \sim 10^5$ ) situated a distance  $z_s = 5\lambda$  from the origin (the numerical layout can be seen in Fig. 1). Both electron and pulse are allowed to counter propagate for  $N$  time steps  $\Delta t = \frac{(L+z_s/2)c^{-1}}{N}$ . Here,  $x(\delta, \delta + \Delta\delta, \alpha, \alpha + \Delta\alpha)$  is discretized by a  $100 \times 100$  grid of cells  $x(m\Delta\delta, n\Delta\alpha)$  each with size  $\Delta\delta \times \Delta\alpha$  and  $m, n = 0, 1, 2, \dots, 99$ . At each time step  $q$ , Eqs. (22) and (23) are used to estimate  $n \approx \alpha/\Delta\alpha$ . Then, for each  $m$  we accumulate

$$x_{q\Delta t} = x_{(q-1)\Delta t} + \Delta\alpha\Delta\omega\Delta t \frac{\partial I}{\partial \omega}(m\Delta\delta, \theta) \quad (25)$$

where we have suppressed the arguments of  $x$  for readability and subscripts denote the time step. For our proof-of-principle we perform blind tests of  $x = M(\theta, d)$  against an "experiment"  $x_{\text{obs}} = M(\theta^{\text{true}} = 0.84, d)$  which serves as a ground truth. Here, the  $\theta$  value is fixed to  $\theta^{\text{true}}$  but the latent variable  $d$  varies randomly between experiments.

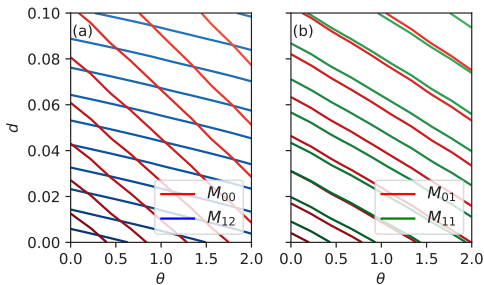


FIG. 2. Contours of  $M_{ij}$  as a function of  $\theta$  and  $d$  where (a) compares  $M_{00}$  and  $M_{12}$ , (b) compares  $M_{01}$  and  $M_{11}$ .

Turning to the prerequisites for ABC sampling, we adopt the following priors over  $\theta$  and  $d$

$$p(\theta) = \mathcal{U}(0, 150), \quad p(d) = \mathcal{U}(0, 0.1) \quad (26)$$

where  $\mathcal{U}(a, b)$  denote the uniform distribution with lower and upper bounds  $a$  and  $b$  respectively. Though there is no prior knowledge apart from  $\theta \geq 0$  and  $0 \leq d \leq 1$  we argue that the given simulation parameters yield  $\chi_0 \approx 100$  and so setting  $\theta = 150$  would then drive the value of  $\tilde{\chi}$  below one, approaching a classical description. As for  $d$ , one could construct a prior from empirical values obtained in a real experiment. Lacking this option, we assume that the amplitude can vary at most by 10%.

During sampling, the following distance is calculated to discriminate between observations

$$\|S(x) - S(x_{\text{obs}})\| = \sqrt{d_{00}^2 + d_{12}^2} \quad (27)$$

where  $d_{ij} = |1 - \frac{M_{ij}^{\text{sim}}}{M_{ij}}|$  (not to be confused with the latent parameter) in which the superscript label moments evaluated from simulations  $x = M(\theta, d)$ . A uniform kernel  $K_\epsilon(\cdot) = \Pi(\cdot)$  is chosen with threshold  $\epsilon = 0.1$  derived from the requirement to accept  $N_\theta = 1600$  samples over the course of  $\approx 50$  sampling hours. For every 50:th proposal  $\theta^*$  we generate new observed data  $x_{\text{obs}}$  as to not bias the result toward the existing value of  $d^* \sim p(d)$ .

In Fig. 3 we present the result of sampling the posterior based on the described ABC routine applied to the simulated outcome of a single collision experiment with unknown value of  $d$ . The fact that the accepted samples are distributed around the actually selected value of  $\theta^{\text{true}} = 0.84$  indicates the claimed capability of the method. To achieve narrower distribution and reduce the credible interval of the distribution, one can process a number of experiments through Alg. 3. That is, the next experiment adapts a prior based on the inference from the previous one.

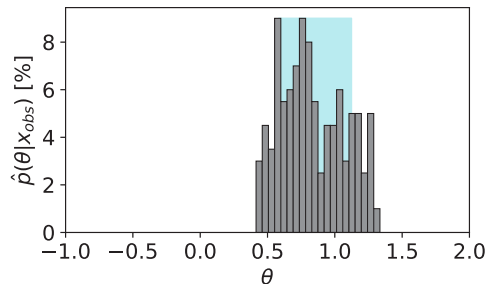


FIG. 3. Approximate posterior obtained with 1600 accepted samples using ABC sampling where the shaded region indicate the 68 % credible interval.

## V. CONCLUSIONS

We have considered prospects for an experiment capable of inferring a parameter  $\theta$  that signify deviations from nonlinear Compton scattering via the notion of effective mass in the regime  $\chi \gg 1$ . The results propel the strategies necessary to incorporate ABC sampling in analogous experiments, scalable to the inclusion of several parameters  $\theta$  and  $z$  accounting for alternative nonperturbative effects. An improved implementation of the interaction will be needed for designing future experiments. This can be done by e.g. simulating a realistically focused laser pulse, devising more comprehensive description via latent parameters and accounting for electromagnetic cascades. Carrying it out might pose an increased computational load as well as affect the sampling efficiency

of ABC. Nonetheless, its convergence can be accelerated by further investigating additional summary statistics, non-uniform kernels and the use of machine learning to suggest better proposals. Additionally, the use of high-performance computing to recruit many ABC samplers in parallel can alleviate both impairments.

## ACKNOWLEDGMENTS

The authors acknowledge support from the Swedish Research Council (Grants No. 2017-05148 and No. 2019-02376). The computations were enabled by resources provided by the National Academic Infrastructure for Supercomputing in Sweden (NAISS) at Tetralith partially funded by the Swedish Research Council through grant agreement no. 2022-06725. The authors would like to thank Tom Blackburn for useful discussions.

- 
- [1] K. Poder, M. Tamburini, G. Sarri, A. Di Piazza, S. Kuschel, C. D. Baird, K. Behm, S. Bohlen, J. M. Cole, D. J. Corvan, M. Duff, E. Gerstmayr, C. H. Keitel, K. Krushelnick, S. P. D. Mangles, P. McKenna, C. D. Murphy, Z. Najmudin, C. P. Ridgers, G. M. Samarin, D. R. Symes, A. G. R. Thomas, J. Warwick, and M. Zepf, Experimental signatures of the quantum nature of radiation reaction in the field of an ultraintense laser, *Phys. Rev. X* **8**, 031004 (2018).
- [2] J. Cole, K. Behm, E. Gerstmayr, T. Blackburn, J. Wood, C. Baird, M. J. Duff, C. Harvey, A. Ilderton, A. Joglekar, *et al.*, Experimental evidence of radiation reaction in the collision of a high-intensity laser pulse with a laser-wakefield accelerated electron beam, *Physical Review X* **8**, 011020 (2018).
- [3] H. Abramowicz, U. Acosta, M. Altarelli, R. Assmann, Z. Bai, T. Behnke, V. Benhamou, T. Blackburn, S. Boogert, O. Borysov, *et al.*, Conceptual design report for the luxe experiment, *The European Physical Journal Special Topics* **230**, 2445 (2021).
- [4] V. Yakimenko, L. Alsberg, E. Bong, G. Bouchard, C. Clarke, C. Emma, S. Green, C. Hast, M. Hogan, J. Seabury, *et al.*, Facet-ii facility for advanced accelerator experimental tests, *Physical Review Accelerators and Beams* **22**, 101301 (2019).
- [5] C. Bula, K. McDonald, E. Prebys, C. Bamber, S. Boege, T. Kotseroglou, A. Melissinos, D. Meyerhofer, W. Ragg, D. Burke, *et al.*, Observation of nonlinear effects in Compton scattering, *Physical Review Letters* **76**, 3116 (1996).
- [6] M. Inuma, K. Matsukado, I. Endo, M. Hashida, K. Hayashi, A. Kohara, F. Matsumoto, Y. Nakanishi, S. Sakabe, S. Shimizu, *et al.*, Observation of second harmonics in laser-electron scattering using low energy electron beam, *Physics Letters A* **346**, 255 (2005).
- [7] T. Kumita, Y. Kamiya, M. Babzien, I. Ben-Zvi, K. Kusche, I. Pavlishin, I. Pogorelsky, D. Siddons, V. Yakimenko, T. Hirose, *et al.*, Observation of the nonlinear effect in relativistic Thomson scattering of electron and laser beams, *Laser physics* **16**, 267 (2006).
- [8] T. Englert and E. Rinehart, Second-harmonic photons from the interaction of free electrons with intense laser radiation, *Physical Review A* **28**, 1539 (1983).
- [9] A. Fedotov, A. Ilderton, F. Karbstein, B. King, D. Seipt, H. Taya, and G. Torggrimsson, Advances in qed with intense background fields, arXiv preprint arXiv:2203.00019 (2022).
- [10] T. Ritto, S. Beregi, and D. Barton, Reinforcement learning and approximate bayesian computation for model selection and parameter calibration applied to a nonlinear dynamical system, *Mechanical Systems and Signal Processing* **181**, 109485 (2022).
- [11] M. C. Kennedy and A. O'Hagan, Bayesian calibration of computer models, *Journal of the Royal Statistical Society: Series B (Statistical Methodology)* **63**, 425 (2001).
- [12] D. N. DeJong, B. F. Ingram, and C. H. Whiteman, A bayesian approach to calibration, *Journal of Business & Economic Statistics* **14**, 1 (1996).
- [13] J. Brehmer, G. Louppe, J. Pavez, and K. Cranmer, Mining gold from implicit models to improve likelihood-free inference, *Proceedings of the National Academy of Sciences* **117**, 5242 (2020).
- [14] J. Akeret, A. Refregier, A. Amara, S. Seehars, and C. Hasner, Approximate bayesian computation for forward modeling in cosmology, *Journal of Cosmology and Astroparticle Physics* **2015** (08), 043.
- [15] V. Yakimenko, S. Meuren, F. Del Gaudio, C. Baumann, A. Fedotov, F. Fluzza, T. Grismayer, M. Hogan, A. Pukhov, L. Silva, *et al.*, Prospect of studying nonperturbative qed with beam-beam collisions, *Physical review letters* **122**, 190404 (2019).
- [16] V. Ritus, Radiative effects and their enhancement in an intense electromagnetic field, *Sov. Phys. JETP* **30**, 052805 (1970).
- [17] S. Meuren and A. Di Piazza, Quantum electron self-interaction in a strong laser field, *Physical review letters* **107**, 260401 (2011).
- [18] S. T. Tokdar and R. E. Kass, Importance sampling: a review, *Wiley Interdisciplinary Reviews: Computational*

- Statistics **2**, 54 (2010).
- [19] A. Doucet, N. d. Freitas, and N. Gordon, An introduction to sequential monte carlo methods, in *Sequential Monte Carlo methods in practice* (Springer, 2001) pp. 3–14.
- [20] S. Brooks, A. Gelman, G. Jones, and X.-L. Meng, *Handbook of markov chain monte carlo* (CRC press, 2011).
- [21] S. A. Sisson, Y. Fan, and M. Beaumont, *Handbook of approximate Bayesian computation* (CRC Press, 2018).
- [22] K. Cranmer, J. Brehmer, and G. Louppe, The frontier of simulation-based inference, *Proceedings of the National Academy of Sciences* **117**, 30055 (2020).
- [23] V. B. Berestetskii, E. M. Lifshitz, and L. P. Pitaevskii, *Quantum Electrodynamics: Volume 4*, Vol. 4 (Butterworth-Heinemann, 1982).
- [24] V. Baier and V. Katkov, Quantum effects in magnetic bremsstrahlung, *Physics Letters A* **25**, 492 (1967).
- [25] A. Macchi, *A superintense laser-plasma interaction theory primer* (Springer Science & Business Media, 2013).
- [26] C. Olofsson and A. Gonoskov, Attaining a strong-field qed signal at laser-electron colliders with optimized focusing, *Physical Review A* **106**, 063512 (2022).